LBL-16089
c.2

Lawrence Berkeley Laboratory
UNIVERSITY OF CALIFORNIA

RECEIVED
LAWRENCE
BERKELEY LABORATORY
JUL 5 1983
LIBRARY AND
DOCUMENTS SECTION

Materials & Molecular Research Division

HIGH TEMPERATURE CORROSION OF IRON AND IRON-BASED ALLOYS IN SULFUR CONTAINING ATMOSPHERES

F.C. Yang
(Ph.D. Thesis)

April 1983

TWO-WEEK LOAN COPY
This is a Library Circulating Copy which may be borrowed for two weeks. For a personal retention copy, call Tech. Info. Division, Ext. 6782.

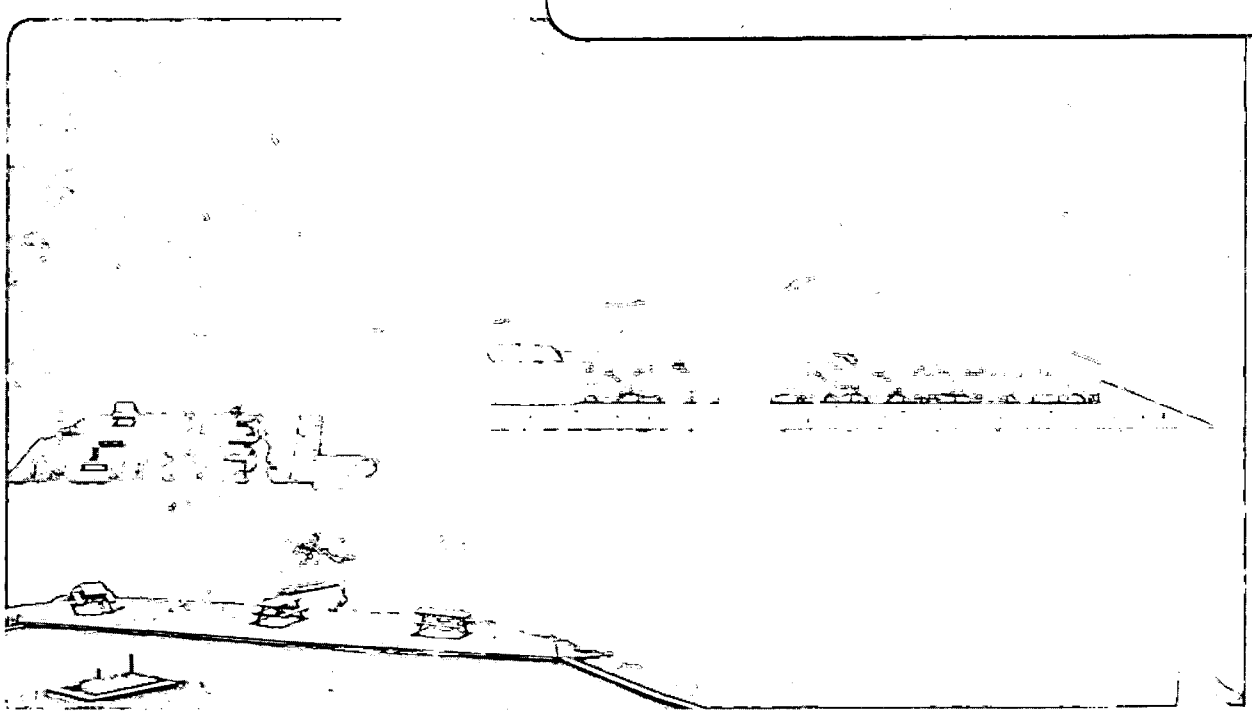

Prepared for the U.S. Department of Energy under Contract DE-AC03-76SF00098

LBL-16089
c.2

DISCLAIMER

This document was prepared as an account of work sponsored by the United States Government. While this document is believed to contain correct information, neither the United States Government nor any agency thereof, nor the Regents of the University of California, nor any of their employees, makes any warranty, express or implied, or assumes any legal responsibility for the accuracy, completeness, or usefulness of any information, apparatus, product, or process disclosed, or represents that its use would not infringe privately owned rights. Reference herein to any specific commercial product, process, or service by its trade name, trademark, manufacturer, or otherwise, does not necessarily constitute or imply its endorsement, recommendation, or favoring by the United States Government or any agency thereof, or the Regents of the University of California. The views and opinions of authors expressed herein do not necessarily state or reflect those of the United States Government or any agency thereof or the Regents of the University of California.

LBL-16089

HIGH TEMPERATURE CORROSION OF IRON AND IRON-BASED ALLOYS IN SULFUR CONTAINING ATMOSPHERES

Frank Chin-tai Yang
Ph.D. Thesis

Materials and Molecular Research Division
Lawrence Berkeley Laboratory

and

Department of Materials Science and Mineral Engineering
University of California, Berkeley, CA 94720

April 1983

This work was supported by the Director, Office of Energy Research, Office of Basic Energy Science, Materials Sciences Division of the U.S. Department of Energy under Contract Number DE-AC03-76SF00098.

CONTENTS

ABSTRACT

CHAPTER I INTRODUCTION

CHAPTER II TECHNICAL BACKGROUND
- 2.1. Corrosion
- 2.2. Equilibrium Phase Diagram
- 2.3. Microscopic Structure
- 2.4. Transport of Sulfur through Scales
- 2.5. Kinetics
- 2.6. Porous Structure
- 2.7. Influence of Alloy Composition
- 2.8. Scanning Auger Microscopy

CHAPTER III INTRODUCTION TO PRESENT WORK

CHAPTER IV EXPERIMENTAL PROCEDURES

CHAPTER V TRANSPORT OF SULFUR
- 5.1. Sulfur Diffusion in Iron Oxide
- 5.2. Sulfur Diffusion in Pure Chromium

CHAPTER VI HIGH TEMPERATURE CORROSION OF IRON IN CO_2–10%SO_2 ATMOSPHERES
- 6.1. Results
- 6.2. Discussion

CHAPTER VII THE EFFECTS OF ALLOYING ELEMENTS ON HIGH TEMPERATURE CORROSION
- 7.1. Results
- 7.2. Discussion

CHAPTER VIIICONCLUSION

ACKNOWLEDGEMENTS

APPENDICES

REFERENCES

FIGURE CAPTIONS

HIGH TEMPERATURE CORROSION OF IRON AND IRON-BASED ALLOYS

IN SULFUR CONTAINING ATMOSPHERES

Frank Chin-Tai Yang

Ph.D.

Materials Science &
Mineral Engineering

Sponsors: Basic Energy Science Div. of
The U.S. Department of Energy

Materials and Molecular
Research Division of
Lawrence Berkeley Laboratory

Anthony G. Evans
Chairman of Committee

ABSTRACT

The corrosion morphology, kinetics, and mechanism of the attack on metals and some iron-based alloys by sulfur-containing atmospheres are studied at 871°C. In the case of pure iron, protrusions with sulfide-rich cores are observed on the scale surface. This morphology is explained by the fast transport of iron ions through the sulfide-rich streaks. Models of unbalanced diffusion are proposed to account for the formation of an inner porous layer. The addition of alloying elements, such as *Al* and *Cr*, improves the corrosion resistance by forming a protective Al_2O_3 or Cr_2O_3 oxide scale. However, sulfur penetration through the scale and its effect on the spalling resistance of the oxide scale can lead to the onset of a catastrophic corrosion and rapid failure of the alloys. The transport of sulfur through scales, the thermodynamic conditions for the formation of duplex oxide-sulfide scales and the influence of alloying elements are discussed. It is concluded that sulfur penetration through both preformed and growing Al_2O_3 and Cr_2O_3 scales resulting in an accelerated attack is inevitable. Nevertheless, ways of slowing down the attack are recommended.

CHAPTER I
INTRODUCTION

Sulfur is a critical impurity in almost all fossil fuel energy sources and leads to accelerated, and often unacceptable, rates of metal degradation. As the areas of energy conversion and environmental protection become increasingly concerned with the processing and cleanup of sulfur-bearing fossil fuels and their combustion products, the attack of metals by sulfur compounds at high temperatures has become a major corrosion problem.

There is sufficient evidence from a range of laboratory, pilot plant, and production experience to indicate that the current generation of stainless steels and heat resistant alloys will be susceptible to accelerated attack by some combination of environmental variables. Alloys may be corroded by oxidation reactions in which one or more elements in the alloy selectively combine with carbon (*C*), sulfur (*S*), oxygen (*O*), or nitrogen (*N*). This results in a loss of metal by surface deterioration or in a reduction in the mechanical properties (strength, ductility, toughness) by the dissolution of an oxidant (*C, S, O, N*), formation of internal reaction products (carbides, sulfides, oxides, nitrides) or selective removal of one or more elements from the alloy.

Generally speaking, metals, and particularly alloys, resist oxidation in pure oxygen by forming a more or less protective oxide scale. When a second oxidant, such as sulfur, is present, the reaction product may change to include low melting compounds or compounds with higher ionic conductivities and poor adhesion than the oxides normally formed. Both possibilities cause accelerated attack on metals and alloys.

The mechanisms of the simultaneous attack of metals by two oxidants have been discussed by Pettit *et al.*[1], Rahmel[2] and Birks[3]. One of the major features

is that sulfide is always formed in the scale, particularly at the scale/metal interface, even in atmospheres in which calculation shows it to be thermodynamically unstable. Reaction mechanisms which result in enhancement of the sulfur activity have been proposed. For example, it has been postulated that sulfur can penetrate through the growing oxide layers, possibly as a gaseous species, via physical defects. However, the mechanism is still in some doubt.

A second interesting observation is that in many studies of oxidation in sulfur-containing atmospheres the scale has been observed to have a porous inner layer. Birks[4] and Mrowec[5] have proposed a ***dissociation mechanism*** to account for the formation of this porous layer. An alternative explanation suggested by Atkinson *et al.*[6] is that the inner porous layer is formed by the inward transport of oxygen or sulfur; either by bulk, grain boundary, or gaseous diffusion, incorporating any porosity which has formed at the interface. However, the details of this mechanism have not been developed.

The intent of this paper is to present a detailed description of the corrosion mechanism of iron and iron-based alloys in CO_2–10%SO_2 atmospheres at 871°C (1600°F) and to develop an improved understanding of corrosion chemistry in terms of metallurgical and environmental variables that will provide a sound basis for the more effective use of alloys in sulfur-containing atmospheres.

CHAPTER II
TECHNICAL BACKGROUND

2.1. Corrosion

Corrosion is the destruction or deterioration of a material by chemical or electrochemical reaction with the environment. At low temperatures the corrosive environment is commonly liquid, usually aqueous. Often the corrosion mechanism is electrochemical in character. That is to say, the corroding metal has both cathodic and anodic areas which may be permanently separated from each other or may consist of cathodic and anodic sites that shift continually. Ions are transported through the liquid (the electrolyte) and electrons through the substrate between the two regions.

The electrochemical corrosion rate depends on many factors: compositional variations of the material and of the electrolyte, the temperature, the rate of flow of the electrolyte, and any external potential applied to the materials. The low temperature corrosion of most metals and alloys in service falls into the eight catagories of Fontana and Greene[7]: uniform corrosion attack, galvanic corrosion, crevice corrosion, pitting, intergranular corrosion, selective leaching, erosion corrosion, and stress corrosion.

When materials are subjected to high temperature, they may fail through loss of strength or gradually deteriorate through the reaction with either a liquid or gaseous environment. The liquid may be a molten salt, in which case once again an electrochemical process may be operative. As for interaction with a gaseous environment, it is usually an oxidation or a sulfidation reaction, and ideally the corrosion product accumulates at the metal/oxidant interface, thus limiting the further progress of the reaction. Degradation through oxidation or sulfidation limits the use of many materials in oxidizing or sulfidizing

environments. This is especially evident in applications such as jet engines or gas turbines, where both oxygen and sulfur may be present in the combustion products.

The presence of minor impurities in the environment can have a profound effect on high temperature corrosion processes either by inhibiting the development of protective surface layers, or by destroying those already present. Most important impurities are sulfur, chlorine, the alkali metal *Li*, *Na*, and *K*; and the heavy metals *V*, *Pb*, *Mo*. This form of accelerated oxidation of alloys which occurs in combustion gases in the presence of impurities is called *hot corrosion*. Details can be obtained from a review given by Stringer[8].

2.2. Equilibrium Phase Diagram

A convenient way of representing the corrosion product which could be formed in some of these cases is to construct *Ellingham-Pourbaix-type* diagrams as illustrated in Appendix A. These diagrams map out the ranges of stability of the various condensed phases as a function of the thermodynamic activities of two components of the reactive gas, for example, log P_{O_2} and log P_{S_2}. A combined *Ellingham-Pourbaix-type* diagram for the *Fe-S-O*, *Cr-S-O*, *Al-S-O* systems at 871°C is shown in Figure 1[9], in which the heavy lines denote the boundaries of condensed phases at unit activity. The equivalence of P_{S_2} to P_{H_2}/P_{H_2S} and P_{O_2} to P_{SO_2}/P_{SO_3} are also indicated on the coordinate. This *Ellingham Plot* is indispensible in the interpretation of product phase formation and morphology in mixed gases.

A further factor to be considered when exposing alloys to sulfur-bearing environments at high temperature is the possible formation of liquid phases. Among the common low-melting point sulfides and eutectics relevant to high temperature alloys are: NiS_x (MPt 797°C), *FeS* (MPt 1195°C), CoS_x (MPt 1180°C),

Ni_3S_2–Ni (MPt 645°C), Co_3S_4–Co (MPt 880°C), FeS-Fe (MPt 988°C), MnS-Mn (MPt 1240°C), and FeS-FeO (MPt 940°C).

Thermodynamic phase stability diagrams should be regarded primarily as an analytical tool to aid in the understanding of phases likely to be formed in corrosion processes. However, care should be taken in using them to predict the behavior of corroding systems, since these may be significantly displaced from equilibrium. With a multi-component alloy in a gas mixture, several different oxides and/or sulfides may be stable at the same time under a given set of conditions. To predict which of the phases actually will be formed simply on the basis of stability diagrams is inappropriate. The exact reaction products also depend on the kinetics of various competing nucleation, diffusion and growth processes. Nevertheless, with the aid of stability diagrams, the reaction products and the factors in the material and environment that govern corrosion behavior can be identified. The major role of the stability diagrams is to interpret, not to predict. Diagrams such as these are of great value in interpretive metallography and analysis of reaction products.

2.3. Microscopic Structure

The usual sequence of events for the formation of an oxide on an initially clean metal surface may be summarized as the following steps:

(1) The adsorption and possibly subsequent dissociation of gas molecules to form a chemisorbed layer on the surface, usually not more than one monolayer thick.

(2) The development of two-dimensional (2D) oxide nuclei at preferred rates.

(3) Further growth to three-dimensional (3D) oxide nuclei.

(4) The lateral growth and coalescence of these nuclei to form a complete, relatively uniform, oxide film.

(5) The subsequent thickening of this oxide film by the transport of metal or oxygen in an appropriate form through the film, usually by a process of diffusion or ion migration.

When sulfur dioxide is introduced, sulfides and oxides may nucleate and grow on the metal surface competitively. Considering that scales can crack, contain voids, spall, sinter and certain oxides and sulfides can become unstable at elevated temperature by melting or evaporating, it is clear that the general situation is complicated and various morphologies can be observed.

A typical microstructure of the scale formed on pure iron in argon atmospheres containing small amount of SO_2 was described by Flatley *et al.*[10] A very thin wüstite layer is formed at the scale/metal interface. This layer contains small irregular islands of FeS. Above it, there is a region of scale consisting of fine lamellar FeO and FeS duplex structure aligned in columnar blocks. On the outside of the lamellar region, the structure gives way to a massive duplex sulfide-oxide mixture. At the scale/gas interface an Fe_3O_4 layer usually seen free of sulfide is formed.

In regard to alloy oxidation, the factors found to be important to the oxidation of pure metals apply equally to that of alloys. There are also some extra factors to consider, such as the possibility of forming several oxides and sulfides, internal oxidation and sulfidation, the formation of ternary compounds and mixed phases.

Salisbury *et al.*[11] described the morphologies of alloys relying on chromium in SO_2-bearing atmospheres by dividing roughly into three classes containing low, medium and high chromium contents respectively. For the alloys containing low chromium contents, a lamellar duplex scale based on iron

oxides and iron sulfides is formed with the thin chromium-rich stringer free of sulfide running parallel to the metal surface. Between this layer and the metal, there is a porous zone containing mainly chromium sulfides. Chromium is not observed in the scale outside the layer containing stringer which apparently indicates the position of the original metal surface.

With iron-chromium alloys containing 5 ~ 10%Cr exposed to $Ar-2\%SO_2$ at 800°C, an initial layer of magnetite (Fe_3O_4) or mixed iron and chromium spinel ($(Fe, Cr)_3O_4$) layer is formed, and is responsible for the fairly low initial reaction rates. Eventually this scale is penetrated by sulfur, and the formation of sulfides within the scale causing expansion, generating stresses which lead to scale cracking. Sulfides are then formed at the scale/metal interface. The presence of the sulfides originally formed in the oxide scale provide rapid diffusion paths for iron ions and a thick outer layer of basically massive iron oxide and iron sulfide is formed with, next to the metal, a well or a metal consumption zone, filled with chromium sulfides.

Alloys with high chromium contents form a relatively stable chromium-based oxide layer. However, this too is eventually penetrated by sulfur, undergoes sulfide attack at the scale/metal interface and drifts to faster reaction rates.

2.4. Transport of Sulfur through Scales

The formation of sulfides below an oxide scale at the scale/alloy interface is the most common observation when metals or alloys are exposed to sulfur-containing atmospheres at high temperatures. This leads to the obvious conclusion that sulfur can penetrate growing oxide layers.

Seybolt[12], Romeo and Spacil[13], and Wagner[14] measured the transport rate of sulfur through Cr_2O_3 scales and bulk oxides. All agreed that the D values are

in the range $1 \sim 3x10^{-10} cm^2/sec$ at 950°C. With this high diffusion coefficient, a $1 \sim 10\ \mu m$ thick Cr_2O_3 scale can be penetrated within 1 hour, even though the detailed mechanism of diffusion is still not understood. Sulfur penetration through Al_2O_3 scale[14] is about 100 times slower at the same temperature. This means that an alloy which has formed an Al_2O_3 scale can survive 100 times longer than an alloy which has formed a Cr_2O_3 scale following its introduction of sulfur into the atmosphere[15].

Two possibilities for the sulfur transport mechanism through the oxide are postulated: dissolution followed by solid state diffusion of sulfur, which may be lattice diffusion or diffusion along short-circuit paths such as grain boundary or dislocation cores, and transport of gas molecules via physical defects, such as pores and microcracks. These are alternate or parallel mechanisms: both may operate together. The question whether one predominates remains open at present.

For dissolution and ionic transport, the solubility of sulfur within the oxide is clearly important. Present data[3] indicate these solubilities are rather low; $0.1 \sim 0.01\%$ being fairly common. The exact value will of course depend on the P_{S_2} and P_{O_2}: indications are that sulfur solubility increases with sulfur potential (*Sievert's law*). Low sulfur solubilities may not necessarily preclude a lattice transport mechanism since it is the flux, solubility times diffusivity, which is important. Some diffusion data[3] for oxides other than Cr_2O_3 or Al_2O_3 are available, but they are not particularly decisive.

Chang *et al.*[16] have studied the diffusion of S^{35} in single and polycrystalline samples of both NiO and CoO at $1000 \sim 1100$°C in air and found that sulfur can dissolve and diffuse quite rapidly through the oxide. The diffusivities of sulfur in pressed powder polycrystalline samples were about an order of magnitude higher than those in single crystalline samples. The diffusion coefficient could

be reduced by doping with Cr_2O_3, thereby increasing the concentration of nickel vacancies and thus decreasing the concentration of anion vacancies. Chang *et al.*[17] also observed that the diffusivity of sulfur increased as the equilibrium oxygen partial pressure was decreased. Both results indicate that sulfur may migrate through the oxide via anion vacancies.

The transport of gas molecules through scales has been substantiated by Rahmel[18] who explained increased reaction rates in the presence of carbonaceous gases and water vapor by the action of a gaseous redox system in the cracks and pores of a growing scale. Further, Bruce *et al.*[19] demonstrated the continuous creation of microcracks in growing iron oxide scales. However, the lower susceptibility of nickel oxide scales to cracking indicates that gaseous transport may not be easy in this system. Recently, Pope and Birks[20] studied the penetration by sulfur of NiO scales growing on nickel and claimed that the physical mechanism (gas molecule transport) is likely to be predominant.

In view of this evidence for both mechanisms of sulfur transport, it is clear that further investigation is necessary to determine which mechanism predominates in the case of sulfur transport through scales formed on iron and iron-based alloys.

2.5. Kinetics

For many metals, ion diffusion through the oxide layer controls the rate of oxidation. In the Fe-O system, for example, the oxidation process:

$$Fe^{++} + O^{=} \rightarrow FeO$$

occurs near the oxide/air interface, requiring that Fe^{++} diffuses through the oxide scale. If ion diffusion controls oxidation, a parabolic oxidation law is observed, *i.e.*, the oxide thickness x is proportional to $time^{1/2}$.

Although parabolic oxidation is commonly observed for many metals, there are other factors that can change the observed oxidation behavior. For

instance, if the oxide scale is not coherent and cracks or spalls off, the metal is not protected from the oxidizing atmosphere by the scale, and oxidation will occur more rapidly than the parabolic law predicts. Also, the oxide may be volatile (as in the case of CrO_3) so that it vaporizes as it forms. Yet another important feature is the conduction of electrons through the oxide scale. Electron transport must accompany the ion diffusion. Some oxides are poor electrical conductors, and hence ion diffusion may be more rapid than electron transport, making the latter process rate-controlling. Each of the above features can change the oxidation kinetics and give rise to a different oxidation rate law. Below are listed the most common of these oxidation rate laws, with a short explanation of the appropriate rate-controlling mechanism:

Parabolic oxidation ($x^2 = A_1 t$, where A_1 is the temperature-dependent rate constant). This behavior is observed when the oxide scale is coherent and ion diffusion is the rate-limiting process, and the transport properties of the oxide do not vary with thickness or with time.

Linear oxidation ($x = A_2 t$, where A_2 is the temperature-dependent rate constant). Linear oxidation may occur when the transport of ions is faster than the one or other of the interface reactions involved in the oxidation step. In this case the reaction itself will be rate-limiting, leading to a time-independent oxidation rate. Linear oxidation also occurs when the oxide scale is nonprotective: *e.g.*, cracks or porosity in the oxide allow the oxidizing atmosphere to remain in contact with the metal and maintain a constant oxidation rate, or when the repeated fracturing and spalling lead to a constant increase of the thickness of the oxide scale covering the metal surface. Figure 2 illustrates an approximate linear oxidation rate for an oxide that continually fractures or spalls during growth. Each break in the curve represents a fracture in the oxide, with a parabolic growth between fractures. MgO on Mg is an example of a

porous oxide film, while *Nb* and *Ta* form oxide films that continually fracture during growth.

Logarithmic oxidation [$x = A_3 \log(A_4 t + A_5)$, where A_3 is the rate constant]. Oxidation at low temperatures with very thin oxide films often follows logarithmic kinetics and is thought to be controlled by the diffusion of ions driven by large electric fields. The electric potential existing between the cathodic and anodic reaction area is about 1 volt for most oxidation reactions. Thus, for very thin films (< 50Å), voltage gradients of the order of $2x\ 10^8 volts/m$ are established. Electric fields of this magnitude are sufficiently large to drive ion diffusion through the oxide. As the oxide thickens, the effect of the electric field diminishes and growth stops unless the temperature is raised high enough to promote thermally activated diffusion. *Al* and *Cu* both show logarithmic oxidation at low temperatures with limiting oxide thicknesses of about 40Å[21].

In general, a fast parabolic rate is observed when iron is exposed to an atmosphere containing only oxygen as the oxidant. Addition of SO_2 to the atmosphere is found to increase the corrosion rate. But the effect of SO_2 is greatly reduced if free oxygen is also present. Flatley *et al.*[10] found that the reaction kinetics are initially linear followed by a parabolic period. When the gas flow rate was increased, the initial linear reaction rate was found to increase, and the duration of this stage to decrease (*i.e.*, the change to parabolic kinetics occurred earlier). The effect of both P_{SO_2} and flow rate together suggests that the initial linear reaction is controlled by diffusion of SO_2 through a boundary layer in the gas. Eventually, cation diffusion becomes the rate controlling step and parabolic kinetics are observed. The fast corrosion rates are due to sulfide formation particularly in the form of lamellae within the iron oxide.

The larger the oxygen potential of the atmosphere, the sooner a protective

oxide layer is formed. For a given SO_2 content, this condition is reached sooner as the flow rate of the gas over the specimen surface is increased. The most damaging attack was found with low SO_2 concentrations and low flow rates. Such conditions may be found in stagnant pockets of gas, such as in pores or beneath deposits. In these positions, the oxygen potential of the gas will be reduced to very low values whatever the oxygen content of the bulk atmosphere.

Rahmel[2] studied the reaction mehcanism on pure Fe in $N_2-O_2-SO_2$ and $CO-CO_2-COS$ mixtures between 700 and 900°C. In the absence of the second oxidant (SO_2), choosing N_2-O_2 (< 1%) as reaction gas, linear oxidation kinetics were observed as the growth of an Fe_xO layer was limited by the transport of O_2 through a stagnant gaseous boundary layer. As SO_2 was added to the gas, both FeS and FeO formed as an aggregate product (see Figure 3) with increased linear kinetics so long as the reaction was controlled by transport in the gas phase. On the other hand, when the oxygen content was higher (> 10% O_2), the kinetics were found to be parabolic and controlled by diffusion through an iron oxide scale. Under these circumstances, the introduction of up to 5% SO_2 did not affect the parabolic kinetics (see Figure 4), nor was FeS formed.

In the somewhat analogous reaction of pure Fe with $CO-CO_2-COS$ gases, the simple formation of FeS from COS or of FeO from CO_2 is limited by an interfacial reaction step - the breakup of the reactant molecule - and linear kinetics are observed. When the second oxidant is introduced in either case, both the sulfide and oxide are formed in an aggregate scale with increased linear kinetics (see Figure 5). Again, the parabolic (diffusion controlled) growth of the oxide or sulfide is not influenced by the presence of minor amounts of the second oxidant.

Rate Determining Steps

Now, let us examine what effects the nature of the rate controlling step might have on scale morphology and reaction kinetics.

The possible rate controlling processes are:

a. Reaction at the *Fe*/scale phase boundary (change over of iron ions and electrons from the metal to the scale)

$$Fe \rightarrow Fe^{++} + 2e^{-}$$

b. Diffusion in the scale (diffusion of cations or anions via vacancies or interstitials and migration of electrons by one of several possible processes)

c. Reaction at the scale/gas phase boundary (dissociation and ionization of the oxidizing agent and growth of the lattice of the scale)

$$SO_2(g) + 6e^{-} \rightarrow S^{=}_{(ads)} + 2O^{=}_{(ads)}$$

d. Diffusion in the gas (transport of the oxidant from the gas stream to the surface of the scale)

Rahmel[2] rationalized and generalized these observations as follows:

1. When linear kinetics result from rate control at or ahead of the scale/gas interface, then the scale is not in equilibrium with the contacting gas and will react with additionally available oxidants.

2. When diffusion control in the scale results in parabolic kinetics, then the scale equilibrates with the reacting gas mixture at the scale/gas interface to exclude any influence of a less reactive second oxidant. The results are summarized in Figure 6.

When alloys, such as iron-chromium alloys, are exposed to sulfur dioxide containing atmospheres[11], normally, a layer of protective scale based on iron-chromium spinel or chromium oxide is formed initially, and the reaction rate is much slower at the early stage. Depending on the chromium content, the early

passive stage, also known as *incubation time*, is in a range of seconds to hours for chromium content from 1% to 20%. Eventually, the protective scale will be destroyed by the penetration of sulfur and an accelerated kinetics will be observed. Currently, however, there is no general rule to predict the transition of reaction kinetics.

2.6. Porous Structure

In many studies[5] of sulfidation, the scales have been observed not to be compact, but to have a porous inner layer. Inert markers are observed at the boundary between the two layers of the scale. Birks[4] and Mrowec[5] proposed a *dissociation mechanism* to account for the formation of this porous layer. It is suggested that as the scale thickens and becomes more rigid, it is unable to deform with the contracting metal core, so the scale begins to lose contact with the metal substrate. In addition, the injection of vacancies into the substrate may condense to form pores at the scale/metal interface. As a result of the formation of this gap, the rate of transport of metal ions to the scale decreases. However, because of the chemical potential gradient and the defect concentration gradient, the sulfide may begin to decompose. The metal ions migrate out through the scale and the sulfur gas diffuses across the gap to sulfidize the metal below. Consequently, the inner layer becomes porous.

An alternative explanation due to Atkinson *et al.*[6] to account for the formation of a porous inner layer in *NiO* proposes that the inner porous layer simply is formed by the inward transport of oxygen through microcracks incorporating any porosity which has formed at the scale/metal interface. However, the details of this mechanism have not been developed.

2.7. Influence of Alloying Composition

Alloying elements, employed to improve the strength or other properties of a metal, can influence the oxidation behavior in several ways. The second alloying component may enter the scale, affecting its lattice defect structure, or may accumulate as metal or oxide beneath the main scale. Since alloy components have different affinities for oxygen and often do not diffuse at the same rate in the oxide or in the alloy, the simple kinetic rate equations are occasionally not followed and the scale and alloy compositions may change in a complex way with time. A moderate content of a nonoxidizable metal (*e.g.*, 10 $w/_o$ gold in copper) produces little change in the oxide layer (Cu_2O) and therefore usually has little effect on the rate of oxidation although it could change a_{Cu} at the scale/metal interface. However, if the oxides of the alloying constituents have widely different values of free energy of formation, the least noble element in an alloy will be preferentially oxidized to the exclusion of all other possible oxide phases. This phenomenon is called *selective oxidation*, and was recently reviewed by Crouch and Scully[22] with particular reference to the *Fe-Cr* system.

A typical example of the beneficial effect of selective oxidation occurs in *Cu* alloys containing 2 ~ 10 $w/_o$ *Al*. Initially a layer of Cu_2O forms at a rapid rate, but soon a protective layer of Al_2O_3 forms at the metal/oxide interface and prevents the Cu^+ ions from reaching the oxide/oxygen interface. Oxidation then virtually ceases. Chromium acts in an analogous manner to protect iron-chromium alloys from oxidation by forming a protective Cr_2O_3 layer. In the oxidation of some alloys, a compound oxide may form and be effective in limiting the rate of oxidation. The $MgO \cdot Al_2O_3$ spinel, which is stoichiometric, forms on aluminum-magnesium alloys and gives excellent protection. However, many spinels, such as $ZnO \cdot Al_2O_3$ and $FeO \cdot Fe_2O_3$, are cation-defective and permit oxidation to continue.

In some cases, if oxygen can diffuse into the alloy in atomic form, precipi-

tation of the oxide of the less noble metal may occur as internal oxide. This process, called *internal oxidation*, can be expected if the volume fraction of the oxide of the less noble metal is below a critical value: for the *Ag-In* case, Rapp[23] showed this critical value was about 0.3%. The internal oxidation is usually undesirable. In suitable alloys, however, the interal oxide particles can be employed as a method of strengthening. Figure 7 provides a summary of most of the common forms of binary alloy oxidation.

Several alloying elements, including *Al* and *Si*, increase the resistance[24] of iron to corrosion and oxidation, but chromium is of outstanding importance. Chromium improves the oxidation resistance[24] and also the resistance to aqueous corrosion in most media (with the notable exception of chloride solutions and strong, nonoxidizing acids). The iron-chromium phase diagram (Figure 8) shows that a significant change in structure occurs when iron contains more than 13 $w/_o$ *Cr* and lies beyond the "γ loop." The alloys are then ferritic (α phase) at all temperatures and are no longer able to under go the $\gamma \rightarrow \alpha$ transformation that leads to martensitic hardening. Depending on the chromium and carbon contents (Figure 9), chromium steels may be hardenable by heat treatment, as are alloy steels (martensitic stainless), or they may be nonhardenable (ferritic stainless) but possess superior corrosion resistance because of a higher chromium content.

When nickel is added to a steel containing enough chromium (about 18 $w/_o$) for good corrosion resistance, the corrosion resistance is further improved, but the principal effect is to change the steel from ferritic to austenitic (Figure 10) at nickel contents above 6.5 $w/_o$. Once the austenite has formed at high temperatures, it may persist during slow cooling to room temperature. Austenitic steels of the *18Cr-8Ni* type possess an excellent combination of corrosion resistance, ductility for easy forming, and strengthening possibilities. Cold working

of these steels can produce an unusual degree of strengthening because the austenite tends to decompose to ferrite and produces a martensitic-type constituent.

A limiting factor in the use of iron-chromium alloys is the spallation of protective scale. According to Wood and Whittle[25], the Cr_2O_3 scale on iron-chromium alloys in oxygen at 800°C or up becomes detached from the alloys in random areas and tends to arch outwards because of the stresses that develop during oxide growth. Cracking of this oxide scale exposes areas of Cr-depleted surface to oxygen and leads to the formation of iron-rich nodules and accelerated oxidation of alloys. When the cavity under the lifted Cr_2O_3 scale is full of growing oxide, the Cr_2O_3 roof could crack off and allow unimpeded growth of the nodular oxide. The addition of sulfur dioxide resulting in the buildup of a sulfide layer at the scale/alloy interface makes the spallation all the more serious.

Apart from the disadvantage of producing films which do not have self-healing qualities, selective oxidation can be superior to other protective-coating systems because it can be applied to any geometry of component, it produces a naturally grown oxide with good adhesion, and it is also a relatively cheap process. But the required amount of oxide-forming element may not be acceptable on the grounds of mechanical properties.

2.8. Scanning Auger Microscopy

The Auger effect was discovered by Auger[26] in 1925, however, it was much later that Lander[27] proposed measurement of electron excited Auger electrons in ultra-high vacuum (UHV). Harris[28], in 1968, proved how surface sensitive the technique was by measuring the differentiated (dN/dE) energy spectrum. Weber and Peria[29] showed how AES could be performed with a standard low

energy electron diffraction (LEED) apparatus and Palmberg *et al.*[30] demonstrated improved sensitivity and measurement speed utilizing a cylindrical mirror analyzer (CMA).

More recent developments have produced AES analytical instruments that have general application in materials analysis. Auger electrons produced by finely focused electron beams (< 500Å) rastered over the surface can be synchronously detected to create 2D surface chemical maps[31]. Beams of inert ions can be directed at surface to sputter surface layers. Simultaneous monitoring of the Auger electron signals while sputtering generates compositional depth profiles.

In this investigation, Auger measurements were carried out in an ion-pumped UHV system capable of reaching a pressure of 0.107 μPa with bakeout. The spectra were taken with a Physical Electronics Industries (PHI) Model 25-110 single pass CMA.

Approximate chemical compositions were calculated from the Auger spectra before and after sputtering by measuring peak-to-peak heights of the constituent element signals: *S* (151 eV), *Al* (1380 eV), *Cl* (179 eV), *C* (270 eV), *O* (510 eV), *Cr* (529 eV), *Fe* (700 eV). Elemental compositions were calculated using the following formula:

$$C_x = \frac{K I_x S_x^{-1}}{\sum_i I_i S_i^{-1}}$$

where I_x is the Auger peak-to-peak height for a specific Auger transition, S_x is a relative elemental sensitivity factor taken from the PHI Handbook, and K is a matrix correction factor. Accurate chemical composition can be obtained only if the *matrix effects* are taken into consideration. These matrix effect factors are associated with the electron escape depth, backscattering, and peak shape. The last factor results because the chemical environment causes the peak

shape to change. These peak shape changes are pronounced with the valence electron transitions. In the present study the value for K is not available and we have assumed it to be 1.

CHAPTER III

INTRODUCTION TO PRESENT WORK

This research is to investigate the corrosion mechanism of iron and iron-based alloys in coal-combustion atomspheres. For most combustor operations, the product gas will be oxidizing in nature, and the oxidizing potential is largely controlled by the excess air used in combustion.

In order to study the mixed sulfidation and oxidation attack, it is necessary to control the experimental conditions so that simultaneous oxidation and sulfidation can occur. According to previous work[3], the most damaging attack of simultaneous oxidation and sulfidation was found with low SO_2 concentrations and low flow rates. As a consequence, two gas mixtures were used: CO_2–10%SO_2 and air-1%SO_2. These gas mixtures equilibrate, at 871°C, to complex atmospheres containing the species CO_2, SO_2, O_2, S_2, CO, COS, SO_3, CS, CS_2, and SO. The partial pressures of these species can be computed from thermodynamic data and are listed in Appendix B. The air-1%SO_2 mixture was used as a comparison for corrosion behavior in high oxygen partial pressure gases. The experimental temperature, 871°C, is chosen just below the liquid phase formation temperature to avoid the complications due to liquid formation.

Points A and B of Figure 11 represent the equilibrium gas mixtures of CO_2–10%SO_2 ($P_{O_2} \approx 10^{-8.7}\,atm$, $P_{S_2} \approx 10^{-10.1}\,atm$) and air-1%$SO_2$ ($P_{O_2} \approx 10^{-0.1}\,atm$, $P_{S_2} \approx 10^{-28.9}\,atm$) respectively. From this diagram, it is obvious that P_{S_2} of CO_2–10%SO_2 is below the Fe-FeS, $Al-Al_2S_3$ and $Cr-Cr_2S_3$ equilibrium lines, *i.e.*, no sulfide is stable in contact with the gas from a thermodynamic point of view. However, the experimental results show that sulfide exists in the scale. The exploration of this phenomenon is one of the main purposes of the present research.

Moreover, the protective nature of an oxide scale can be destroyed due to the spallation of oxide on repeated thermal cycling or on exposure to sulfur-containing atmospheres. In this study, however, much concern is given to the penetration of sulfur through the oxide scale which leads to the sulfidation of the base metal and rapid failure of the alloys.

In summary, this study is to investigate the high temperature behavior of pure iron and iron-based alloys in a CO_2–10%SO_2 gas mixture. The scale growth mechanism was proposed on the basis of careful examination of the initial experimental results and confirmed by further experimental evidence.

CHAPTER IV

EXPERIMENTAL PROCEDURES

The experimental procedure consisted essentially of reacting a range of *Fe-Cr*, *Fe-Al*, and *Fe-Cr-Al* alloys in the two atmospheres at 871°C for times up to 700 hours.

The pure iron and iron-based alloys used in this investigation were melted in an induction furnace under an argon atmosphere, cast into ingots, and subsequently homogenized at 1200°C for 24 hours. The castings were cut into 1x1x0.3 *cm* coupons. The compositions of the specimens determined by chemical analysis are listed in Appendix C. The surfaces of the specimens were prepared immediately before each run by grinding them down to 600 grade carborundum paper followed by washing in acetone.

There were two groups of experiments. In one, specimens were exposed for predetermined times in a horizontal tube furnace and removed for examination; in the other, the kinetics of the reaction were determined thermogravimetrically in a vertical tube furnace using a Cahn microbalance. The horizontal furnace had a mullite reaction tube: the specimen was placed in an alumina boat in a cool part of the reaction tube, and the assembly was flushed with argon containing an estimated 1 *ppm* oxygen impurity. The specimen holder was then moved into the hot part of the furnace, and the argon was replaced by the reaction gas at a flow rate of approximately $1.5 \times 10^{-6}\ m^3/sec$.

The surface topography and composition of the oxidized samples were examined using a Scanning Electron Microscope (SEM) fitted with an energy dispersive X-ray (EDX) analysis facility. Scale products were also characterized using X-ray diffraction (XRD) and Scanning Auger Microscopy (SAM). Cross-sections of the corroded specimens were examined using conventional metallo-

graphic techniques.

CHAPTER V

TRANSPORT OF SULFUR

Virtually, all fossil fuels contain sulfur as an impurity and when they are burned - whether in a turbine, in fluidized beds, or in conversion processes such as coal gasification or liquefaction - they generate atmospheres that contain sulfur compounds. The use of metallic alloys in such environments at elevated temperatures often leads to a ***breakaway*** phenomenon in which the oxide scale loses its protectiveness and unacceptedly high rates of metal wastage ensue. Generally, the cause of the breakaway is related to sulfur penetration through the growing oxide scale, resulting in formation of sulfides both within and below the scale, although the detailed mechanism has not been unequivocally demonstrated. Pre-forming of the protective oxide in a sulfur-free atmosphere may delay the breakaway, but does not eliminate it.

In order to design and use high temperature alloys effectively in these systems, an experimental or theoretical prediction of the time at which breakaway will occur as a function of the temperature and the corrosion environment is required, so that the alloys can be operated only in regimes in which there is a high probability that breakaway will not occur during their required service lifetimes. At present, the mechanism for the transport of sulfur through the oxide scale is not understood, and as a consequence, alloys can only be safely used under the assumption that breakaway corrosion will occur from the beginning of operation. This, of course, leads to an over-conservative uneconomical design.

Generally, two distinct mechanisms for sulfur transport through the oxide are considered[3]:

(i) dissolution of sulfur in the scale and subsequent solid state diffusion inwards either via a lattice or grain boundary route to the scale/alloy interface;

(ii) penetration of sulfur in molecular compound form through physical defects in the scale such as pores, cracks, or even grosser defects such as might prevail if substantial spallation of the protective oxide occurred.

The details of the mechanism are important, since they dictate the appropriate remedy. The following two experiments identify the mechanism of sulfur transport through iron oxide scales and in a chromium matrix respectively, and thus help to provide a basis for the prediction of breakaway of alloys.

5.1. Sulfur Diffusion In Iron Oxide

Pure iron samples in the form of 2x0.3x0.1 *cm* coupons were notched to assure the position of the fracture of the specimens. The samples were completely oxidized in air for 2 days at 871°C; this avoids the ductile fracture of iron on subsequent breaking. The completely oxidized samples were then exposed to a H_2-10%H_2S atmosphere ($P_{S_2} \approx 10^{-5} atm$) at 871°C for 1 minute. This short exposure time was chosen so that sulfur could penetrate into the scale, but substantial sulfide formation would not be expected. After exposure, the sample was fractured inside the vacuum chamber of the SAM to avoid any contamination.

Figure 12(a) shows the impact fractured cross-section of the scale. The left side of the micrograph shows a region of intergranular fracture, whereas the right side shows areas where fracture has occurred intragranularly. Figure 12(b) is the sulfur Auger electron map of Figure 12(a). Comparing these two pictures, it is clear that sulfur is only present along the grain boundaries of the

scale. This is further confirmed by Figure 13(a), (b) which are the corresponding images and sulfur Auger electron map of the same area after argon ion sputtering for 5 minutes. It is evident that all the sulfur has been sputtered away and that it existed only at the grain boundary. Figures 14(a), (b) are the Auger electron energy surveys at Point 1 and Point 2 shown on Figure 13(a) before argon ion sputtering. The 150 e.V. peak of sulfur existing only at Point 2 confirms that sulfur exists at grain boundary, but not in the grain. Figures 15(a), (b) are the intensities of the sulfur, oxygen and iron peaks composition depth profiles at Point 1 and Point 2 of Figure 13(a) respectively during the 5 minutes argon ion sputtering. They indicate that sulfur at Point 2 disappears after the first half minute sputtering, *i.e.*, the thickness of the sulfur layer covering the grain boundary is less than 200Å (Argon ion sputtering rate is approximately 400Å/*min.*)

Based on these results, it is concluded that sulfur can penetrate through iron oxide scale via grain boundary diffusion.

Even in this very short exposure, 1 minute or a maximum of 2 minutes, if the time taken for the sample to cool from the reaction temperature is included, sulfur has managed to penetrate completely through the 1 *mm* thick sample. This indicates an effective diffusion coefficient of the order of at least $10^{-4} cm^2/sec$. This is considerably higher than reported diffusivities of sulfur in wüstite[32]: $10^{-7} cm^2/sec$ at 1300°C[33] and 4 x $10^{-8} cm^2/sec$ and $10^{-6} cm^2/sec$ at 1050°C and 1250°C respectively. Whether the value implied by the present result represents a grain boundary diffusion coefficient, or a gaseous coefficient through fine pores at the boundaries remains in question.

5.2. Sulfur Diffusion in Pure Chromium/Chromium Oxide

In order to examine the mechanism of sulfur penetration through the

chromium/chromium oxide and the reduction of chromium oxide by the hydrogen, pure chromium (99.9% Cr) in the form of 3x0.25x0.25 cm coupons was oxidized in air for 17 days at 1000°C, and subsequently exposed to H_2–10%H_2S ($P_{S_2} \approx 10^{-4}\,atm$) for 10 minutes at 1000°C. After exposure, the sample was fractured inside the vacuum chamber of SAM, to avoid any contamination of the fractured surface.

It is expected that protective chromium oxide will slow down the sulfidation attack by limiting penetration of sulfur into the chromium matrix, however, examination of the fractured surface revealed that the chromium oxide had not been reduced by the hydrogen, but had nevertheless failed to suppress sulfur penetration. The retention of the chromium oxide and concentration of sulfur at the scale/metal interface indicate that the sulfur transport through the chromium oxide was via short-circuit paths. Furthermore, it is observed that a significant amount of sulfur penetrated into the chromium matrix. Figure 16(a) shows the fractured cross-section of the center part of the specimen, Figure 16(b) is the corresponding sulfur Auger electron map. It is likely that sulfur is observed only on some of the grains where intergranular fracture occurs. However, after 2 minutes argon ion sputtering, most of the sulfur was removed as shown in Figure 16(c), indicating that the sulfur layer is rather thin. Based on an argon sputtering rate of 1000Å/min, the approximate thickness of this sulfur penetration layer is 3000Å. Such a thin sulfur layer in the chromium matrix confirms that sulfur transport is via grain boundary diffusion. There are several areas in Figure 16(c) which still show a strong sulfur content. This is probably due to a geometric effect, with topographical features shadowing the surface and penetrating access of the argon ions. Figures 17(a), (b) are the Auger spectrum and the compositional/depth profile at Points 1 and 2 of Figure 16(a). The analyses at both locations show similar results. A nitrogen peak

appears in Figure 17(a) suggesting that nitrogen, as well as sulfur, can penetrate through a chromium oxide. This is consistent with previous data produced by Pettit *et al.*[1] They observed a layer of Cr_2N beneath Cr_2O_3 in the reaction of pure chromium in air at 1200°C. However, the diffusivity and reaction kinetics of nitrogen with chromium are presumably much lower than those of sulfur with chromium, since the sample was exposed to air for 17 days, but exposed to a H_2-10%H_2S atmosphere only for 10 minutes. The gradually decreasing sulfur concentration as shown in Figure 17(b) indicates that sulfur penetrates along grain boundaries first and then diffuses into the grains.

In this short exposure, sulfur managed to penetrate completely through the 2.5 *mm* thick sample via grain boundary diffusion. A penetration depth of 1.25 *mm* within 10 minutes indicates an effective diffusion coefficient of the order of at least $10^{-5}\,cm^2/sec$. Figure 17(b) is the diffusion profile of sulfur from the grain boundary into the grain. If it is assumed that a constant boundary layer containing approximately 38 $a/_o$ sulfur is formed at some time after the first minute, but before the last minute of exposure so that the penetration time of sulfur into the grain is between 1 and 9 minutes; then by using the profile in Figure 17(b) and Fick's diffusion equation:

$$c(x,t) = C_b[1 - erf(\frac{x}{2\sqrt{Dt}})]$$

where C_b is the sulfur concentration at the boundary layer, x is the distance, D is the diffusion coefficient and t is the time, the corresponding diffusion coefficient of sulfur in the chromium lattice may be calculated as between 10^{-12} and $10^{-14}\,cm^2/sec$ at 1000°C.

This result is consistent with the observation made by Perkins *et al.*[33] They reported that sulfide particles have been found beneath a thin Cr_2O_3 scale formed on Type 310 stainless steel exposed to a H_2–H_2O–H_2S mixture at 871°C for 48 hours. The chromium sulfide particles formed preferentially at the metal

grain boundaries and twin boundaries which intersect the alloy surface. The particles are very thin (less than a few microns thick) and generally can not be detected in polished cross-sections of the scale metal interfaces, even at 3000X magnification.

In summary, sulfur can penetrate rapidly through the chromium oxide scale via short-circuit path and into the chromium matrix via grain boundary diffusion. The sulfur in the grain boundaries then penetrates into the grains at a very low diffusion rate.

CHAPTER VI

HIGH TEMPERATURE CORROSION OF IRON IN CO_2–10%SO_2 ATMOSPHERES

In this study, most of the pure iron samples were exposed to a CO_2-10%SO_2 atmosphere which at equilibrium gives a $P_{S_2} \approx 10^{-10.1}\,atm$, a $P_{O_2} \approx 10^{-8.7}\,atm$ and $a_c \approx 10^{-9.3}$ at 871°C. The activity of carbon is too low to cause any carburization, and thus only sulfidation and oxidation problems are encounted.

6.1. Results

Reaction Kinetics

The reaction kinetics of pure iron exposed to a CO_2–10%SO_2 atmosphere were determined by thermogravimetric analysis. Parabolic kinetics were observed during the latter stages of growth. Initial growth rate (within the first 2 hours) was linear as shown in Figure 18. When the gas flow rate was increased, the initial linear reaction rate was found to increase, and the duration of this stage to decrease (*i.e.*, the change to parabolic kinetics occurred earlier.) The parabolic rate of iron exposed to CO_2–10%SO_2 falls between the rate of pure sulfidation and the rate of pure oxidation as shown in Figure 18. The reaction kinetics of pure iron exposed to an air-1%SO_2 atmosphere were the same as those for iron subjected to simple oxidation in air.

Scale Morphology

After pure iron was exposed to a CO_2-10%SO_2 atmosphere for 3 hours, a large number of protrusions were observed to grow outward from the scale surface as shown in Figure 19. The diameters of some of these protrusions are over 50 μm. These protrusions are irregular, non-crystallographic, randomly oriented and with branches. The number and size of the protrusions decrease

with time. Closer examination reveals that wrinkles, which look like a pattern of ridges, spread all over the protrusions and the scale surface. Figure 20 unveils that these wrinkles grow along the grain boundaries of the scale. A sulfide-rich core runs through the center of a protrusion as seen in Figure 21. Oxide grains surrounding the sulfide-rich core appear to grow radially out of the sulfide-rich core.

A fractured cross-section of the scale stripped from the metal mechanically by quenching in liquid nitrogen reveals that the outer layer is composed of oxide grains and sulfur-rich grains. Some small pores exist in the outer layer. As for the inner layer, it is mostly porous, particularly near the scale/metal interface. The pores in the inner layer seem interconnected as shown in Figure 22. Beneath the inner layer, there exists a layer of large grains at the scale/metal interface. Figure 23 is the bottom view of the scale. By comparing with the sulfur map, it is clear that many small grains which look like nuclei spread on the left side of Figure 23, *i.e.*, the sulfur-rich area. These nuclei are on the underside of the large-grained layer which is much denser than the porous inner layer. Figure 24 is the top view of the metal surface after the scale was removed. The metal surface shows the scale grains imprint which is an indication of good contact of scale and metal. However, some voids may also exist at the scale/metal interface.

Sectioned and polished specimens were examined. A typical optical microscopic section is shown in Figure 25. The scale/metal interface is relatively uniform, whereas the scale/gas interface is irregular. Near the scale/gas interface, the scale consists of different phases. White streaks and spots which are rich in sulfur are distributed in a gray magnetite matrix. There are sometimes long streaks extending as protrusions on the surface of the scale. Sometimes there are no sulfide streaks beneath the protrusions. The observation of

sulfide streaks below the protrusion depends on whether the section cuts through a protrusion. In the inner regions of the scale, the sulfide particles are smaller and not so obvious as the outer layer. The porosity of this inner layer is shown in Figure 22. It is hard to differentiate the two phases in this layer because there are no distinct contrasts, but presumably the sulfide phase is intimately mixed with the wustite rather than the more distinguishable distribution in the outer layer.

Based on the above observations, the morphology of the scale exposed to a CO_2-10%SO_2 atmosphere is drawn in Figure 26.

Scale Microstructure

The scales were further analyzed by using SAM and XRD. Figures 27(a)-(d) are some of the SAM analyses. Figures 27(a), (b) show the composition/depth profile of a sulfur-rich grain and of an oxide grain respectively. These were produced by using an argon ion sputtering rate of 400Å/*min*. They demonstrate that the sulfur-rich grain contains a high concentration of oxygen (at least 10 $a/_o$) whilst a slight amount of sulfur is detected in the oxide matrix. Figures 27(c), (d) are the other two SAM analyses of the inner layer grains. It is noted that these SAM results are not typical, and are actually very sensitive to position: close to the scale/metal interface, the sulfur content increases gradually. The core of a protrusion was also examined by SAM. A similar composition/depth profile was obtained, approximately 20 $a/_o$ sulfur and 40 $a/_o$ oxygen. Neither pure sulfide nor pure oxide was detected. Since the SAM has a resolution of approximately 1 μm, the sulfur is present either as a solid solution in the oxide or as a very fine second phase. The XRD results suggest that the latter is the case.

6.2. Discussion

Thermodynamic Consideration

The thermodynamic phase stability diagram for *Fe-S-O* system at 871°C is shown in Figure 28[32]. Point A represents the environment to which the specimens were exposed. According to this equilibrium diagram, sulfide is not a thermodynamically stable phase in contact with a CO_2-10%SO_2 gas mixture, nor is the sulfur potential of the gas high enough to form the iron sulfide. The existence of sulfide in the scale indicates, however, that the sulfur activity must be increased somehow, probably because oxygen is consumed by the reaction with metal ($P_{O_2} \approx 10^{-8.6} atm$), and as a consequence, the sulfur activity is increased. The reaction can be expressed as:

$$SO_2 \rightarrow \frac{1}{2} S_2 \uparrow + O_2 \downarrow$$

In order to further explore this depletion phenomenon, it is important to establish how the composition of the CO_2-10%SO_2 gas mixture, assuming that it is always at equilibrium, will change when one of the components is removed from the gas by reacting with the metal. Especially, the effect on the activities of oxygen and sulfur reactants should be considered.

Equilibria of the *S-O-C* gas system have been calculated by Pope *et al.*[34] A combination of an *Ellingham-Pourbaix-type* diagram and a CO_2−10%SO_2 gas system equilibrium diagram is shown in Figure 28. The interdependencies between sulfur and oxygen potentials have a considerable influence on the corrosion behavior. For example, a gas mixture equilibrated in the oxide region (Point A) might shift into a sulfide stable region (Point B) when oxygen is consumed by reacting with the metal. In other words, during the formation of an oxide phase contiguous to the metal, local equilibria may be set up temporarily at the scale/gas interface or internally within the scale, such as within pores, which deviate greatly from the bulk gas phase and thereby allow the formation

of sulfide.

In the first case, the change of thermodynamic equilibrium to a sulfide stable region by reaction on the specimen surface would imply that diffusion of the oxidant through the gas phase to the scale/gas interface is the rate determining step. This implication is in agreement with a linear reaction rate which was observed as described in the experimental results. The formation of sulfide, which can cause the depletion of sulfur for the same reason, shifts the thermodynamic equilibrium back to the oxide stable region, *i.e.*, the gas composition near the scale surface fluctuates between a sulfide stable region and an oxide stable region. In addition, the reaction rate is so fast that an oxide/sulfide duplex structure is formed rather than the separate grains of oxide or sulfide. The formation of sulfide is very sensitive to the depletion of oxygen. As the scale thickens, the transport rate of cations is limited, therefore, the depletion of oxygen becomes more difficult, and as a result, there is less tendency for sulfide to be formed. Therefore, sulfur concentration decreases from the scale/metal interface to the scale/gas interface.

However, Figure 28 is plotted on a log scale, therefore, the change of P_{O_2} from Point C to Point B is very much greater than from Point A to Point B, *i.e.*, the amount of oxygen which must be removed in order to reach the sulfide-stable region (*e.g.*, Point B) will be much greater from Point C rather than from Point A. This accounts for the experimental result in which the reaction kinetics of pure iron exposed to an air-1%SO_2 atmosphere (equilibrium at Point C) is the same as the rate of oxidation in the air, for it is impossible to deplete the oxygen locally in this case. As a further consequence, no sulfide was observed in the scale.

As an alternative for the reaction at the surface of the scale producing depletion of oxygen, there is also a possibility of a change in thermodynamic

equilibrium to a sulfide stable region due to the reaction within the scale, providing gas transport through the scale occurs via physical defects (*e.g.*, cracks or pores). To determine the predominant reaction, an iron sample of 3 mm thickness was completely oxidized in CO_2-37%CO for 2 days, and subsequently exposed to CO_2-10%SO_2 for 3 hours. The porous iron oxide formed in the first stage was further oxidized to a lower iron activity equilibrating with CO_2–10%SO_2 in the second stage, as shown in Figure 28, from Point D to Point A. According to the gaseous transport theory, SO_2(g) can penetrate into the oxide scale via pores or cracks very rapidly, thus sulfide should be formed uniformly throughout the scale or concentrated in the center of the scale. However, sulfide was concentrated near the scale surface, as shown in Figure 29. This result indicates that the diffusion of iron ions to the scale/gas interface is more significant and faster than the transport of SO_2(g) into the scale, *i.e.*, the depletion of oxygen at the scale/gas interface is predominant in sulfide formation. As a reference, a similar iron sample was completely oxidized in CO_2 for 2 days, subsequently exposed to CO_2–10%SO_2 for 3 hours, as shown in Figure 28 from Point E to Point A. Under these conditions, the P_{O_2} remained the same, *i.e.*, no change in iron activity, accordingly no sulfide was formed in the scale after the second exposure. This experiment confirms that the change of iron activity is essential for the formation of sulfide.

The Irregularities of the Scale

As mentioned earlier, after exposure of pure iron to a CO_2–10%SO_2 atmosphere, there are two kinds of irregularities in the microstructure of the scale. The larger irregularities are the protrusions; the smaller ones are the wrinkles formed on the surfaces of the scale and the protrusions. These irregularities are not observed in either pure sulfidation or pure oxidation, where the scale surface usually forms some type of crystallographic facetting. For this reason,

they must be related to a specific growth mechanism.

The formation of protrusions on the scale is explained by the following mechanism (see Figure 30):

Stage 1

As discussed earlier, during the exposure of pure iron to CO_2-10%SO_2, the gas layer adjacent to the metal becomes enriched in sulfur vapor due to the depletion of oxygen consumed by oxidation at the sites of high iron activity. Consequently there is a local change of the gaseous equilibrium from an oxide stable region into a sulfide stable region leading to the formation of sulfide. In this case, the reaction rate is limited by diffusion in the gaseous phase and a linear kinetic rate is observed as shown in Figure 18. It is observed that the initial linear reaction rate increases as the gas flow rate increases and the duration of this stage decreases (*i.e.*, the change to parabolic kinetics occurred earlier). This effect of flow rate excludes the possibility that the rate determined step is the reaction at the scale/gas phase boundary which also leads to a linear kinetics.

Stage 2

The existence of sulfide is very sensitive to the depletion of oxygen. Basically, the depletion of oxygen is due to cation transport in the scale being faster than oxygen transport from the bulk gas to the scale/gas interface. The most possible area where oxygen is easily depleted is over a pre-existing sulfide-rich area, since iron cations transport faster through this than through the oxide[3]. A higher iron acitivity might thus be expected to exist in the sulfide-rich area (*i.e.*, a surplus of iron ions waiting for the possible reaction), leading to a more rapid reaction and hence a faster growth rate than the surrounding oxide. This phenomenon insures that once the sulfide forms, a depleted atmosphere always surrounds it; any available oxidant, either sulfur or

oxygen, will react with the iron ions at the top of the protrusion to form sulfide or oxide, so that the protrusions will continue to grow in the undepleted bulk atmosphere rather than spreading laterally. In other words, scale/gas equilibrium has not been achieved at the surface of sulfide-rich areas, and the gas composition fluctuates locally between sulfide and oxide stable regions. This leads to the continuous formation of a sulfide and oxide lamellar structure at the original sulfide-rich areas on the surface of the scale.

However, due to the local fluctuations in gas composition, it is also possible for adsorbed sulfur to form sulfide nuclei on the surface of oxide, thus inducing new depletion areas. An indication that this can also be a contributory factor is demonstrated by the following experiment: Pure iron was pre-oxidized in air for 3 hours, then exposed to a CO_2-10%SO_2 atmosphere for 1 hour. Protrusions were present evenly over the surface with a relatively uniform oxide layer beneath them. The existence of these protrusions, which had sulfide-rich cores, indicates that sulfide can nucleate on the oxide surface, thus inducing local depletion. A further possibility is that sulfur can penetrate along the grain boundaries of the oxide[35] to the scale/metal interface and thus enhance the diffusion of iron ions. The presence of sulfide as a constituent of a scale provides a mechanism for very rapid ionic transport through the scale, this is particularly so if the sulfide is present as a continuous network throughout the grain boundaries of the scale.

Stage 3

It should be noted, however, that sulfide is not a thermodynamically stable phase in equilibrium with the bulk gas, and that eventually oxide will be formed when the composition of the atmosphere surrounding the protrusions approaches that of the atmosphere of the bulk gas due to transport of oxidants such as CO_2 or SO_2 to the scale surface. Three possibilities of oxide formation

are suggested as follows:

Step A: oxide is formed on the top of a sulfide protrusion, resulting in the development of branches on the protrusion due to the blockage of the rapid iron transport by the oxide.

Step B: oxide surrounds a protrusion, thus the sulfide-rich cores will continue to grow.

Step C: oxide covers the sulfide-rich core, thus the protrusion will be buried as the surrounding oxide grows around it.

Stage 4

As a result of the surrounding oxide growing with the protrusions, the long streaks of sulfide and oxide lamellar structure are formed. Also, some sulfide-rich streaks are buried inside the scale, and some isolated sulfide-rich grains covered by oxide are randomly distributed within the scale as shown earlier in Figure 25.

The proposed mechanism is consistent with the following facts:

a. No protrusions are formed in pure sulfidation or oxidation for neither local fluctuation in surface gas composition between sulfide and oxide stable regions, nor local diffusion rate differences caused by sulfide within the scale can occur.

b. No protrusions are observed when iron is exposed to an air-1%SO_2 atmosphere, since depletion of oxygen is insignificant.

c. As the exposure time increases, the number and size of protrusions decrease, because the outward transport rate of cations is limited by the thickening scale, *i.e.*, the differences between sulfide-rich and oxide-rich areas diminish.

d. The number of protrusions is less at the edges of the specimen. Since at the edges, depletion is less likely.

In order to confirm the mechanism, illustrated in Figure 30, it is important to identify the sulfide-rich active centers. However, no sulfur was detected by SEM or SAM at the heads of the protrusions. It is believed that these active centers are covered with oxide during the cooling stage, following the experiment, by oxygen impurities within the argon gas used for flushing the reaction chamber. Consequently, a specimen was cooled down in a sulfur-containing atmosphere (CO_2-10%SO_2) instead of the argon atmosphere. This time, the SEM and EDX pictures (see Figure 31) revealed the existence of sulfide at the heads of the protrusions. They developed a flower-like appearance at their heads indicating that the protrusions grew fast. This experiment confirms that the protrusions are formed by rapid ionic transport through the sulfide-rich areas.

Figure 32 portrays a fractured section through a protrusion, with a sulfide-rich core, which is surrounded by many oxide grains formed during the argon flushing stage. The surface of the sulfide-rich protrusion, where it penetrates into the bulk gas, (which would be closer to the CO_2-10%SO_2 composition or flushing argon), tends to be converted to oxide. As a consequence, these oxide grains grow in a columnar orientation normal to the surface of the protrusion core. This orientation indicates that the transport of cations through the sulfide-rich core is faster than through the oxide grains, and thus confirms Stage 3 of Figure 30: oxide nucleates easily and grows on the sulfide-rich core. Otherwise, the oxide would grow parallel rather than perpendicular to the sulfide-rich core as shown in Figure 33, and it would be impossible for many oxide grains to grow and to cover the sulfide-rich core.

The wrinkles formed on the scale surface and on the surface of the protrusions as shown in Figure 19 are probably a result of grain boundary diffusion of

iron which is enhanced by sulfide at the grain boundaries. Figure 20 reveals that the wrinkles grow along the scale grain boundaries.

Wrinkles are not found in either pure sulfidation or pure oxidation of iron, although the grain boundary exists in both cases. Therefore, it is believed that sulfur plays an important role in grain boundary diffusion. In a recent study (see Section 5.1), the existence of sulfide at the oxide grain boundary was demonstrated. The sulfide might enhance the grain boundary diffusion of cations, because the bonding of the sulfide is much weaker than that of the oxide, *i.e.*, the transport of iron ions along the sulfide network at grain boundary is much faster.

To confirm this, pure iron was sulfidized in H_2–10%H_2S for 1½ hours and then exposed to air for 4 minutes at 871°C. The sulfur below the oxide scale penetrated along the grain boundaries of the oxide scale and enhanced the outward diffusion of cations. Therefore, wrinkles should be observed on the surface of the oxide scale despite the fact that wrinkles were not observed in either pure sulfidation or pure oxidation. Figure 34 shows the growth of these wrinkles schematically illustrated in Figure 35.

These wrinkles (Figure 34) are finer than those observed on the scale formed in a CO_2–10%SO_2 atmosphere (Figure 20). This difference is due to a different sulfur content in the matrix. Nucleation of oxide on the scale surface depends on the supply of iron ions combining with oxidant. However, iron ions transport faster in the pure sulfide formed in H_2–10%H_2S than in the sulfide/oxide mixture formed in CO_2–10%SO_2. Thus, a finer oxide grain size is obtained on a pure sulfide scale.

Porous Structure

Apart from the irregularities on the scale surface, the second major

feature of the scale is the porous structure. Pores are present throughout the scale, but particularly in the inner layer. The formation of this porous structure is explained by the mechanism of unbalanced diffusion illustrated in Figure 36. The diffusivity of sulfur is greater than that of oxygen. The pores can be formed by the following mechanism:

In the scale, the sulfur concentration decreases from the scale/metal interface to the scale/gas interface as shown in Figure 36. With sulfur diffusing inward, presumably as an anion, formation of new sulfide at the scale/metal interface is not balanced by a continuous supply of sulfur from the outer layer, and this contributes to the porosity.

The inward transport of sulfur ions through sulfur-rich areas or grain boundaries results in either the formation of nuclei or the growth of the existing grains at the scale/metal interface. Separation of the scale from the metal using liquid nitrogen, revealed many nuclei at the scale/metal interface as in Figure 23. The nuclei are concentrated in the sulfur-rich areas. This proves that sulfur diffuses along the sulfur-rich channels. In addition, the layer of larger grains below the inner porous layer, as shown in Figure 22, indicates grain growth at the scale/metal interface. Both nucleation and grain growth are evidence of the inward diffusion of anions, which is the basis of the mechanism for the formation of the porous layer.

This mechanism was further confirmed by the following two experiments:

Experiment 1

Pure iron was exposed to CO_2–10%SO_2 for 3 hours, followed by another 3 hours exposure to air. In the first stage, sulfide-rich protrusions were formed on the scale surface. After being exposed to air for another 3 hours, these protrusions were covered by oxide. The sulfur in the protrusions diffused toward the scale/metal interface. However, because there was no continuous supply of

sulfur from the gas in the air exposure, the protrusions became porous as illustrated schematically in Figure 37 and as exhibited in Figure 38. Comparing Figure 38 with Figure 19, the wrinkles which exist in the first stage exposure disappear after second stage exposure. This is because the sulfur in the protrusion diffuses inward, and therefore enhanced grain boundary diffusion due to sulfur is no longer applicable.

Experiment 2

Pure iron was exposed to air for 1 hour, followed by 2 hours H_2–10%H_2S exposure, and exposed subsequently to air for a further 3 hours. After the final 3 hours air exposure, large pores were developed in the scale, as shown in Figure 39, due to the diffusion of sulfur through the oxide formed in the first 1 hour and the blockage of sulfur supply in the air exposure. The pores formed in this experiment were much larger than those formed in Experiment 1. This difference is related to the sulfur content. In the Experiment 1, the protrusions contained about 30% sulfide and 70% oxide ($^a/_o$). After sulfur diffused inward, the oxide still remained in the center of the protrusion (see Figure 38). However, in this experiment, the middle layer was pure sulfide. Inward sulfur diffusion and outward iron diffusion resulted in the formation of large pores. In addition, the inner part of the scale was porous, whereas the outer part of the sulfide scale (close to the oxide scale formed in the latter air exposure) was quite dense. This result excludes the possibility that the porous protrusion in Figure 38 is formed due to sulfur diffusing outward or oxidation to form sulfur dioxide.

Other factors, such as vacancy condensation at the scale/metal interface, stress generation as a result of phase transformations of *Fe*-oxide and wüstite-magnetite, or a dissociation mechanism, may also contribute to the formation of a porous layer. However, since the large-grained layer is quite dense, and

the porous layer is above this layer, but not at the scale/metal interface, unbalanced diffusion seems to be a predominent factor in forming the porous scale on Fe exposed to a CO_2–10%SO_2 atmosphere.

CHAPTER VII

THE EFFECTS OF ALLOYING ELEMENTS ON HIGH TEMPERATURE CORROSION

Stainless steels and heat-resistant alloys are designed to resist high temperature corrosion by forming a protective oxide scale on the alloy surface. The oxide serves as a barrier to the inward migration of oxidants as well as the outward migration of metal ions, thereby protecting the metal from accelerated attack. The protective scale is mainly formed by the selective oxidation of alloying elements in the alloy to form a thin and adherent oxide, such as Cr_2O_3 or Al_2O_3.

The basic idea of oxidation resistance of iron-chromium alloys has been briefly reviewed in Section 2-7. However, the introduction of sulfur-containing atmosphere can lead to rapid scaling and to internal precipitation of stable sulfides, even when a more stable, protective oxide covers the alloy. According to previous work[36], a high chromium steel is the only alloy so far found to be resistant to sulfidation when exposed to the environment within the bed of a fluidized-bed coal combustor. In spite of these evaluation tests, the basic mechanism of attack has not been completely understood.

The beneficial effect of aluminum on high temperature oxidation resistance of steels has been extensively studied by many workers and reviewed by Kubaschewski *et al.*[37] and Boggs[38]. However, the poor workability, weldability and fabricating difficulties of iron-aluminum alloys have limited the application of these alloys in industry. Nevertheless, the superior oxidation resistance of the iron-aluminum alloy has prompted the investigation of possible usage of this alloy in sulfur-containing atmospheres[39,40], perhaps as a coating or cladding over a substrate with better mechanical properties.

Iron-chromium-aluminum alloys have interesting oxidation behavior because aluminum competes with chromium to form a surface steady-state scale in certain composition ranges. It is well-known that it is easier to establish and maintain $\alpha - Al_2O_3$ scales on iron-chromium-aluminum alloys than on iron-aluminum alloys. The presence of chromium leads to the formation of an $\alpha - Al_2O_3$ layer which serves as a better barrier than $\gamma - Al_2O_3$ to suppress the growth of iron oxide. Chromium is important because it acts either as a getter[41] for oxygen during the initial stage of oxidation and prevents diffusion of oxygen atoms into the interior of the alloy followed by internal precipitation of Al_2O_3 which would preclude the formation of an outer Al_2O_3 scale or as a stabilizer of $\alpha - Al_2O_3$ rather than the less protective $\gamma - Al_2O_3$ [42]. Fundamentally, Cr_2O_3 and $\alpha - Al_2O_3$ nuclei develop extensively in the initial transient stage excluding or reducing the nucleation of iron oxides. That is to say, the nucleation of Al_2O_3 and Cr_2O_3 control and reduce the dissolution and diffusion rates of oxygen into the alloy, thus ensuring the eventual formation of a steady-state scale of either $\alpha - Al_2O_3$ or Cr_2O_3. If there is sufficient aluminum in the alloy, aluminum will have more opportunity to diffuse to the surface because of its higher activity and to provide a complete healing layer beneath the initially thin scale[41,43]. Despite the extensive studies on oxidation behavior of *Fe-Cr-Al* alloys, few studies have been done on the behavior of *Fe-Cr-Al* alloys in sulfur-containing atmospheres[40].

Based on the above considerations, there is a strong need to continue to undertake short term tests on chromium and aluminum steels in sulfur-containing atmospheres in order to examine the different parameters on corrosion behavior and to understand the basic corrosion mechanisms.

7.1. Results

On being exposed to a CO_2–10%SO_2 atmosphere, the alloys containing sufficient chromium or aluminum normally form stable, highly protective scales based on chromium oxide or aluminum oxide. The reaction kinetics are characterized by very slow reaction rates, similar to the situation in oxygen atmosphere, which slowly begin to accelerate - usually after several hours exposure, known as the *incubation time*. The corrosion morphologies of iron-chromium, iron-aluminum and iron-chromium-aluminum alloys are described separately as follows:

Iron-Chromium Alloy

Figure 40 shows a view of the external surface of an *Fe-18Cr* alloy exposed to CO_2–10%SO_2 for 48 hours at 871°C. Three kinds of morphologies can be identified. The center part of Figure 40 whose enlarged picture is shown in Figure 41 is pure chromium oxide. The scale in Figure 41 appears to consist of thin angular plates on a relatively smooth undulating inner oxide surface; in contrast, the oxide formed in pure oxidation (see Figure 42) consists of an assembly of approximately equiaxed grains bounded by plane faces, apparently low index crystallographic planes. Figure 43, the enlarged picture of the left part of Figure 40, shows the growth of oxides with uneven composition revealed by EDX analysis. The crystallographic grains aggregate together as clusters, but the vertical blades disappear. Figure 44, the enlarged picture of the right part of Figure 40, shows the alloy surface beneath the scale. An EDX analysis indicates that its composition is 0.6 $^a/_o$ *S*, 11.8 $^a/_o$ *Cr*, and 87.6 $^a/_o$ *Fe*. Two kinds of morphologies can be identified: the micro-rough area and the smooth area as described by Howes[44] in an observation of the metal/oxide interface for an *Fe-Cr* alloy. The former indicates the maintained contact between the scale and the alloy, whereas, the latter indicates the interconnected pores developed at the scale/alloy interface. Figure 45(a) shows the top view of an *Fe-25Cr*

specimen exposed to a CO_2–10%SO_2 atmosphere for 48 hours at 871°C. On the right lower corner, there exists a chromium oxide scale which is enlarged in Figure 45(b). Comparing with the Cr_2O_3 scale formed on *Fe-18Cr*, the scale formed on *Fe-25Cr* is less adherent and its vertical blades are smaller and fewer in number. Figure 46(a), the enlarged picture of the center part of Figure 45(a), shows the alloy surface where the scale spalled off. Some iron-rich nodules can be observed on the alloy surface. The EDX analyses of Point x & y are displayed in Figure 46(b) & (c). At the relatively flat area, chromium content is over 18 $a/_o$; whereas, the nodules contain only 2.6 $a/_o$ chromium. The nodules are observed even after the scale is removed manually. It is likely that these nodules growing beneath the scale by penetration of sulfur or oxygen degrade the adhesion between the scale and the alloy and lead to the extensive spallation of the scale. Figure 47(a) shows the top view of the scale formed on an *Fe-40Cr* specimen after the exposure to a CO_2–10%SO_2 atmosphere for 110 hours. The scale is pure chromium oxide as shown in the Figures 47(b) & (d). At the alloy surface where the scale spalled off, the sulfur content is a little higher but no iron-rich nodule is observed. An EDX analysis indicates its composition as 1.3 $w/_o$ S, 30.0 $w/_o$ Cr, and 68.7 $w/_o$ Fe. A comparison of the scales formed on *Fe-18Cr*, *Fe-25Cr* and *Fe-40Cr* concludes that the number and size of the vertical blades in the scale as well as the adhesion of the scale decrease with increasing chromium contents in the alloys.

Over a long exposure time, continuous spallation of Cr_2O_3 scale and formation of new scale with lower chromium contents finally destroy all the protective Cr_2O_3 scales. Figure 48, the top view of the scale formed on *Fe-18Cr* exposed to CO_2–10%SO_2 for 7 days, shows the growth of essentially pure iron oxide on the surface. A porous layer which is rich in chromium and sulfur exists near the scale/alloy interface as shown in Figure 49. An EDX analysis

shows that this porous layer contains approximately 20 $a/_0$ S which will be discussed later in this chapter.

Preoxidization experiments were carried out to see if this improved the resistance to SO_2 attack. Figure 50(a) shows the top view of an 18-hour-preoxidized *Fe-18Cr* specimen exposed to CO_2–10%SO_2 for 32 hours. Many nodules were observed on the scale. Figure 50(b) shows the top view of a nodule and Figures 50(c), (d) show the detailed morphology of the flat scale. A large number of thin fibers and blades were observed on both nodules and flat scales. The nodules as well as the scale are poorly adherent to the alloy matrix and thus easily spall off. An EDX analysis, as shown in Figure 51, indicates that the nodules are low in *Cr* but rich in *Fe*. Beneath the scale and the nodules, many particles were observed on the metal surface as shown in Figure 52. These particles at the scale/metal interface contain iron sulfide as shown in Figure 53. The particles, formed as a result of the inward diffusion of sulfur, may perhaps be responsible for the poor adhesion of scale to alloy matrix.

To investigate the growth mechanism of the nodules, an 18-hour-preoxidized *Fe-18Cr* specimen was exposed to a CO_2–10%SO_2 atmosphere for 6 hours. It is observed that the nodules initially grow as a ring then spread out as shown in Figure 54(a). These rings are believed to be associated with the grain boundaries of the underlying alloy matrix, *i.e.*, sulfides (or oxides) nucleate on and grow along the grain boundaries of the alloy substrate leading to the growth of the iron oxide-rich rings. An examination of the alloy grain size, as shown in Figure 54(b), indicates that the grain size is similar to the ring size, although a direct correspondence has not been shown. It is therefore believed that sulfur penetrates into the grain boundaries of the alloy, thereby enhancing the outward diffusion of iron ions along the grain boundaries resulting in the formation of iron oxide-rich rings.

Iron-Aluminum Alloy

After alloy specimens have been exposed to CO_2–10%SO_2, it is observed that the scale morphology of iron-aluminum alloys is different from that of iron-chromium alloys in two major characteristic ways. Firstly, the incubation time is generally longer for iron-aluminum alloys than for iron-chromium alloys. This is, of course, due to the better sulfur penetration resistance of Al_2O_3 than Cr_2O_3. However, for iron-aluminum alloys, the incubation time is more variable: it ranges from a few hours to a few days. Secondly, the scale is rather more adherent to the *Fe-Al* alloy matrix, but the attacked areas are much more localized: fewer nodules are nucleated and tend to grow deeper into the iron-aluminum alloy instead of spreading laterally. In contrast, the scale on iron-chromium alloys is poorly adherent to the alloy matrix. Usually, more nodules are produced and tend to interconnect forming a comparatively uniform scale. Figure 55 shows the polished cross-section of a typical nodule growing into an *Fe-10Al* specimen after being exposed to CO_2–10%SO_2 for 7 days. The outer layer of the nodule is iron oxide with a sulfide-rich layer at the original metal surface. Similar to the pitting behavior of low temperature corrosion, the effect of differential aeration cell is observed as shown in Figure 56 and schematically illustrated in Figure 57. The inner layer of the nodule is a mixture of iron oxide, aluminum oxide and spinel ($FeAl_2O_4$). At the tip of the nodular base, many Al_2S_3-rich intrusions are observed. Pegs are not observed at the flat nodule/alloy interface as shown in Figure 58(b). Figure 59 shows the images and corresponding *S* and *Al* maps of the tip of a nodular base. A layer of alumina is observed at the nodule/alloy interface. This alumina layer is developed probably by the selectively oxidized Al_2O_3 being continuously suppressed by the new scale forming above it. Beneath this interface, intrusions which are rich in aluminum and sulfur grow normal to the nodule/alloy

interface. The intrusions are blade-like in shape as revealed in a deep-etched sample shown in Figure 60.

Iron-Chromium-Aluminum Alloy

Iron-chromium-aluminum alloys exhibit excellent corrosion resistance to CO_2–10%SO_2 atmospheres. After an *Fe-18Cr-3Al* sample was exposed to CO_2–10%SO_2 for 700 hours at 871°C, neither thick scale nor localized attack was observed. However, similar to iron-chromium alloys, the scale formed on *Fe-18Cr-3Al* is lack of adhesion to the alloy, thus, it can spall off easily. Figures 61(a)-(d) are the SEM image and corresponding *Cr*, *Al* and *Fe* maps of the 700-hour-exposure *Fe-18Cr-3Al* sample. In the center part of Figure 61(a), the scale had spalled off, thus, the alloy matrix was exposed to the atmosphere. Sulfur was detected using SAM at the exposed alloy matrix as shown in Figure 62. However, it was not severely attacked, since it still contained enough *Cr* when the scale spalled off, a protective Cr_2O_3 scale could be reformed. Figure 63 is the top view of the scale which is mainly composed of Al_2O_3, also containing iron and slight chromium. An EDX analysis shows that the scale is composed of 62.37 $a/_o$ *Al*, 9.62 $a/_o$ *Cr*, and 28.81 $a/_o$ *Fe*.

7.2. Discussion

In general, neither Cr_2O_3 nor Al_2O_3 provides a good barrier to sulfur-induced attack. Basically, sulfur penetrates through the scale and concentrates at the scale/alloy interface. For iron-chromium alloys, the sulfur destroys the adhesion between the scale and the alloy and leads to the continuous spallation of Cr_2O_3 scale and finally to the exposure of chromium-depleted alloy to the CO_2–SO_2 atmosphere. The rehealed scale with less chromium and more iron can not provide a good barrier to outward diffusion of cation or to inward diffusion of anion. Consequently, an accelerated corrosion rate is observed. As

for iron-aluminum alloys, sulfur penetration is much slower, but even more worry is given to the enhanced localized attack. This leads to a fast corrosion rate at the area where protective scale fails first.

Four questions arise:

1) Why does sulfide form in the scale, contradicting the thermodynamic prediction?

2) How does sulfur penetrate through the scale?

3) What is the driving force for the sulfur penetration?

4) What is the role of sulfur in the cycling behavior?

For the process of high temperature oxidation or sulfidation of pure metals and alloys, the following stages of reaction can be observed:

1. dissociation and adsorption of gas molecules as anions on the metal surface;

2. nucleation and growth of oxide or sulfide;

3. formation of a thick continuous layer of scale.

Nucleation of metallic oxides has been studied since 1950[45]. Recently, studies in this field have focused more on the adsorption stage. Techniques, such as LEED, ESCA and SAM, are very useful in this field, especially, to understand the growth mechanism and the structure of adsorbed layers in relation to the atomic arrangement of the substrate surface.

As described in 1956 by Moreau and Bénard[46] for *Fe-18Cr* in a H_2-H_2O mixture at high temperature, if the partial pressure of oxygen is slightly higher than the dissociation pressure of Cr_2O_3, this oxide is the only one nucleated. This is the classical phenomenon of selective oxidation of the element having a higher affinity for oxygen in the alloy. If the partial pressure of oxygen is lower than the dissociation pressure of Cr_2O_3, no oxide can be formed. However, a

new phenomenon appears: the planar metal surface appears to become unstable and develops facets with new orientations (facetting). It was assumed that adsorbed oxygen was responsible for the facetting. This explanation is now generally accepted to explain facetting of pure metals in the presence of traces of a reactive gas.

Recently, Oudar[47] observed that chromium is selectively combined with sulfur and oxygen in adsorbed layers formed at high temperatures on iron-chromium alloys using LEED and SAM calibrated with S^{35}, and concluded that the heat of adsorption determined by the *Van't'Hoff* equation is almost identical to the enthalpy of formation of *CrS*. From this, it is concluded that the metal-sulfur bonds are very similar in the 2D surface compound and in the 3D compound *CrS*.

When iron-based alloys are exposed to CO_2–10%SO_2 atmospheres, the thermodynamic calculations in Chapter III predict that sulfide is not stable on the metal or scale surface. But the prediction does not exclude the possibility of sulfur being adsorbed on the surface temporarily and returning to the atmosphere thereafter. The temporarily adsorbed sulfur, however, may have a profound effect on the nucleation of oxide. It is possible that the different scale morphologies between CO_2–10%SO_2 exposure (Figure 41) and air exposure (Figure 42) are associated with the adsorption of sulfur on the alloy surface, that changes the normal oxide nucleation process. However, other possible factors may also play a role in the scale growth process leading to the distinctive morphology, such as different oxygen potential in gas mixtures, carbon or nitrogen as an impurity. The detailed mechanism, therefore, requires further exploration.

In the growth of oxide (or sulfide) scale on metals, the reactants may be transported across the growing layer by lattice diffusion[21]. Examples of both

cation and anion diffusion have been reported; the diffusion process may involve the movement of vacancies or of interstitials. Because the anion is relatively large in oxides or sulfides, there are no well-documented examples of anion interstitial transport, although it has been suggested that the anionic species may be present interstitially as an uncharged atom, or even perhaps, as a positively charged ion. Semiconducting oxides (that is, oxides in which ionic transport is slower than electronic transport) are p-type if the major mobile species is a cation vacancy; and n-type if the major mobile species is a cation interstitial as an anion vacancy. In addition to the majority species, there may of course be minority defect species: these play an important role in processes such as diffusion creep, but have not been shown to be significant in oxidation.

The adsorbed gas molecules and their ionization result in the formation of an electric field across the scale. This field normally accelerates the ion diffusion and thus leads to a fast surface transport. Following the terminology of semiconductor physics, this region close to the surface, where electric space charge is present, is designated as a space-charge boundary layer or a *space-charge* layer.

If one considers the metal-oxide system as an electrochemical cell analogous to an aqueous corrosion cell, the overall chemical reaction

$$2\,Cr + \frac{3}{2}O_2 \rightarrow Cr_2O_3;\ \Delta G^o \approx -196\,kcal/mole\ \ (at\ 871^oC)$$

occurs by separate anodic and cathodic reactions at the two surfaces of the oxide layer. On this basis, it can be calculated that an electrical potential difference of approximately $E = -\Delta G^o/6F = 1.4$ *volts* should be developed between the cathodic and anodic regions. This potential has qualitatively different effects depending on the thickness of the oxide layer, for convenience, three classes can be differentiated: very thin (< 50Å), thin (50 ~ 1000Å), and thick (> 1000Å). In very thin films, the potential creates such high electric

fields ($1.4 \times 10^9 volts/m$ in a 10Å film) that quantum-mechanical tunnelling effects can aid in the growth of these films even at low temperatures. If this is the transport mechanism, the film may virtually stop growing at a thickness corresponding to the minimum electric field required to initiate the tunnelling. At slightly higher temperatures the further growth of very thin oxide films is strongly influenced by a concentrative overpotential of the electronic defects. A typical rate law for such thin films is the logarithmic relation:

$$x = K_1 \log(K_2 t + K_3)$$

For the second class, a cubic rate law ($x^3 = K_c t$) is observed. These scale thicknesses can produce selective adsorption of light, resulting in the characteristic tarnishing colors. This rate law can be derived by taking account of the changing field across the scale as it thickens and the effect of the field on defect diffusion.

The behavior of thick oxide layers depends on the characteristics of the oxide composing the film. Two types of transport must occur through an oxide layer if the growth is to continue: (1) electrons and/or holes must flow as an electronic current between the cathodic and anodic regions to prevent excessive increase of electrical potential, and (2) cations and/or anions must diffuse as the flux to permit cooperative building of the oxide lattice. The migration of the ionic species also transports charges. At the steady state the net flux of positively and negatively charged species must be equal in terms of chemical equivalents. In a semiconducting oxide, the more quickly moving electrons establish a field which has the effect of slowing down the transport of the electronic defects and accelerating the transport of the the ionic defects until the fluxes become equal. When the transport properties do not vary with scale thickness or with time and the transport process (other than an interface process) is rate-limiting, parabolic rate kinetics are observed. Parabolic growth

does not require that the ionic flux be the slower process and determine the rate of oxidation. For example, in the growth of halides on metals the corrosion product is an ionic conductor (ions move faster than electrons) but the growth is parabolic - this case is also treated by Wagner[48].

The effect of the electric field diminishes as the scale thickness increases. However, space-charge layers still exist at both the scale/gas and the scale/alloy interfaces, because of the large electron affinity of the chemisorbed gas and the different work functions between alloy and scale. While the action of the chemisorbed gas on the scale has been investigated very thoroughly[21], the space-charge-layer effects at the scale/metal phase boundary during oxidation have not yet been successfully studied. The surface charge at the scale/alloy interface attracts the nearby negatively charged defects and repels the nearby positively charged defects. Consequently, anions, irrespective of whether they are oxygen or sulfur, move toward the alloy, cations, no matter whether they are iron, chromium or aluminum, move away from the scale/alloy interface. Similarly, at the scale/gas interface, the surface charge of chemisorbed gas keeps attracting the positively charged defects and repelling the negatively charged defects near the scale/gas boundary.

The concentration of cation vacancies decreases from the scale/gas interface to the scale/alloy interface. Thus, cations, no matter which kind, diffuse from the scale/alloy boundary toward the scale/gas boundary. Generally, iron cations transport faster than chromium or aluminum ions, thus, the scale surface is rich in iron. Moreover, the chemisorbed oxygen is all over the scale surface, thus, iron cations can spread laterally from the nodules where sulfide destroys the protective Al_2O_3 scale, and cover the unattacked scale where Al_2O_3 scale limits the outward diffusion of iron under it as schematically illustrated in Figure 57 and shown in Figure 56. This is the same effect as differential aera-

tion cell on pitting in low temperature corrosion and a strong confirmation of faster outward diffusion of iron ion than aluminum ion, since aluminum was not observed in the spreading scale.

As mentioned earlier, sulfur may be adsorbed on the scale or metal surface temporarily, and may be present as an adsorbed molecule, uncharged atom, or charged ion, presumably negatively charged. Such a sulfur ion on the scale/gas interface would be repelled by the surface charge, and would tend to diffuse into the scale, instead of returning to the atmosphere as a gas molecule because that would involve the thermodynamically unfavored process of the release of electrons. Furthermore, the continuous formation of new scale by the outward diffusion of cations combining with adsorbed anions at the scale/gas interface will eventually immerse most of the adsorbed sulfur in the scale. This is confirmed by the observation that sulfur concentrates in the outer iron-rich, but essentially aluminum-free, layer of the scale as shown in Figure 55. The outward diffusion of iron cations combining with adsorbed anions on the surface is responsible for the formation of this layer. In contrast, the inner layer of this scale is believed to grow mainly by inward diffusion of anions, therefore, it contains aluminum.

Inside the scale, the anion vacancies decrease from the scale/metal interface to the scale/gas interface. Both oxygen and sulfur anions can diffuse toward the scale/alloy interface via these vacancies. However, presumably sulfur transports faster than oxygen due to its weaker bonding with the cations, thus, sulfur diffuses to the alloy side much easier than oxygen. The continuous diffusion of anions toward the scale/alloy interface and the formation of the new scale at the scale/alloy interface result in the increase of sulfur concentration at the scale/alloy interface. This accounts for the observations that sulfur concentrates at the scale/alloy interface as shown in Figure 59 and Fig-

ure 49. The sulfur diffusion from the scale/gas interface to the scale/metal interface against its concentration gradient in the scale can be explained by the ternary diffusion theory[49,50]. This means that sulfur chemical potential is raised under the influence of the oxygen in the scale. The diffusion in ternary system is complicated and has not been extensively studied, nor is it well understood. Further work is needed to explore the details.

In many oxidizing systems, transport across the oxide scale is dominated by one ionic species (*i.e.*, either cations or anions), and the other species may be considered immobile to a reasonable approximation. In the case of cation diffusion, new oxide forms at the oxide/gas interface and consequently can adjust itself into whatever volume it requires without generating appreciable stress. Anion diffusion, on the other hand, results in the formation of new oxide at a confined interface (oxide/metal or oxide/oxide). If the oxide-to-metal volume ratio is different from unity, the potential for stress generation exists, although the magnitude and distribution of the stresses are very much dependent on the morphology of the reaction interface.

In the somewhat unusual situation of simultaneous diffusion of both cations and anions, it is possible to generate very large stresses. For example, Rhines and Connell[51,52] provided evidence that oxygen diffusing inward along grain boundaries meets nickel diffusing outward through the *NiO* grains during the high temperature oxidation of nickel, thereby new oxides in the grain boundaries are formed. The resulting lateral stresses are large enough to induce creep in the unoxidized portions of the metal.

In sulfur-containing atmospheres, the significant penetration of sulfur through the scale resulting in the formation of sulfide at the scale/metal interface and the large sulfide-to-metal volume ratio make this spallation all the more serious. Since sulfide-to-metal volume ratio is greater than oxide-to-

metal volume ratio (see Appendix D), the volume increase generates large stress, thereby destroying the adhesion at the scale/alloy interface. Moreover, the sulfur itself may also change the adhesion between the scale and the metal. Therefore, in this investigation, all the scales with sulfur spall off easily.

For example, Figure 64, the underside of the sulfide scale formed on an iron specimen exposed to H_2–10%H_2S for 1½ hours, shows many nuclei at the scale/metal interface. It is believed that the expansion of volume at the scale/metal interface produced by these nuclei makes the spallation of the iron sulfide scale much easier. Furthermore, these nuclei appear to be located in the grain, rather than at the grain boundaries, indicating the inward diffusion of sulfur through the sulfide scale is probably via lattice diffusion or short-circuit paths down dislocation cores which are within the grains, but certainly not via grain boundary paths.

When the protective scale spalls off because of either the sulfur penetration forming nodules beneath it or the stress generation during normal oxidation process, the atmosphere can react with the alloy substrate immediately at elevated temperature. If the alloy is sufficiently rich in *Cr*, such as *Fe-40Cr*, new protective oxide can be generated. However, in the case of alloys with lower chromium contents, such as *Fe-18Cr*, healing is unlikely. Consequently, the non-protective iron-containing nodules will continue to grow until the entire specimen is consumed as shown in Figure 48.

It is found that the scale spallation increases as the chromium content in the alloy increases. This phenomenon is related to the irregularity of the scale/alloy interface that improves the adhesion of the scale to the alloy. As shown in Figure 65, the scale/alloy interface of *Fe-18Cr* alloy is more irregular than that of *Fe-25Cr* due to its more severe localized attack. Therefore, although the *Fe-18Cr* alloy corrodes faster, the scale has a better adhesion to

the alloy. This probably will improve its erosion resistance to moving particles.

Sulfide at the scale/metal interface not only causes the spallation of protective scale, but also prevents the healing of protective scale at the scale/alloy interface. Normally, in the case of oxidation, the accelerated attack due to spallation of protective scale can be retarded by the healing of a new Cr_2O_3 or Al_2O_3 layer at the nodule/alloy interface[53]. However, when sulfide is present as a layer at the scale/alloy interface, it will always remain at the interface. This phenomenon known as *cycling effect* was proposed by Spengler and Viswanathan[54] and confirmed by El Dahshan, Whittle and Stringer[55,56]. They suggested that a small ingress of sulfur at the scale/metal interface removes chromium from solution as sulfides which are then oxidized forming Cr_2O_3 or spinels, thus the sulfur is released to attack the metal phase further. Hence any small amount of sulfur at the scale/metal interface will cause continuous damage.

The observations[55,56] that all of the sulfur that occurs at the scale/metal interface is retained and does not escape to the atmosphere, even when this is pure oxidation in a sulfur-free atmosphere, is an indication that the sulfur is held at low activity as chromium sulfides and that the cycling or regenerating behavior referred to the above occurs by solid state reaction and not by gas phase reaction.

To confirm this mechanism in iron-aluminum alloy systems, an *Fe-10Al* specimen was exposed to a H_2–10%H_2S atmosphere for 1 hour, and subsequently exposed to air for another 19 hours. Many nodules were observed after this short exposure as shown in Figure 66. Normally, nodules would not grow within the first few hours if the alloy was exposed to a CO_2–10%SO_2 atmosphere. However, presulfidation destroys the ability of the alloy to form a protective Al_2O_3 scale and leads to a rapid growth of nodules. Figure 67 shows the pol-

ished cross-section of a nodule and the corresponding *Al*, *S* and *Fe* X-ray maps. Two sulfide layers are observed in the nodules. The first layer exists between the dense and porous layers of the nodule as shown in Figure 68. This sulfide layer forming in the first hour H_2–10%H_2S exposure works as an inert marker in the growing scale. The sulfur at the dense/porous layer interface confirms the unbalanced diffusion for the formation of porous layer proposed in Chapter VI: the inner porous layer is formed by inward diffusion of anions. The second sulfide layer developing at the nodule/alloy interface is in the form of Al_2S_3 stringers as shown in Figure 69. It is clear that there are a few sulfides left between the two sulfide layers indicating the inward penetration of some sulfur. This sulfide layer and the accelerated growth of nodules confirm the cycling effect of sulfur which can continuously attack the alloy matrix and destroy the protective nature of alloys. The separation of sulfide as two layers indicates that although sulfur diffuses to and concentrates at the scale/nodule interface, there is only a limited amount, uniformly distributed sulfur existing at the scale/nodule interface. This probably is an indication of the effect of space-charge layer which provides electric field only over a short range. Moreover, there is no Al_2O_3 layer observed at the nodule/alloy interface that is different from the case of *Fe-10Al* exposed to CO_2–10%SO_2 for 7 days as shown in Figure 59. This confirms the previously proposed idea: the Al_2O_3 layer in Figure 59 is developed by the selectively oxidized Al_2O_3 being continuously driven inwards by new scale formed above it, not by healing, otherwise a similar layer would be observed in this presulfidized *Fe-10Al* specimen.

In summary, two effects are produced by the sulfide at the scale/metal interface:

(1) the generation of stresses at the scale/metal interface leading to the spallation or poor adhension of the scale;

(2) the destruction of the protective nature of the scale.

The latter effect may be caused by two possible mechanisms:

(a) The existence of sulfur in the scale provides a network of channels for base metal to transport rapidly through the protective Al_2O_3 or Cr_2O_3 scales, *i.e.*, sulfur enhances the outward diffusion of cations. This mechanism is supported by the observation that an Al_2O_3 layer at the nodule/alloy interface fails to stop nodule growth.

(b) The catalytic effect of sulfur at the scale/alloy interface produces more anion vacancies. Sulfur diffuses inward to the alloy matrix easily, thus providing more anion vacancies at the scale/alloy interface, *i.e.*, it enhances the anion inward diffusion. This effect is supported by the observation that sulfur always exists at the scale/alloy interface, even when the specimen is exposed to sulfur-free atmospheres after a short exposure to sulfur-containing atmospheres. The attack does not stop even when a layer of Al_2O_3 forms behind the sulfide.

It is suggested in Chapter VI that pores can be formed due to the unbalanced diffusion of oxygen and sulfur. Alternatively, it is also possible to form pores as a result of unbalanced diffusion of cations and anions. This is especially true for alloys whose irregular scale/metal interface can be enhanced by alloying elements, particularly active elements, such as *Hf* or *Y*. It was shown in Chapter V and in other papers[33] that sulfur can penetrate into the grain boundaries of metals and alloys. The depletion of chromium near the grain boundaries by selective sulfidation of chromium at the grain boundaries of the *Fe-18Cr* alloy leads to the preferential corrosion at the grain boundaries - a sulfide network. This phenomenon is similar to the intergranular corrosion of sensitized 304 stainless steel at low temperatures. Meanwhile, near the surface

of the alloy, the chromium-depleted alloy grains are surrounded by chromium-rich sulfide networks. Near the scale/alloy interface, the iron within the alloy grains can diffuse rapidly along the sulfide network toward the scale/gas interface, and this can lead to the development of pores, resembling Kirkendall voids, within the grains. The continuous diffusion of sulfur into the alloy matrix results in the formation of a porous layer in the sulfide scale as illustrated in Figure 70.

Figure 71 shows the polished cross-section of an *Fe-18Cr* specimen exposed to H_2–10%H_2S for 2 hours at 871°C. The observation of some remaining alloy grains at the edge of pores in the sulfide scale confirms the mechanism proposed above. It is also observed that pore size gradually increases with distance from the scale/alloy interface. This pore size distribution indicates that the scale/alloy interface is moving toward the alloy side, therefore, the pores developed at the scale/alloy interface coalesce as the scale/alloy interface shifts toward the alloy side. A further confirmation of sulfur penetration into grain boundaries leading to intergranular corrosion is shown in Figure 54 which indicates the growth of iron oxide rings above the metal grain boundaries.

As a comparison, a pure iron sample was exposed to a H_2–10%H_2S atmosphere at the same condition. It was observed that the scale formed on *Fe-18Cr* (Figures 71 and 71) is more porous than that on pure iron (Figures 73 and 63). This is because there is no selective sulfidation possible for pure iron, and thus pores can not be formed for lack of intergranular corrosion.

Considering an *Fe-18Cr* specimen exposed to CO_2–10%SO_2 for 7 days, the combination of unbalanced diffusions of oxygen and sulfur and of cations and anions prompts the formation of a highly porous layer (see Figure 49). Nevertheless, the outer layer of the scale formed by the outward diffusion of cations remains dense.

The *Fe-18Cr-3Al* alloy exhibits excellent corrosion resistance in a 700-hour CO_2–10%SO_2 test. Two major factors contribute to its excellent behavior: Firstly, it forms an Al_2O_3-rich scale which is more protective than a Cr_2O_3 scale to sulfur penetration. Secondly, it contains sufficient chromium beneath the scale. Therefore, when scale spalls off, a Cr_2O_3 scale, which prevents the accelerated nodules formation and saves time for the formation of a healing Al_2O_3, can be formed immediately.

The latter point was further confirmed by the following experiment: an *Fe-10Al* and an *Fe-18Cr-3Al* specimen were preoxidized for 24 hours at 871°C, then carefully polished until the scales were just removed, subsequently exposed both specimens to CO_2–10%SO_2 atmospheres for 1 hour. It was observed that the *Fe-10Al* specimen suffered severe attack, whereas, the *Fe-18Cr-3Al* specimen did not. This experiment indicates that if the scale spalls off, *Fe-18Cr-3Al* with enough chromium in the aluminum-depleted zone can reheal rapidly, but *Fe-10Al* without any other alloying element in the aluminum-depleted zone cannot reheal. However, it is predicted that despite the fact that the *Fe-18Cr-3Al* alloy has excellent corrosion resistance, over a long time, probably a few thousand hours, a layer of sulfide will accumulate at the scale/metal interface and the alloy will suffer accelerated attack. This is based on the following experiment: an *Fe-18Cr-3Al* specimen was presulfidized for 1 hour, and subsequently oxidized in air for 19 hours. As shown in Figure 74, the specimen was severely corroded.

As a conclusion, work to date suggests that scales formed on iron-chromium-aluminum alloys by controlled preoxidation in sulfur-free atmospheres provide the best performance in simulated coal combustion atmospheres. In addition, controlling the combustion atmosphere in low P_{S_2} and high P_{O_2} will minimize the sulfidation attack and thus further elongate the alloy

service life. Advanced work is needed to optimize the composition and surface condition of alloys to develop a compact, dense, adherent scale in service environments.

CHAPTER VIII

CONCLUSIONS

1. The reaction rate for pure iron exposed to CO_2–10%SO_2 is between the rates of oxidation and of sulfidation.

2. The scale formed on pure iron exposed to CO_2–10%SO_2 is composed of three layers: an outer magnetite layer with protrusions on the surface and sulfide-rich streaks beneath the protrusions, an inner wüstite/sulfide duplex layer, and a layer of large grains at the scale/metal interface. The grains in the scale are in the form of a lamellar structure with alternating layers of sulfide and oxide; different grains contain different amounts of sulfur.

3. The existence of sulfide in the scale on pure iron is due to the depletion of oxygen in the neighborhood of the scale/gas interface. This phenomenon shifts the thermodynamic equilibrium in the gas from one in which oxide is stable to one in which sulfide is stable.

4. The fast corrosion rate of iron exposed to oxygen-rich but sulfur-containing atmospheres and the formation of protrusions at the scale surface are due to the rapid transport of iron ions through sulfide-rich channels in the oxide.

5. Wrinkles which are observed on the scale surface, including the surfaces of the protrusions which develop on the iron specimens, are formed by sulfur-enhanced grain boundary diffusion.

6. The unbalanced diffusion between sulfur and oxygen and between cations and anions leads to the formation of pores in the scale.

7. Preferential sulfur diffusion down grain boundaries of the scale formed on pure iron has been identified using Scanning Auger Microscopy. A very

high diffusion coefficient is implied.

8. Sulfur can penetrate rapidly through the chromium oxide scale grown on pure chromium. The transport of the sulfur through the scale appears to be via short-circuit paths. The sulfur then migrates rapidly into the metal by grain boundary diffusion; from the boundaries it diffuses into the metal grains at a very much lower rate.

9. A model in which the space-charge layers in the oxide enhance the adsorption and diffusion of sulfur is proposed to account for the existence of sulfide beneath the Cr_2O_3 and Al_2O_3 scales.

10. The sulfide at the scale/metal interface can generate stress at the interface resulting in the poor adhesion or spallation of the scale, thus destroying its protective nature.

11. For alloys with high chromium contents, the spallation of the scale is the main cause of failure, whereas, for alloys with high aluminum contents, the scale suffers sulfur-induced localized attack.

12. Of the *Fe-Cr*, *Fe-Al* and *Fe-Cr-Al* alloys studied, the best corrosion resistance in the simulated coal combustion atmosphere was exhibited by the *Fe-18Cr-3Al* alloy. This alloy has enough chromium beneath the scale for healing when the protective Al_2O_3-rich scale fails due to spallation or sulfur penetration.

ACKNOWLEDGEMENTS

I am very grateful to

Prof. D. Whittle* and Prof. J. Stringer for their support and guidance during this research;

Prof. L. Brewer, Prof. A. Evans, and Prof. A. Searcy and Dr. S. Smith for their helpful comments and assistance;

Mr. G. Baum, Mr. K. Gaugler and Ms. S. Ozturkmen for their help.

This work was supported by the Director, Office of Energy Research, Office of Basic Energy Science, Materials Sciences Division of the U.S. Department of Energy under contract Number DE-AC03-76SF00098.

* deceased

APPENDICES

Appendix A

Thermodynamic Stability Diagrams

Gibbs free energy data can be used to calculate which reaction products can exist in stable equilibrium with the gas phase at the scale/gas interface. For example, in the reaction for the oxidation of iron, the equilibrium constant (K) can be calculated from the standard Gibbs free energy (ΔG^o) for any temperature of interest as follows:

$$Fe + \tfrac{1}{2} O_2 \leftrightarrow FeO \qquad \text{(A-1)}$$
$$\Delta G^o = -RT \ln K$$

where ΔG^o = standard free energy of formation at temperature "T"

T = Temperature, ^oK

R = Gas Constant [1.987 cal/(mole)(^oK)]

K = Equilibrium Constant.

The oxygen partial pressure for the reaction at equilibrium is calculated from the equilibrium constant (K) as follows:

$$K = \frac{a_{FeO}}{a_{Fe} \cdot P_{O_2}^{1/2}} \qquad \text{(A-2)}$$

For unit activity of Fe and FeO, $K = \dfrac{1}{P_{O_2}^{1/2}}$

where a_{FeO} = Activity of the oxide, normally unity

a_{Fe} = Activity of the metal, normally unity

P_{O_2} = Equilibrium oxygen pressure, atmospheres.

Thus, $P_{O_2} = e^{\frac{2\Delta G}{RT}} \approx 10^{\frac{2\Delta G}{2.3RT}}$.

Iron oxide can exist as a stable phase on the surface only when P_{O_2} in the gas phases exceeds the calculated equilibrium value from Equation A-2. A similar calculation can be made for the sulfidation of iron and for the oxidation of iron sulfide to establish the equilibrium pressure of sulfur and oxygen at which the sulfide will be a stable phase. The pressures can be plotted in a diagram as shown in Figure 11 to map out the fields of phase stability where iron, iron oxide, and iron sulfide can exist in equilibrium with the gas phase. Referring to the boundaries for iron, the oxide will be stable at all oxygen pressures to the right of the vertical and sloping lines. The sulfide will be stable at all sulfur pressures above the horizontal and sloping lines. Unreacted metal will be stable at all sulfur pressures below the horizontal and oxygen pressures to the left of the vertical lines. Similar boundaries can be derived to map out phase stability fields for other elements in the alloy as shown in Figure 1.

Appendix B

Log Partial Pressures of Gas Species After Equilibria in CO_2-10%SO_2 & Air-1%SO_2 at 871°C.

Gas	Log Partial Pressure	
	CO_2–10%SO_2	Air -1%SO_2
CO	-4.0	--
CO_2	-0.0	--
SO_2	-1.0	-2.0
O_2	-8.7	-0.1
S_2	-10.1	-28.9
COS	-8.8	--
SO_3	-5.7	-2.2
CS	-20.7	--
CS_2	-18.5	--
SO	-6.1	-11.6

Appendix C

Specimen Compositions

Alloy Nominal Composition	Actual Composition (in w/o)		
	Fe	Cr	Al
Fe	99.91	0.00	0.00
Cr	0.00	99.9	0.00
Fe-10Al	Bal.	0.00	9.29
Fe-18Cr	Bal.	17.85	0.00
Fe-25Cr	Bal.	25.02	0.00
Fe-40Cr	Bal.	39.87	0.00
Fe-18Cr-3Al	Bal.	17.56	2.56

Appendix D

Volume Change of Metals to Oxides[57] or Sulfides[58]

Oxide	ΔV	Sulfide	ΔV
FeO	1.8		
Fe_3O_4	2.2	FeS	2.7
Fe_2O_3	2.1		
Cr_2O_3	2.0	Cr_2S_3	3.9
Al_2O_3	1.3	Al_2S_3	3.6

REFERENCES

1. F. S. Pettit, J. A. Goebel and G. W. Goward, Corr. Sci., 9, *903* (1969)
2. A. Rahmel, Corr. Sci., 13, *125* (1973)
3. N. Birks, Proceedings of the Symposium on Properties of High Temperature Alloys, The Electrochem. Soc., *215* (1976)
4. N. Birks and H. Rickert, J. Inst. Met., 91, *308* (1963)
5. S. Mrowec, Corr. Sci., 7, *563* (1967)
6. A. Atkinson, R. I. Taylor and P. D. Goode, Oxid. Met., 13, *519* (1979)
7. M. G. Fontana and N. D. Greene, Corrosion Engineering, McGraw-Hill Book Co., N.Y. (1967)
8. J. Stringer, Proceedings of the Symposium on Properties of High Temperature Alloys, The Electrochem. Soc., *513* (1976)
9. P. L. Hemmings and R. A. Perkins, EPRI FP-539 (Dec. 1977)
10. T. Flatley and N. Birks, J. Iron Steel Inst., 209, *523* (1971)
11. R. P. Salisbury and N. Birks, J. Iron Steel Inst., 209, *534* (1971)
12. A. U. Seybolt, Trans. AIME, 242, *752* (1968)
13. G. Romeo and H. S. Spacil, High Temperature Gas-Metal Reactions in Mixed Environments, ed. by Jansson and Foroulis, Met. Soc., AIME, Boston, MA, *299* (1972)
14. J. B. Wagner, Defects and Transport in Oxides, ed. by M. S. Seltzer and R. I. Jaffee, Plenum, N.Y., *283* (1974)
15. D. R. Holmes and J. Stringer, Limitations on the Use of Alloys in Coal Gasifiers for Power Generation, in Materials to Supply the Energy Demand, ed. by E. B. Hawbolt and A. Mitchell, ASM, Ohio, *165-204* (1981)

16. R. H. Chang, W. Steward and J. B. Wagner, Jr., Proc. of 7th International Symp. on Reactivity of Solids, Bristol, *231* (July 1972)

17. D. R. Chang, R. Nemoto and J. B. Wagner, Jr., Metall. Trans., 7A, *803* (1976)

18. A. Rahmel, Werkst. Korros., 16, *837* (1956)

19. D. Bruce and P. Hancock, J. Iron Steel Inst., 208, *1021* (1970)

20. M. C. Pope and N. Birks, Oxid. Met., 12, *173* (1978)

21. K. Hauffe, Oxidation of Metals, Phenum Press, N. Y. (1965)

22. I. G. Crouch and J. C. Scully, Oxid. Met., 15, *101* (1981)

23. R. A. Rapp, Corrosion, 21, *382* (1965)

24. N. D. Tomashov, Theory of Corrosion and Protection of Metals, The Macmillan Co., N. Y. (1966)

25. G. C. Wood and D. P. Whittle, Corr. Sci., 7, *763* (1967)

26. P. Auger, J. Phys. Radium, 6, *205* (1925)

27. J. J. Lander, Phys. Rev., 91, *1382* (1953)

28. L. A. Harris, J. Appl. Phys., 39, *1419* (1968)

29. R. E. Weber and W. T. Peria, J. Appl. Phys., 38, *4355* (1967)

30. P. W. Palmberg, G. K. Bohn and J. C. Tracy, Appl. Phys. Lett., 15, *254* (1969)

31. N. C. MacDonald, Electron Microscopy: Physical Aspects, ed. by D. Beaman and B. Siegel, Wiley (1974)

32. G. J. W. Korr and E. T. Turkdogan, Met. Trans., 2, *1571* (1971)

33. R. A. Perkins, EPRI FP-1280 (Dec. 1979)

34. M. C. Pope, J. H. Woodhead and N. Birks, Oxid. Met., 13, *3* (1979)

35. F. C. Yang and D. P. Whittle, Corr. Sci., 23, *285* (1983)

36. National Coal Board, U.K., EPRI CS-1853 (May 1981)

37. O. Kubaschewski and B. E. Hopkins, Oxidation of Metals and Alloys, 2nd ed., Butterworths, London (1967)

38. W. E. Boggs, Proceedings of the High Temperature Gas Metal Reactions in Mixed Environments Symposium, Corr. Sci., 5, *751* (1965)

39. K. N. Strafford, Metall. Rev., *138* (1969)

40. S. Mrowec and M. Wedrychowska, Oxid. Met., 13, *481* (1979)

41. C. Wagner, Corr. Sci., 5, *751* (1965)

42. W. C. Hagel, Corrosion, 21, *316* (1965)

43. G. C. Wood and M. G. Hobby, Proc. 3rd Int. Congress on Corrosion (1966)

44. V. R. Howes, Corr. Sci., 8, *221* (1968)

45. J. Bénard, L'oxydation des métaux, Gauthier Villars, Paris (1962)

46. J. Moreau and J. Bénard, J. Chim. Phys., 53, *787* (1956)

47. J. Oudar, Proceedings of the Symposium on Properties of High Temperature Alloys, The Electrochem. Soc., *61* (1976)

48. C. Wagner, Diffusion and High Temperature Oxidation of Metals, ASM, Cleveland, *153* (1951)

49. L. Darken, Trans. AIME, 180, *430* (1949)

50. D. P. Whittle, D. J. Young and W. W. Smeltzer, J. Electrochem. Soc., 123, *1073* (1976)

51. F. N. Rhines and R. G. Connell, Jr., Proceedings of the Symposium on Properties of High Temperature Alloys, The Electrochem. Soc., *154* (1976)

52. F. N. Rhines and R. G. Connell, Jr., Stress Effects and Oxidation of Metals, ed. by J. V. Cathcart, AIME, N. Y., *94* (1975)

53. M. Lambertin, A. Steklosa and W. W. Smeltzer, Oxid. Met., 15, *355* (1981)

54. C. J. Spengler and R. Viswanathan, Met. Trans., 3, *161* (1972)

55. M. E. El-Dahshan, J. Stringer and D. P. Whittle, Oxid. Met., 8, *211* (1974)

56. M. E. El-Dahshan, D. P. Whittle and J. Stringer, Oxid. Met., 8, *179* (1974)

57. G. V. Samsonov, The Oxide Handbook, Plenum Data Co. (1982)

58. M. B. Pilling and R. E. Bedworth, J. Inst. Met., 29, *529* (1923)

59. D. Peckner and I. M. Bernstein, Handbook of Stainless Steel, McGraw-Hill Book Co., . Y. (1977)

FIGURE CAPTIONS

Figure 1 Combined *Ellingham-Pourbaix-type* diagram for the *Fe-S-O*, *Cr-S-O*, *Al-S-O* systems at 871°C.

Figure 2 Shapes of oxidation curves.

Figure 3 Influence of SO_2 on the linear rate constant of the oxidation of iron in N_2-O_2 mixtures with 0.15 and 1.0% O_2 at 900°C.
(linear flow rate of the gas: 5.8*cm / sec*)

Figure 4 Influence of SO_2 on the parabolic rate constant the oxidation of iron in oxygen at 900°C.

Figure 5 Influence of CO_2 on the linear rate constant of the sulfidation of iron in $CO-CO_2-COS$ mixture with 0.12% COS at 900°C.
(linear flow rate of the gas: 5.8*cm / sec*)

Figure 6 Summary of Rahmel's experimental results. Influence of the second oxidant on the oxidation or sulfidation of iron in dependence of the rate-determining steps of the reaction.

Figure 7 Schematic representation of modes of oxidation of alloy AB of variable composition.

Figure 8 The *Fe-Cr* diagram[59].

Figure 9 Shift of gamma loop with carbon and chromium[59].

Figure 10 The *Fe-Cr-Ni* diagram at constant chromium[59].
A = austenite, F = ferrite.

Figure 11 *Fe-S-O* phase stability diagram and partial pressure relationship of oxygen and sulfur for $CO_2-10\%SO_2$ at 871°C.

Figure 12 (a) Fractured section through completely oxidized *Fe* exposed to $H_2-10\%H_2S$ for 1 min. at 871°C;

(b) Sulfur Auger electron map of (a).

Figure 13 (a) As Figure 12, but after 5 min. argon ion sputtering;

(b) Sulfur Auger electron map of (a).

Figure 14 (a) Auger electron spectrum at Points 1 (Figure 13);

(b) Auger electron spectrum at Points 2 (Figure 13).

Figure 15 (a) Intensity/depth profile during argon ion sputtering at Point 1;

(b) Intensity/depth profile during argon ion sputtering at Point 2.

Figure 16 Fractured section through 17 days oxidized *Cr* exposed to H_2–10%H_2S for 10 min. at 1000°C.

(a) Adsorption image;

(b) Sulfur Auger electron map;

(c) Sulfur Auger electron map after 2 min. argon ion sputtering.

Figure 17 (a) Auger spectrum;

(b) Composition/depth profile at Point 1 or Point 2 of Figure 16.

Figure 18 Weight gain vs time curves for *Fe* oxidized in H_2–10%H_2S, CO_2–10%SO_2, and air at 871°C.

Figure 19 Top view of the scale surface formed on *Fe* oxidized for 3 hrs in flowing CO_2–10%SO_2 at 871°C.

Figure 20 Cross-section of a fractured scale formed on *Fe* oxidized in CO_2–10%SO_2 for 3 hrs at 871°C.

Figure 21 Fractured cross-section of a protrusion formed on *Fe* oxidized in CO_2–10%SO_2 for 3 hrs at 871°C.

(a) SEM image;

(b) Sulfur map.

Figure 22 The inner layer of scale formed on *Fe* oxidized in CO_2–10%SO_2 at 871°C.

(a) Fractured section;

(b) Sulfur map.

Figure 23 Bottom view of the scale (the scale/metal interface) formed in CO_2–10%SO_2 for 3 hrs at 871°C.

(a) SEM image;

(b) Sulfur map.

Figure 24 Top view of the metal surface after the scale was removed.

Figure 25 Polished cross-section of the scale formed in CO_2–10%SO_2 at 871°C for 12 hrs.

Figure 26 Cross-section of the scale formed on *Fe* exposed to CO_2–10%SO_2 for a few hrs at 871°C.

Figure 27 Concentration profiles across the grains of a fractured section of the *Fe* scale oxidized in CO_2–10%SO_2.

(a) Point analysis of a sulfide-rich grain in Figure 26;

(b) Point analysis of an oxide-rich grain in Figure 26;

(c), (d) two point analyses of two *S*-rich grains in Figure 26.

Figure 28 *Fe-S-O* phase stability diagram and partial pressure relationship of oxygen and sulfur for 10%SO_2 at 871°C.

Point A: CO_2–10%SO_2;

Point B: in sulfide stable region;

Point C: *Air* –1%SO_2;

Point D: CO_2–37%CO;

Point E: CO_2.

Figure 29 Fractured cross-section of *Fe* oxidized in CO_2–37%CO for 2 days, subsequently exposed to CO_2–10%SO_2 for 3 hrs.

(a) SEM image of the scale corner;

(b) Sulfur map.

Figure 30 Mechanism for the formation of protrusions.

Figure 31 Top view of protrusions formed in CO_2–10%SO_2 for 3 hrs at 871°C.

(a) SEM image;

(b) Sulfur map.

(cooled down in a sulfur-containing atmosphere)

Figure 32 Bottom view of a fractured cross-section of the protrusion formed on *Fe* oxidized in CO_2–10%SO_2 for 3 hrs at 871°C.

Figure 33 Schematic diagram of the growth mechanism of oxide grains on the sulfide-rich core.

(a) Cations transport along the sulfide-rich core;

(b) Cations transport along oxide grains.

Figure 34 Top view of *Fe* sulfidized in H_2–10%H_2S for 1½ hrs, subsequently exposed to air for 4 min. at 871°C.

Figure 35 Schematic diagram of the growth of sulfur-induced wrinkles on oxide scale.

Figure 36 Schematic diagram of the growth mechanism of the porous scale formed on *Fe* exposed to CO_2–10%SO_2 at high temperature.

(dots represent sulfur distribution)

Figure 37 Schematic diagram of the formation mechanism of a porous protrusion.

(a) A protrusion formed in CO_2–10%SO_2 exposure;

(b) A protrusion covered with oxide;

(c) Sulfur in the protrusion diffusing inward;

(d) A porous protrusion formed.

Figure 38 SEM image of a fractured protrusion formed on *Fe* oxidized in CO_2–10%SO_2 for 3 hrs and subsequently exposed to air for 3 hrs at 871°C.

Figure 39 Fractured cross-section of the scale on *Fe* exposed to air for 1 hr, then to H_2–10%H_2S for 2 hrs, and subsequently exposed to air for another 3 hrs at 871°C.

(a) SEM image;

(b) Sulfur map.

Figure 40 Top view of the scale surface formed on *Fe-18Cr* oxidized for 48 hrs in flowing CO_2–10%SO_2 at 871°C.

Figure 41 (a) Enlarged picture of the center part of Figure 40;

(b) EDX analysis of the overall surface shown in (a).

Figure 42 Top view of the scale surface formed on *Fe-18Cr* oxidized for 100 hrs in air at 871°C.

(a) SEM image;

(b) Same as in (a) but higher magnification.

Figure 43 (a) Enlarged picture of the left part of Figure 40;

(b) EDX analysis of the overall surface shown in (a).

Figure 44 (a) Enlarged picture of the right part of Figure 40;

(b) EDX analysis of the overall surface shown in (a).

Figure 45 (a) Top view of the scale surface formed on *Fe-25Cr* oxidized for 48 hrs in flowing CO_2–10%SO_2 at 871°C;

(b) Enlarged picture of area P shown in (a).

Figure 46 (a) Enlarged picture of the center part of Figure 45;

(b) EDX analysis of area X shown in (a);

(c) EDX analysis of area Y shown in (a).

Figure 47 (a) Top view of the scale surface formed on *Fe-40Cr* oxidized for 110 hrs in flowing CO_2–10%SO_2 at 871°C;

(b) Enlarged picture of area Y shown in (a);

(c) Enlarged picture of area X shown in (a);

(d) Enlarged picture of the center part of the surface shown in (b).

Figure 48 (a) Top view of the scale surface formed on *Fe-18Cr* oxidized for 7 days in flowing CO_2–10%SO_2 at 871°C;

(b) Enlarged picture of the center part of the surface shown in (a).

Figure 49 (a) Top view of the alloy surface after the scale was removed manually;

(b) Iron map of (a);

(c) Sulfur map of (a);

(d) Chromium map of (a).

Figure 50 (a) Top view of the scale surface formed on *Fe-18Cr* preoxidized for 18 hrs in air and subsequently exposed to flowing CO_2–10%SO_2 for 32 hrs at 871°C;

(b) Enlarged picture of relatively flat area shown in (a);

(c) Enlarged picture of the nodule shown in (a);

(d) Another enlarged picture of relatively flat area shown in (a).

Figure 51 (a) Top view of the scale surface formed on *Fe-18Cr* preoxidized for 18 hrs in air and subsequently exposed to flowing CO_2–10%SO_2 for 32 hrs at 871°C;

(b) Chromium map of (a);

(c) Iron map of (a).

Figure 52 (a) Top view of the easy-spalling scale surface formed on *Fe-18Cr* preoxidized for 18 hrs in air and subsequently exposed to flowing CO_2–10%SO_2 for 32 hrs at 871°C;

(b) Top view of the alloy surface after the scale was removed.

Figure 53 (a) Microstructure of the alloy surface after the scale was removed;

(b) Auger analysis of grains indicated by arrow and white point in (a).

Figure 54 (a) Top view of the scale surface formed on *Fe-18Cr* preoxidized for 18 hrs in air and subsequently exposed to flowing CO_2–10%SO_2 for 6 hrs at 871°C;

(b) Top view of the etched alloy surface after the scale was removed by polishing.

Figure 55 (a) Polished cross-section of *Fe-10Al* exposed to flowing CO_2–10%SO_2 for 7 days at 871°C;

(b) Sulfur map of (a);

(c) Aluminum map of (a);

(d) Iron map of (a).

Figure 56 (a) Polished cross-section of *Fe-10Al* exposed to flowing CO_2–10%SO_2 for 7 days at 871°C;

(b) Same as in (a) but a different nodule.

Figure 57 The scale formed on iron-aluminum alloy by outward diffusion of iron cations similar to differential aeration cell.

Figure 58 (a) Polished cross-section of *Fe-10Al* exposed to flowing CO_2–10%SO_2 for 7 days at 871°C;

(b) The nodule/alloy interface shown in (a).

Figure 59 (a) Polished cross-section of the nodule/alloy interface of *Fe-10Al* exposed to flowing CO_2–10%SO_2 for 7 days at 871°C;

(b) Sulfur map of (a);

(c) Aluminum map of (a);

(d) Same as in (a) but higher magnification;

(e) Sulfur map of (d);

(f) Aluminum map of (d).

Figure 60 (a) Deep-etched cross-section of the nodule/alloy interface of *Fe-10Al* exposed to flowing CO_2–10%SO_2 for 7 days at 871°C;

(b) EDX analysis of Point P indicated by arrow in (a).

Figure 61 (a) Top view of the scale surface formed on *Fe-18Cr-3Al* exposed to flowing CO_2–10%SO_2 for 700 hrs at 871°C;

(b) Chromium map of (a);

(c) Aluminum map of (a);

(d) Iron map of (a).

Figure 62 (a) Auger spectrum at the area where scale spalled off as in the center part of Figure 61;

(b) Composition/depth profile of the same area as (a).

Figure 63 (a) Top view of the scale surface formed on *Fe-18Cr-3Al* oxidized for 700 hrs in flowing CO_2–10%SO_2 at 871°C;

(b) EDX analysis of grain indicated by arrow in (a).

Figure 64 Underside of the scale formed on *Fe* sulfidized for 2 hrs in H_2–10%H_2S at 871°C.

(a) SEM image;

(b) Same as in (a) but higher magnification.

Figure 65 (a) Polished cross-section of *Fe-18Cr* exposed to flowing CO_2–10%SO_2 for 48 hrs at 871°C;

(b) Same as in (a) but of *Fe-25Cr*.

Figure 66 (a) Top view of the scale surface formed on *Fe-10Al* presulfidized in flowing H_2–10%H_2S for 1 hr, subsequently oxidized in air for 19 hrs

at 871°C;

(b) Enlarged picture of area b in (a);

(c) EDX analysis of area d in (a).

(d) EDX analysis of area c in (a).

Figure 67 (a) Polished cross-section of *Fe-10Al* presulfidized in H_2–10%H_2S for 1 hr, subsequently exposed to air for 19 hrs at 871°C;

(b) Aluminum map of (a);

(c) Sulfur map of (a);

(d) Iron map of (a).

Figure 68 (a) Enlarged picture of the dense/porous layer interface of Figure 67;

(b) Sulfur map of (a).

Figure 69 (a) Polished cross-section of the nodule/alloy interface of *Fe-10Al* preoxidized in H_2–10%H_2S for 1 hr, subsequently exposed to air for 19 hrs at 871°C;

(b) Aluminum map of (a);

(c) Sulfur map of (a);

(d) Iron map of (a).

Figure 70 The mechanism for the formation of porous layer near the scale/alloy interface of an iron-chromium alloy.

Figure 71 (a) Polished cross-section of *Fe-18Cr* exposed to flowing H_2–10%H_2S for 2 hrs at 871°C;

(b) The scale/alloy interface shown in (a).

Figure 72 (a) Underside of the scale formed on *Fe-18Cr* sulfidized for 2 hrs in H_2–10%H_2S at 871°C;

(b) Same as in (a) but the top view of the alloy surface after the scale was removed.

Figure 73 Fractured cross-section of the scale formed on *Fe* sulfidized in H_2–10%H_2S for 2 hrs at 871°C.

(a) SEM image;

(b) Enlarged picture of the area shown in (a).

Figure 74 (a) Polished cross-section of *Fe-10Al* presulfidized in H_2–10%H_2S for 1 hr, subsequently exposed to air for 19 hrs at 871°C;

(b) Iron map of (a);

(c) Chromium map of (a);

(d) Sulfur map of (a);

(e) Aluminum map of (a).

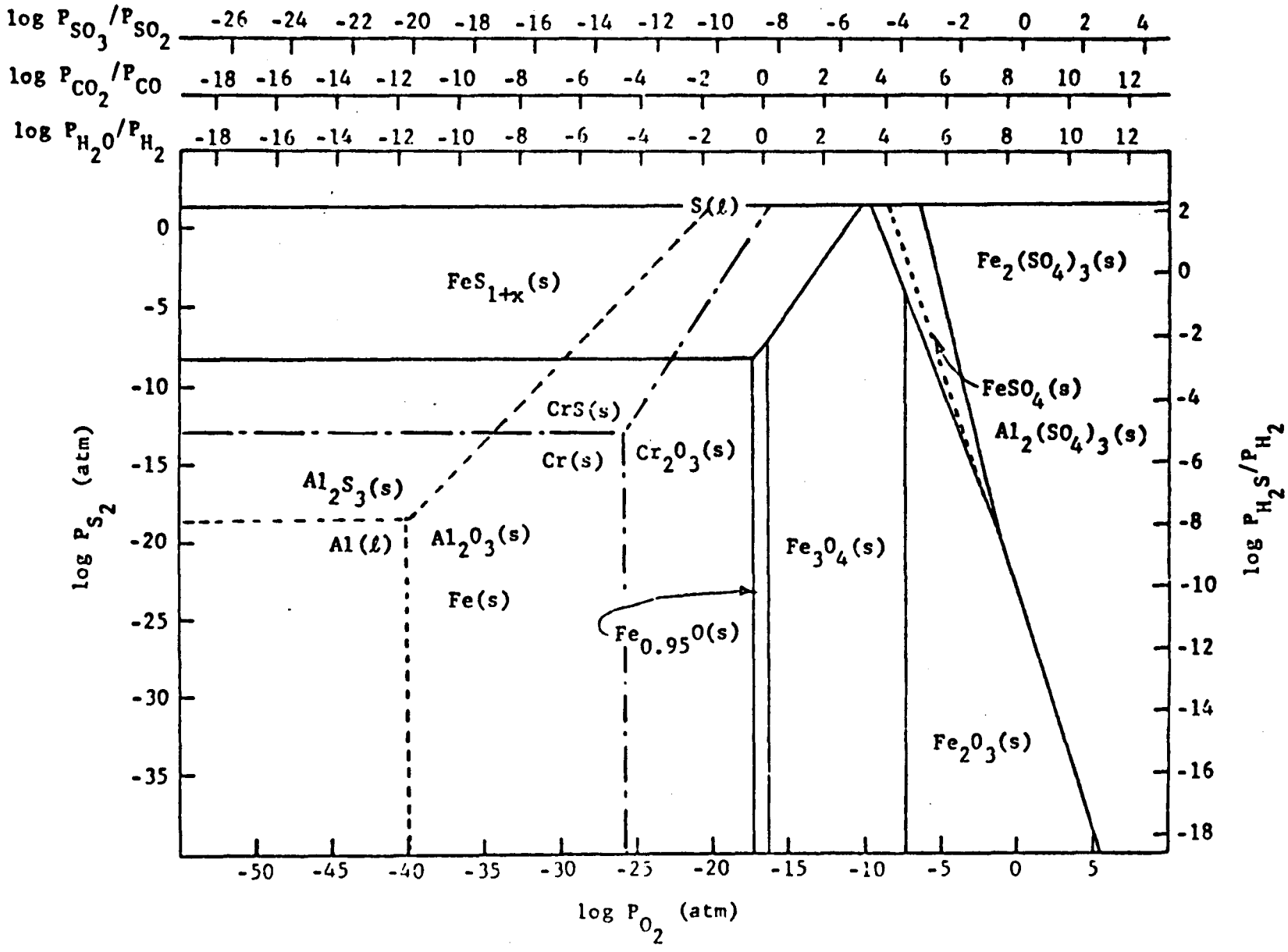
log P_{SO_3}/P_{SO_2}
-26 -24 -22 -20 -18 -16 -14 -12 -10 -8 -6 -4 -2 0 2 4
log P_{CO_2}/P_{CO}
-18 -16 -14 -12 -10 -8 -6 -4 -2 0 2 4 6 8 10 12
log P_{H_2O}/P_{H_2}
-18 -16 -14 -12 -10 -8 -6 -4 -2 0 2 4 6 8 10 12
S(ℓ)
FeS_{1+x}(s)
$Fe_2(SO_4)_3$(s)
$FeSO_4$(s)
$Al_2(SO_4)_3$(s)
CrS(s)
Cr(s)
Cr_2O_3(s)
Al_2S_3(s)
Al(ℓ)
Al_2O_3(s)
Fe(s)
Fe_3O_4(s)
$Fe_{0.95}O$(s)
Fe_2O_3(s)
log P_{S_2} (atm)
0 -5 -10 -15 -20 -25 -30 -35
log P_{H_2S}/P_{H_2}
2 0 -2 -4 -6 -8 -10 -12 -14 -16 -18
-50 -45 -40 -35 -30 -25 -20 -15 -10 -5 0 5
log P_{O_2} (atm)

Figure 1

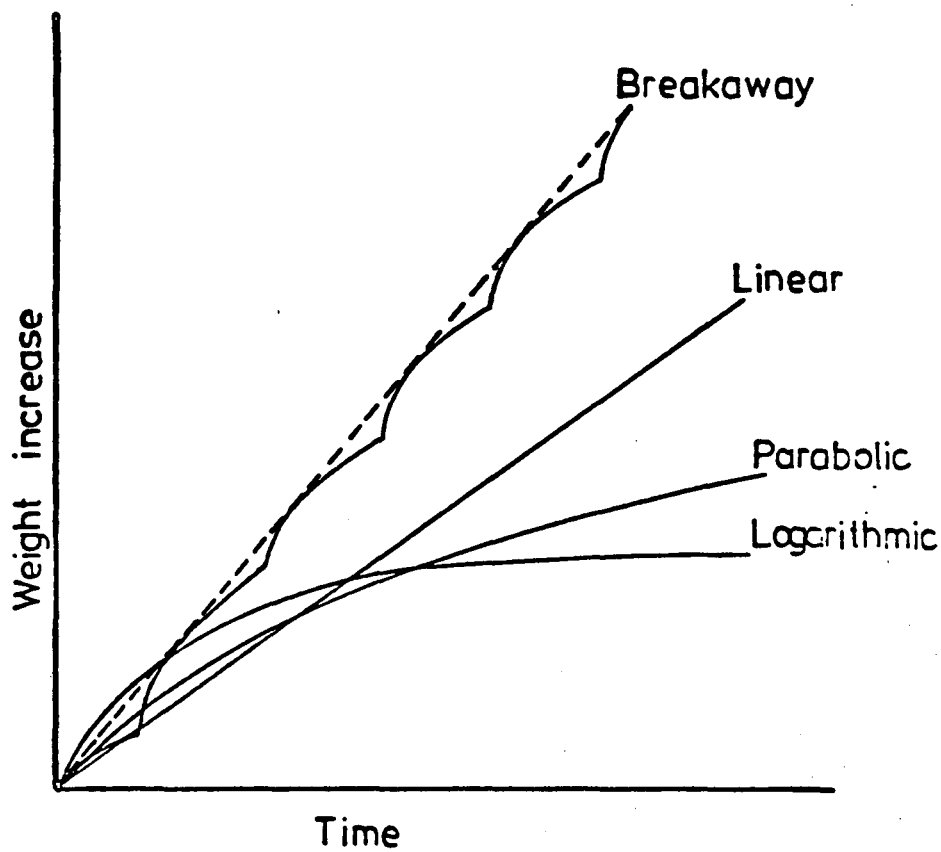
Breakaway
Linear
Parabolic
Logarithmic
Weight increase
Time

Figure 2

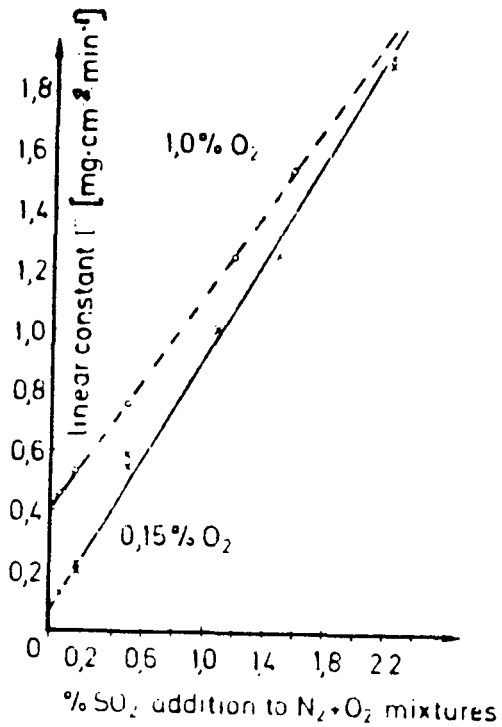

Figure 3

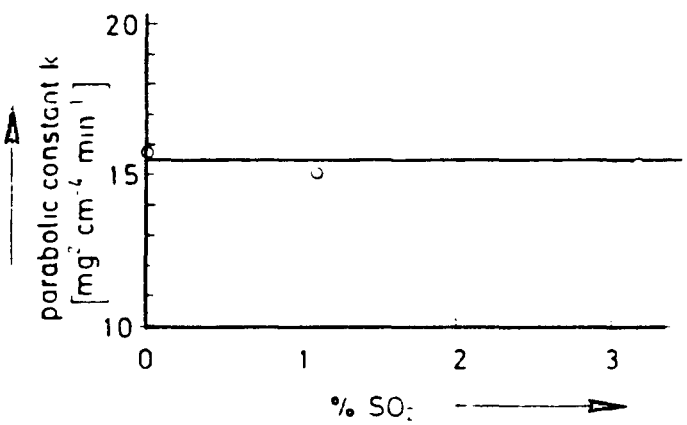

Figure 4 XBL 815-9919

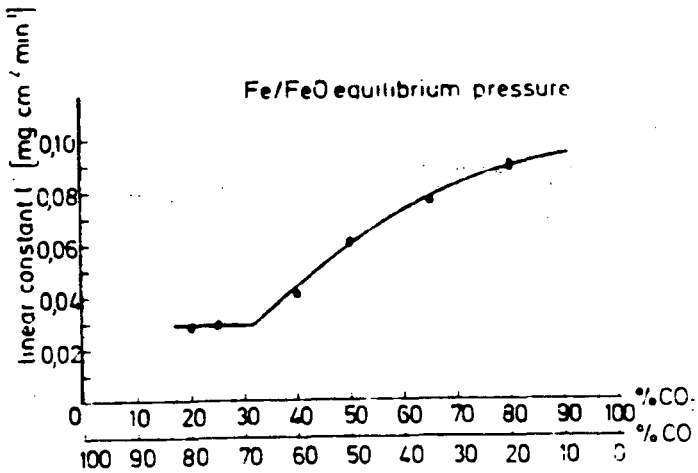

Figure 5

Rate determined step of reaction	Rate law	Conc. gradients in the scale and in the convective diffusion boundary layer	Effect of second oxidant on 1 rate	2 composition of scale
Reaction at the Fe/FeX phase boundary	complex	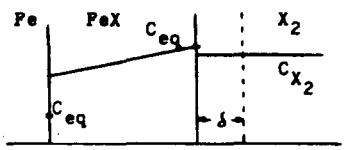	no effect	Fe-oxides or Fe-sulfides
Diffusion in FeX	parabolic $x^2 = k \cdot t$	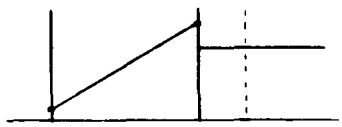	no effect	Fe-oxides or Fe-sulfides
Reaction at the FeX/X_2 phase boundary	linear $x = k \cdot t$	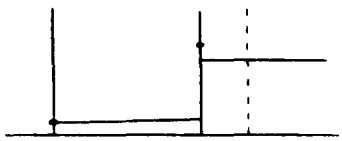	rate increases	FeO+FeS
Transport in the gas phase	linear $x = k \cdot t$		rate increases	FeO+FeS

Figure 6

XBL 815-9917

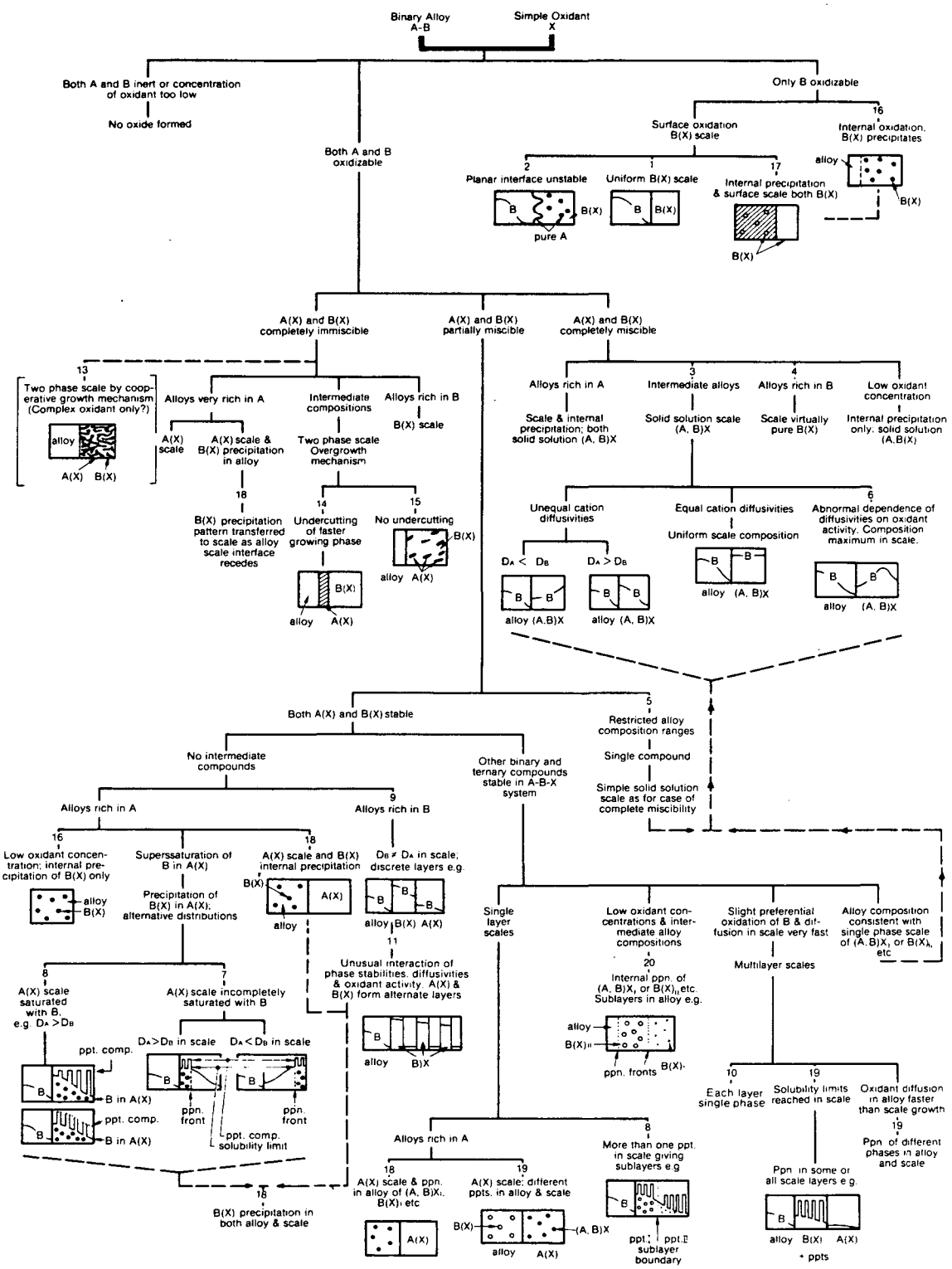

Figure 7

XBL 808-11342

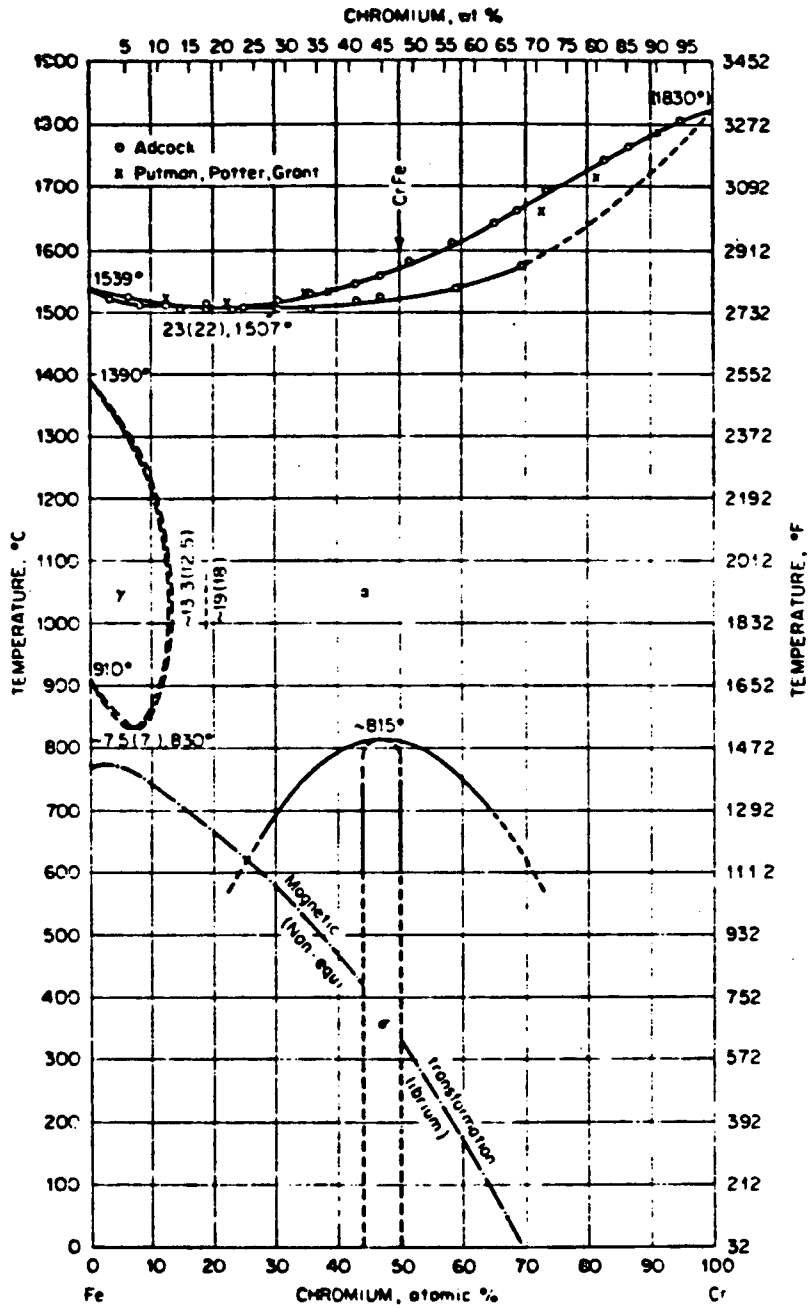
CHROMIUM, wt %
5 10 15 20 25 30 35 40 45 50 55 60 65 70 75 80 85 90 95
1800 1700 1600 1500 1400 1300 1200 1100 1000 900 800 700 600 500 400 300 200 100 0
3452 3272 3092 2912 2732 2552 2372 2192 2012 1832 1652 1472 1292 1112 932 752 572 392 212 32
TEMPERATURE, °C
TEMPERATURE, °F
Adcock
Putman, Potter, Grant
Cr/Fe
1539°
23(22), 1507°
1390°
910°
7.5(7), 830°
~13.3(12.5)
~19(18)
γ
α
~815°
(1830°)
Magnetic
(Non-equ.)
transformation
(Equilibrium)
0 10 20 30 40 50 60 70 80 90 100
Fe
CHROMIUM, atomic %
Cr

Figure 8

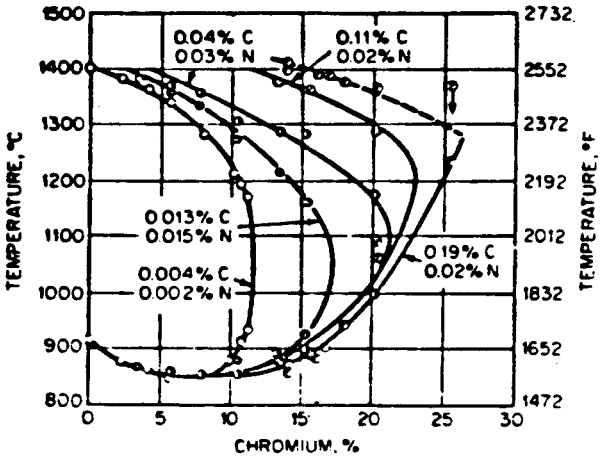

Figure 9

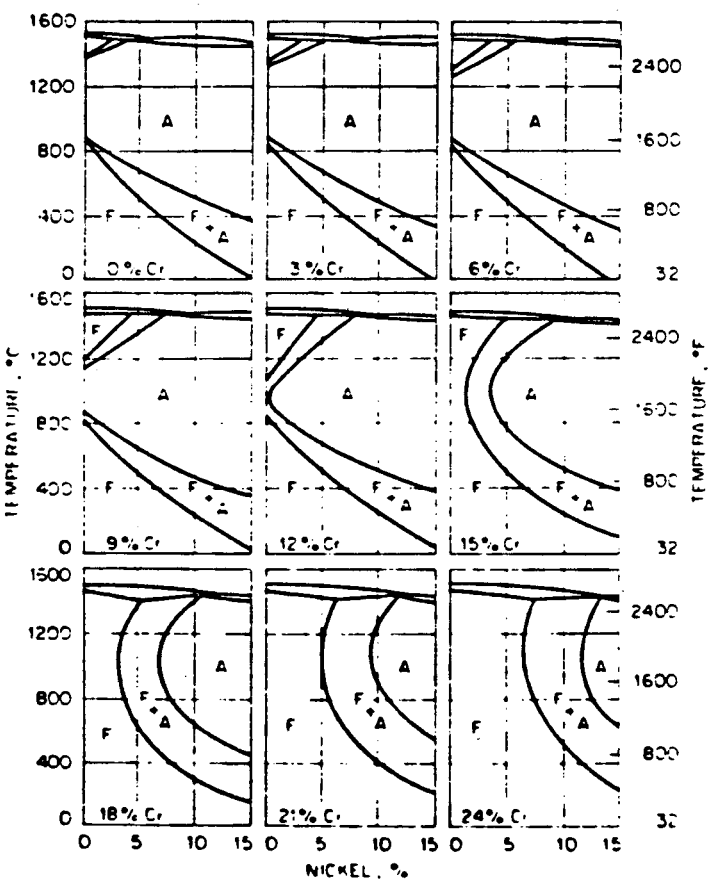

Figure 10

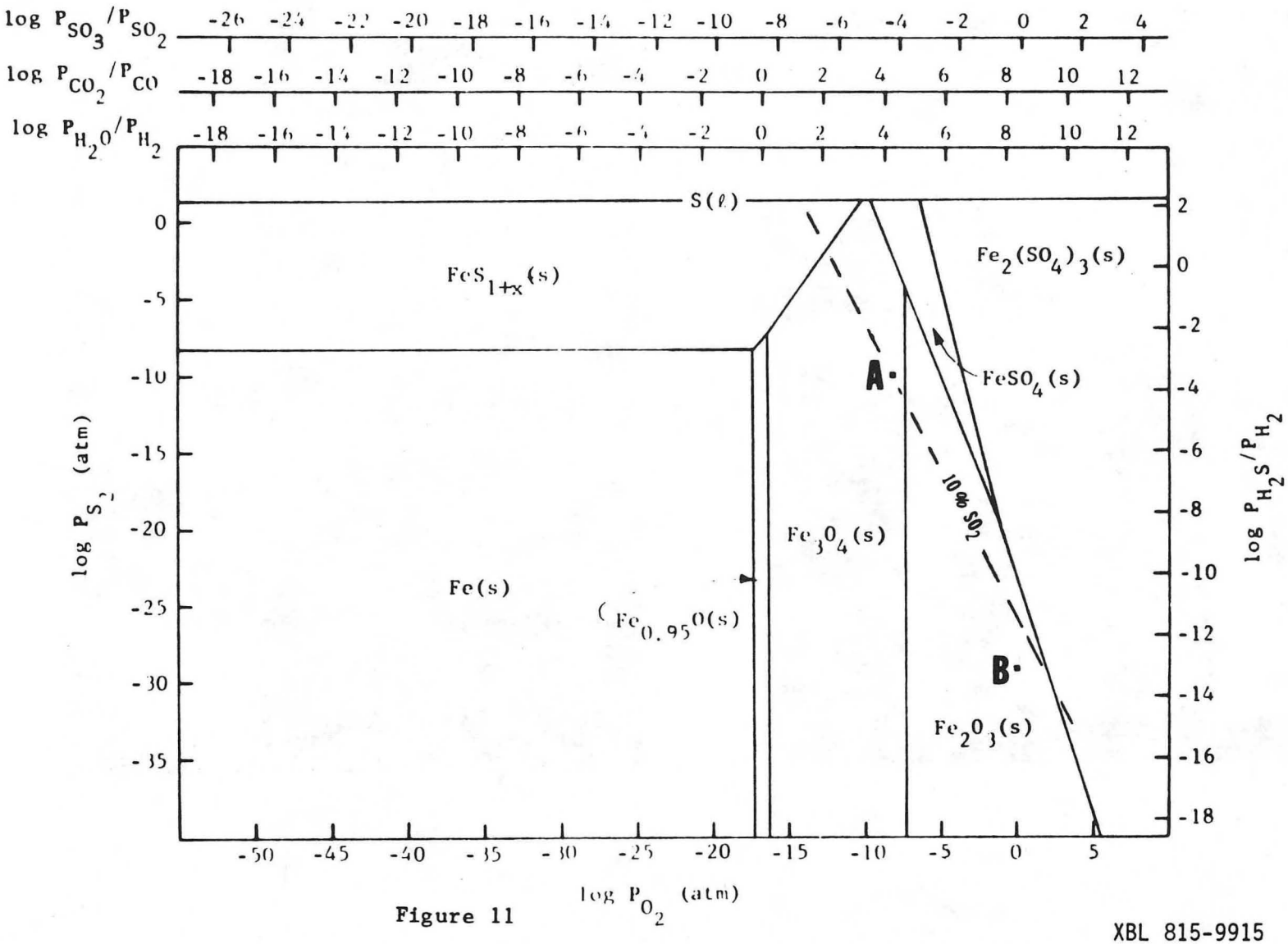

Figure 11

XBL 815-9915

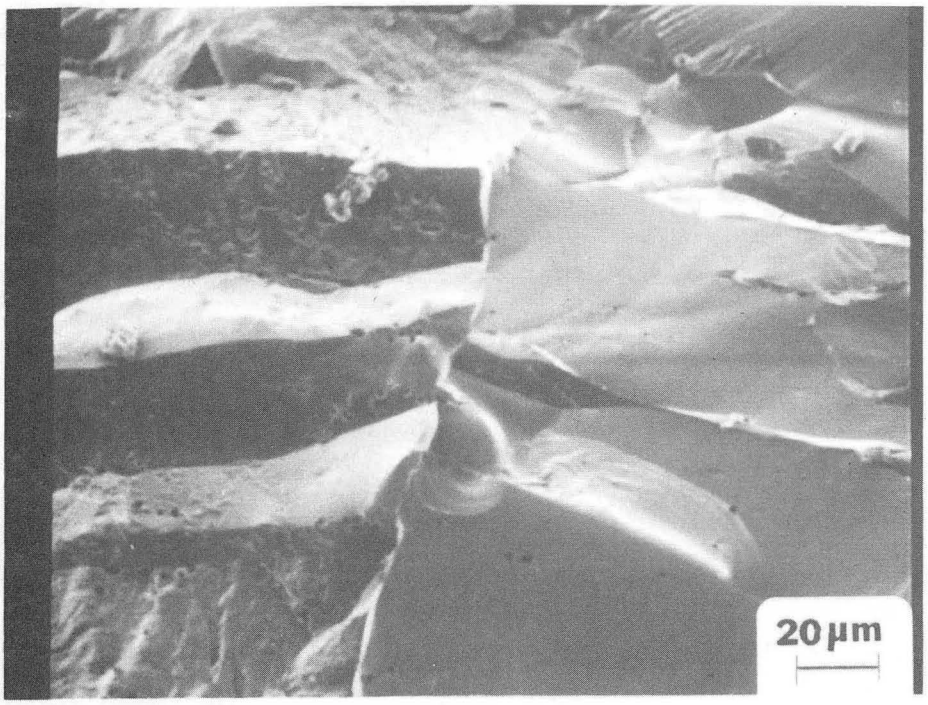

(a)

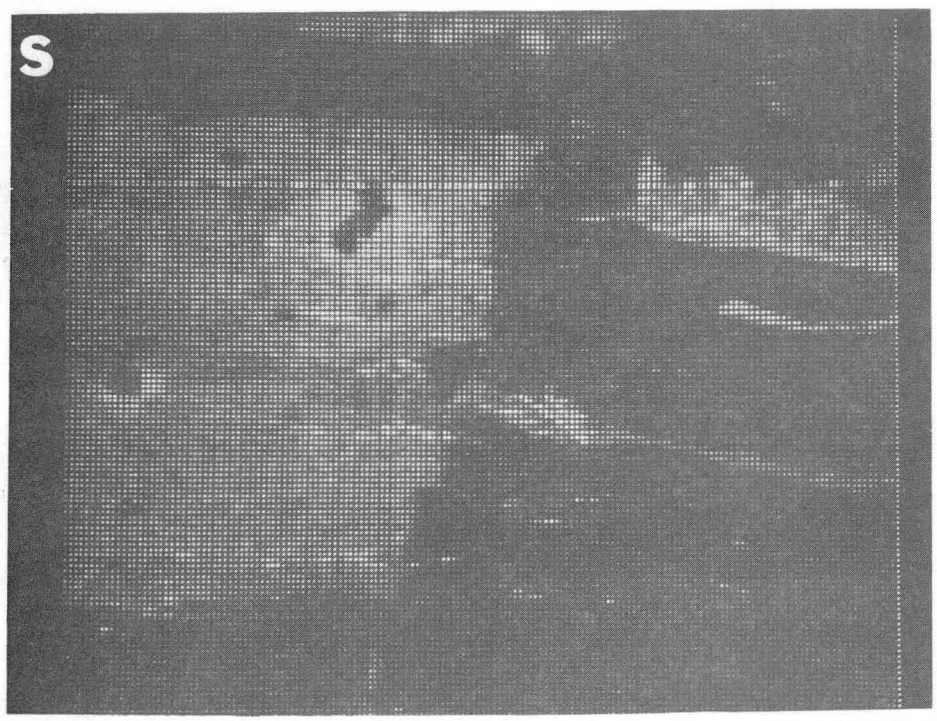

(b)

XBB 824-4090

Figure 12

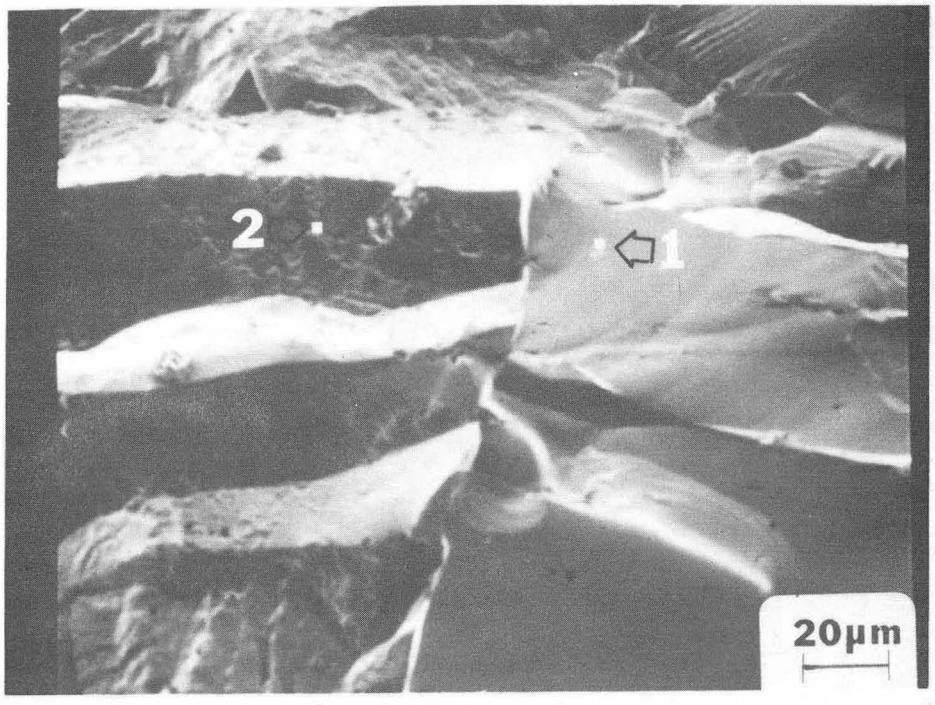

(a)

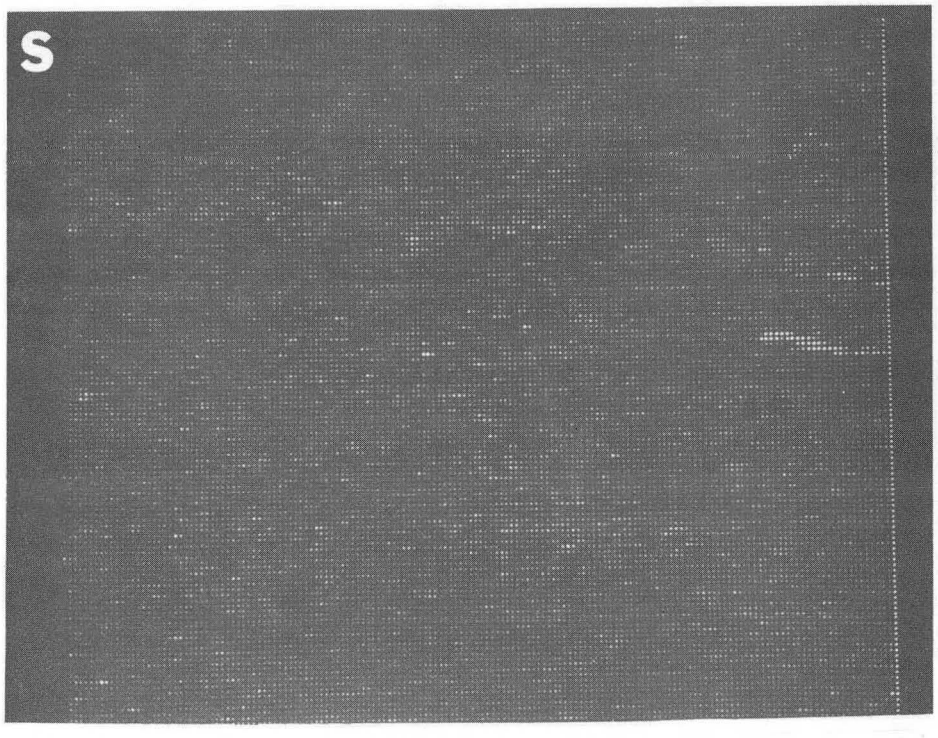

(b) XBB 824-4091

Figure 13

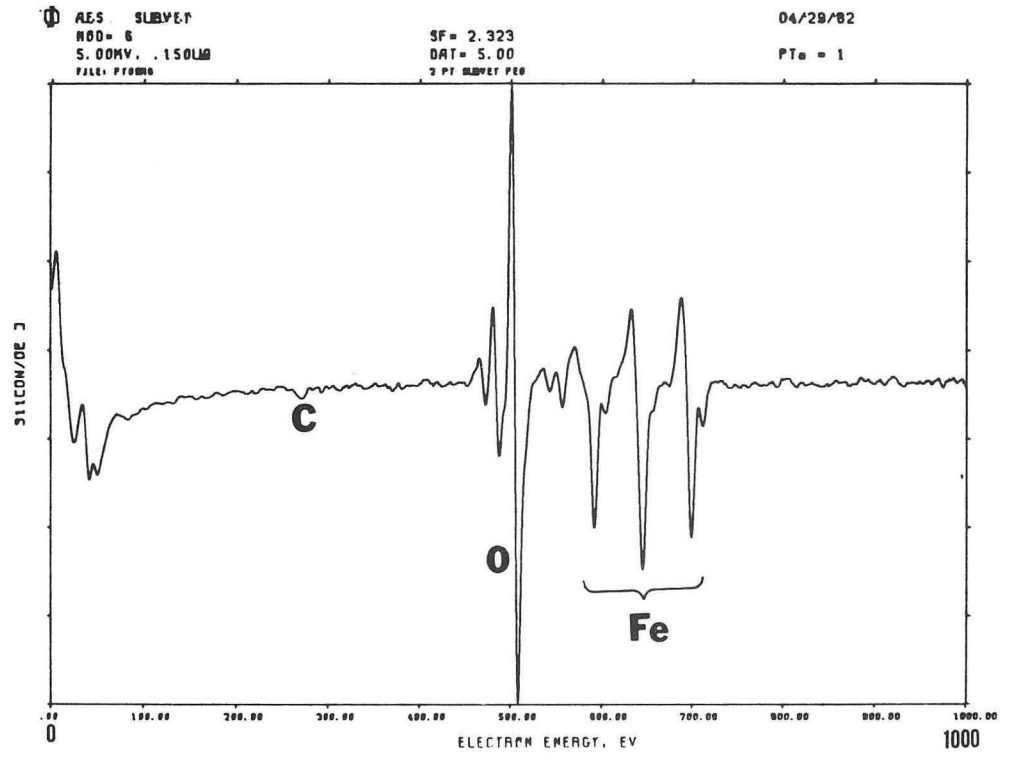

(a)

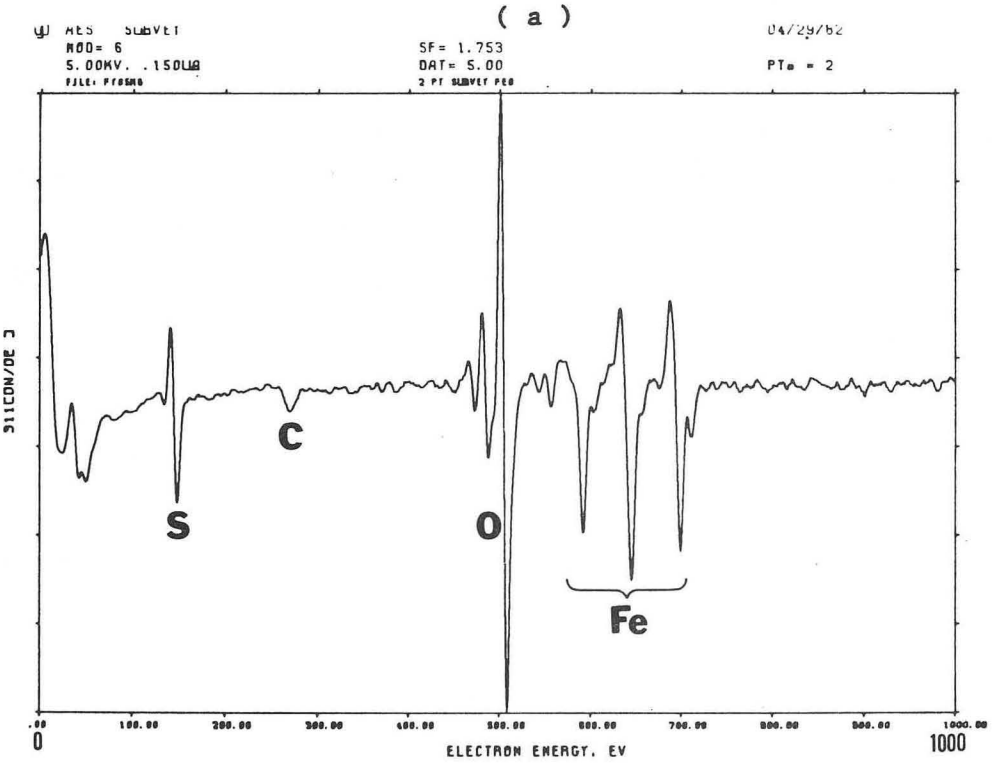

(b)

XBL 825-9754

Figure 14

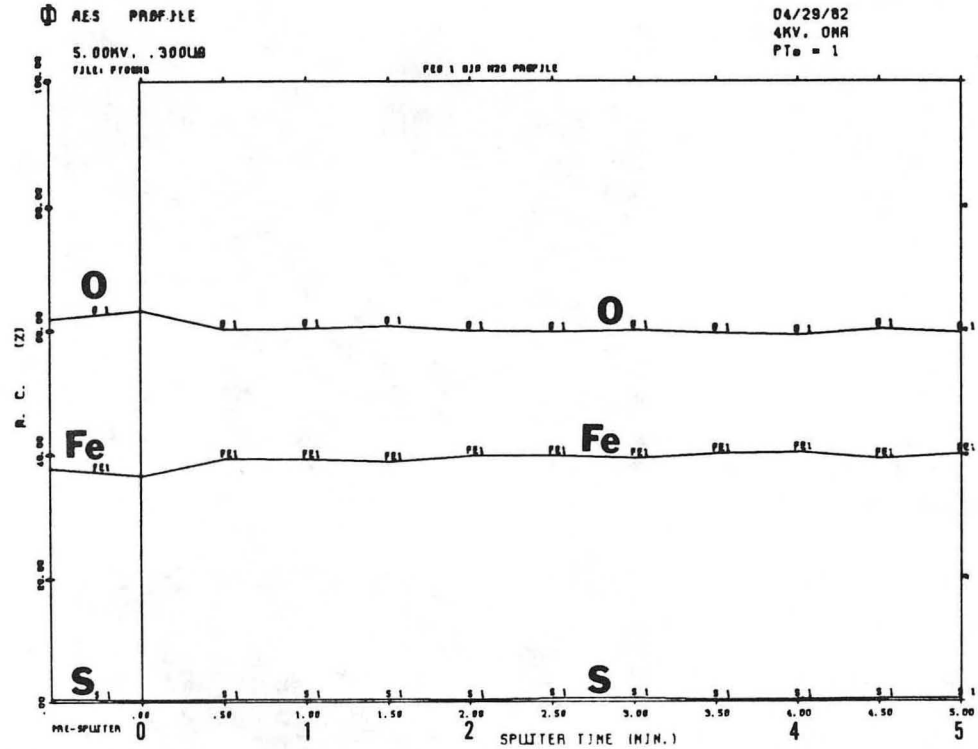

(a)

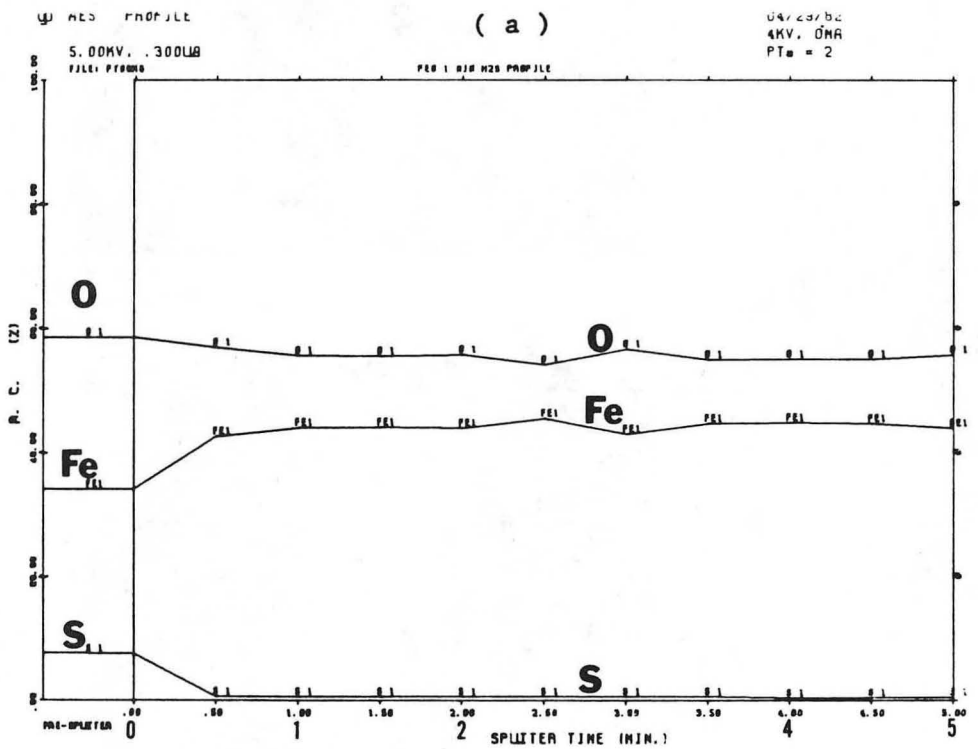

(b)

XBL 825-9755

Figure 15

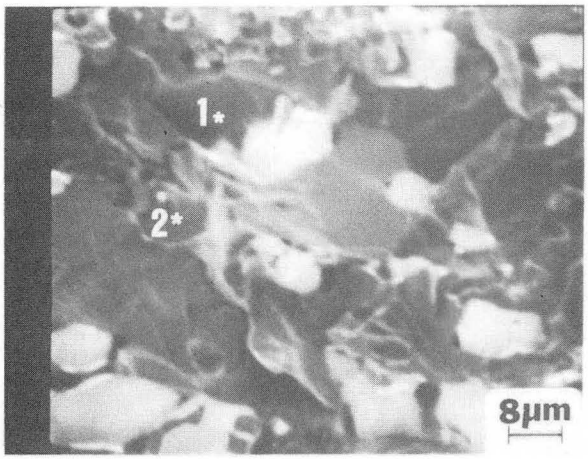

(a)

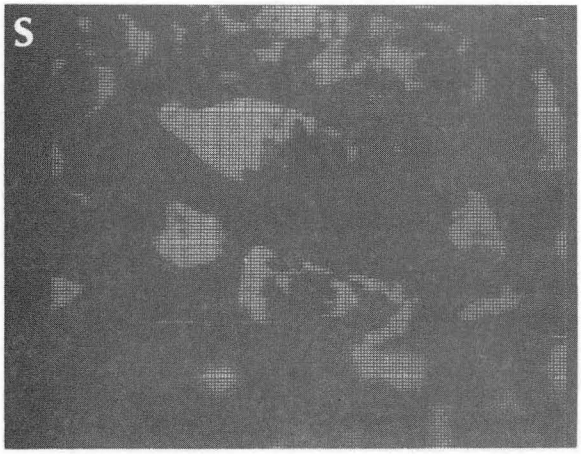

(b)

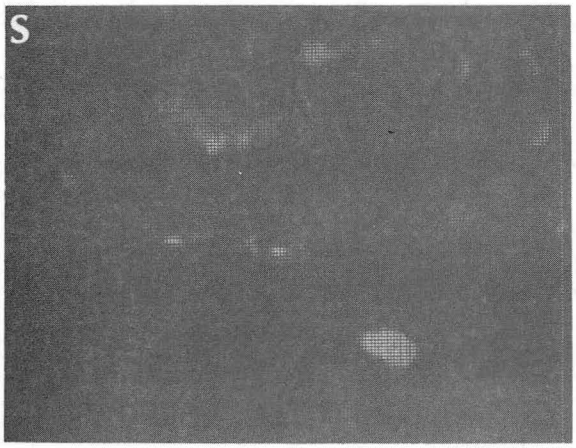

(c) XBB 829-7712

Figure 16

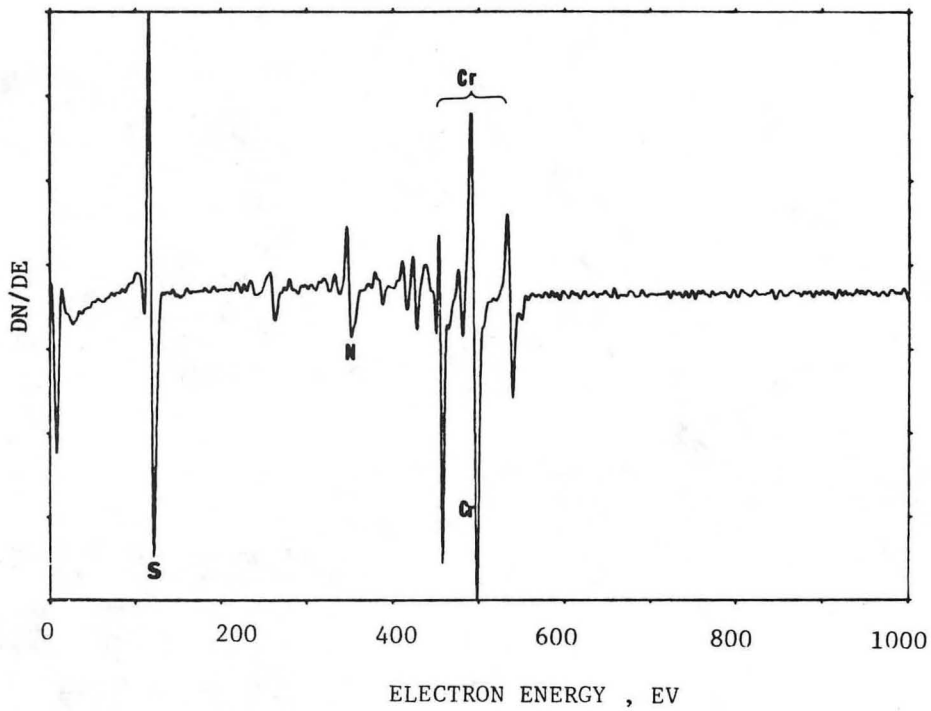

(a)

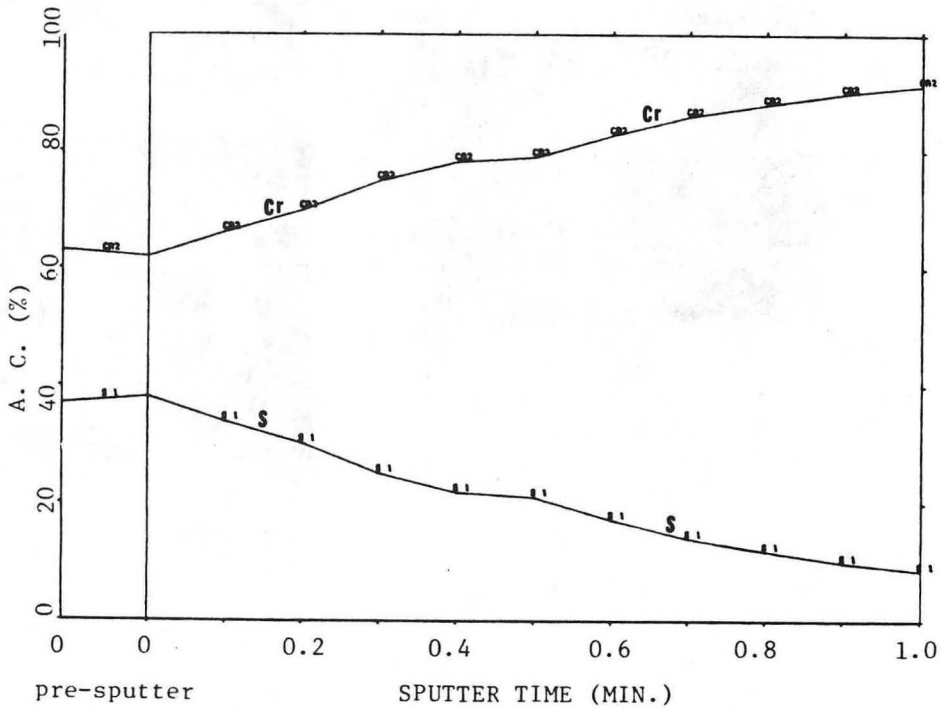

(b)

XBL 829-11477

Figure 17

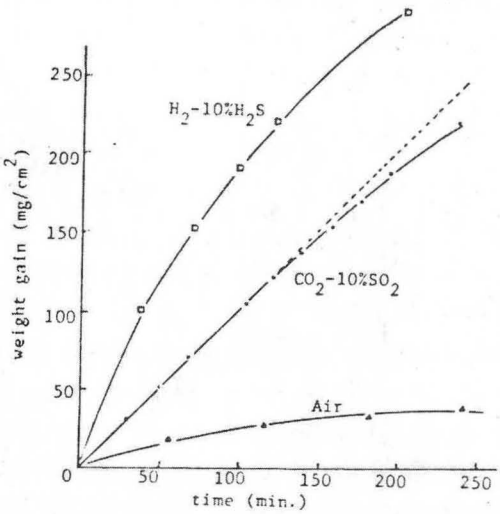

Figure 18

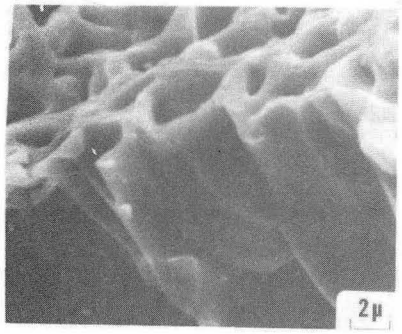

Figure 20

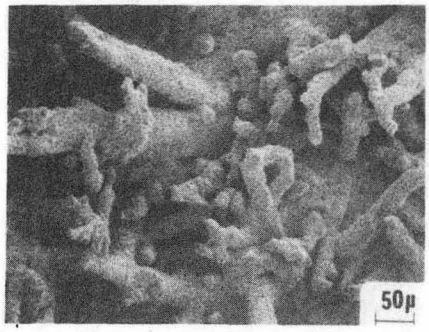

Figure 19

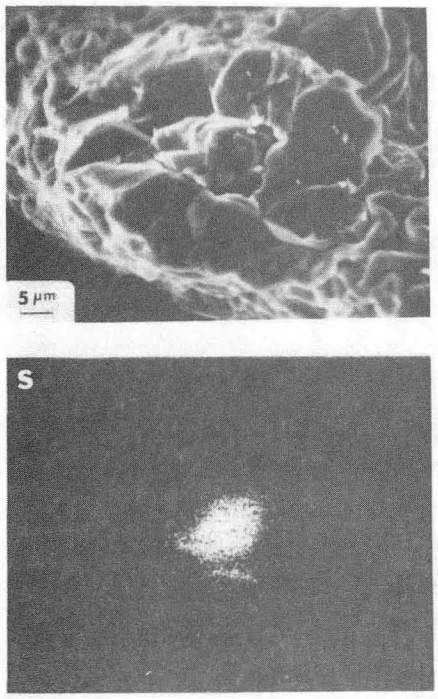

XBB 820-9622

Figure 21

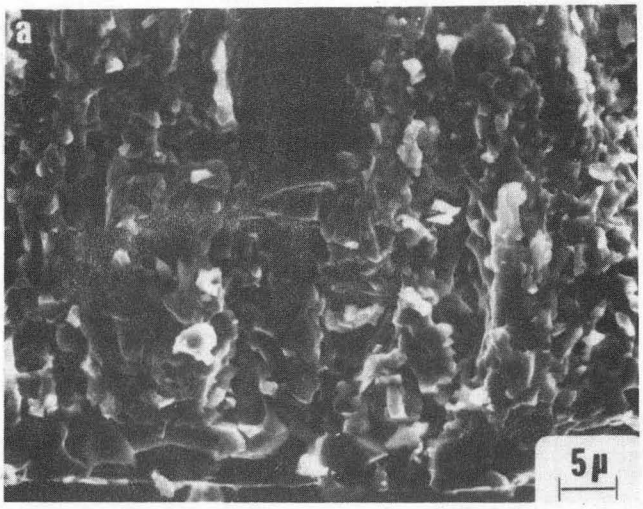

Inner layer

large grains layer

(a)

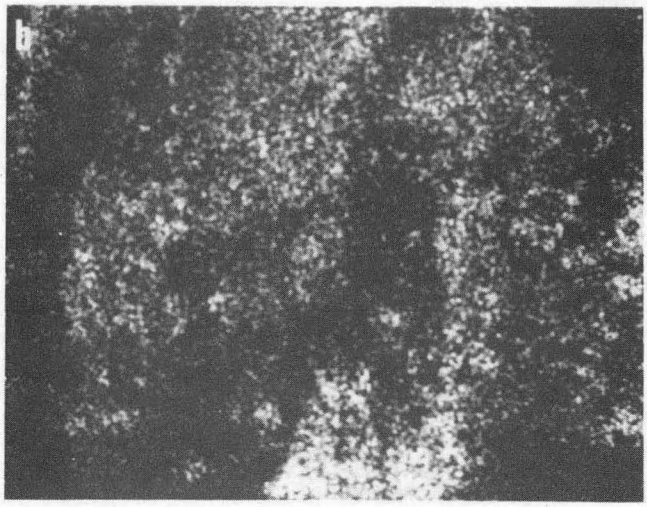

(b)

XBB 820-9623

Figure 22

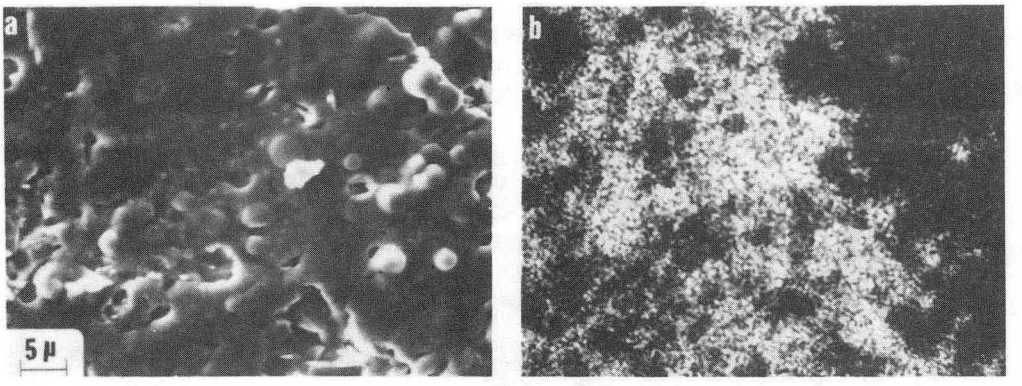

(a) (b)

Figure 23

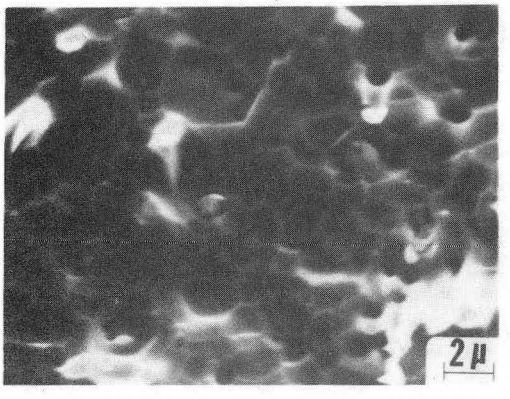

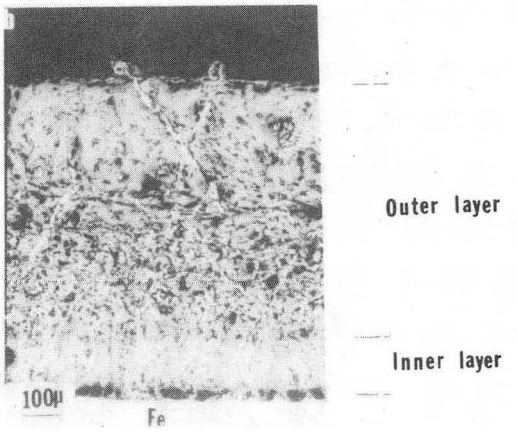

XBB 820-9624

Figure 24

Figure 25

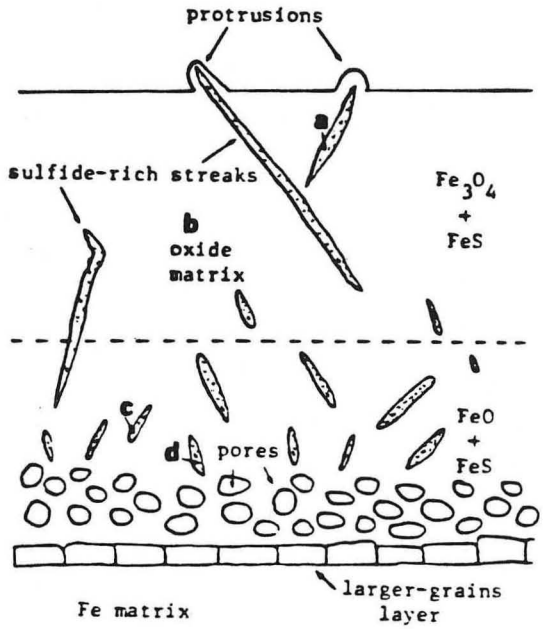

Figure 26

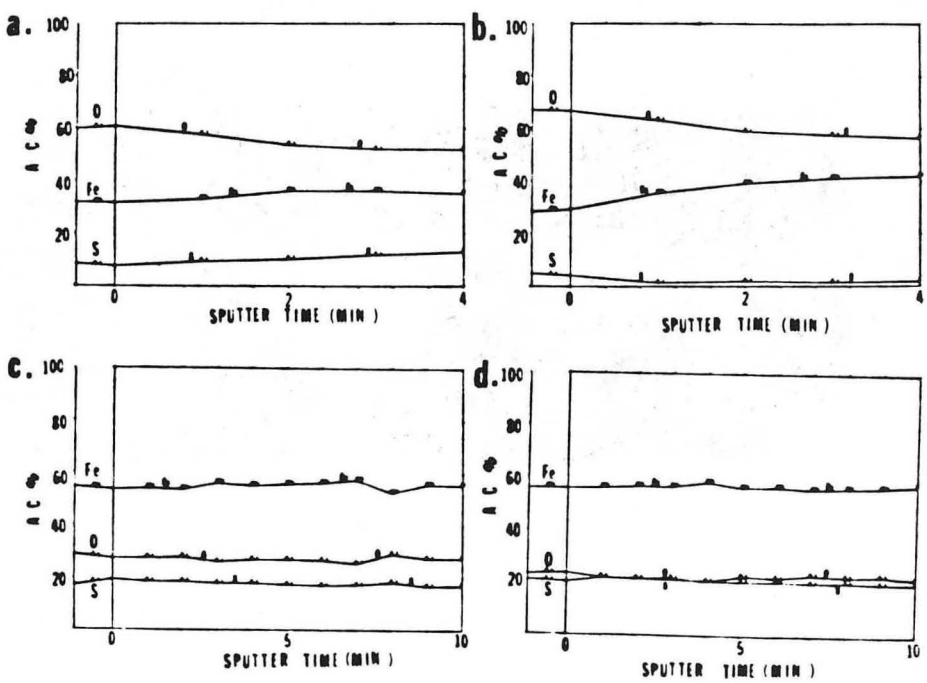

Figure 27

XBL 8211-3287

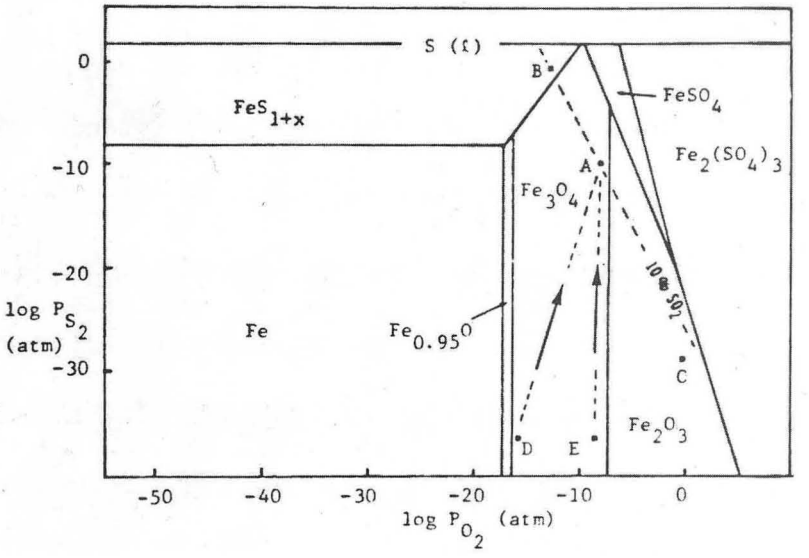

Figure 28

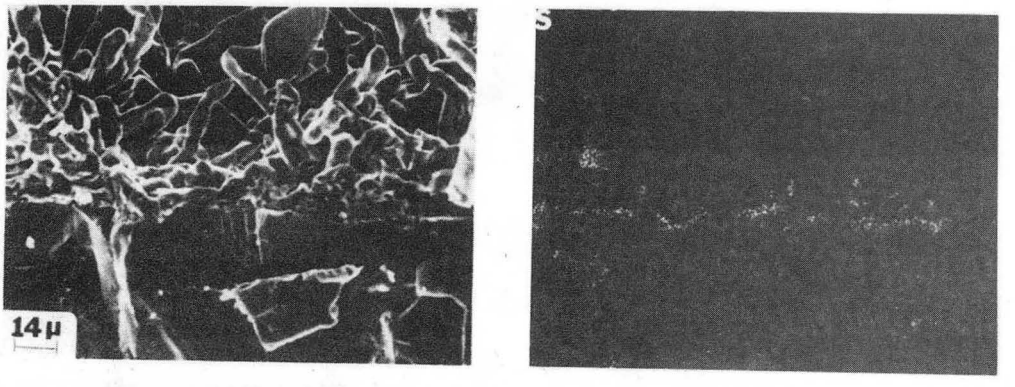

(a) (b)

XBB 820-9625

Figure 29

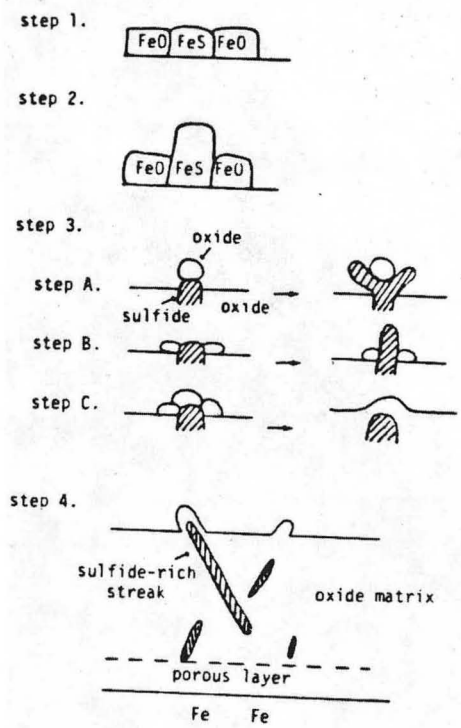

Figure 30

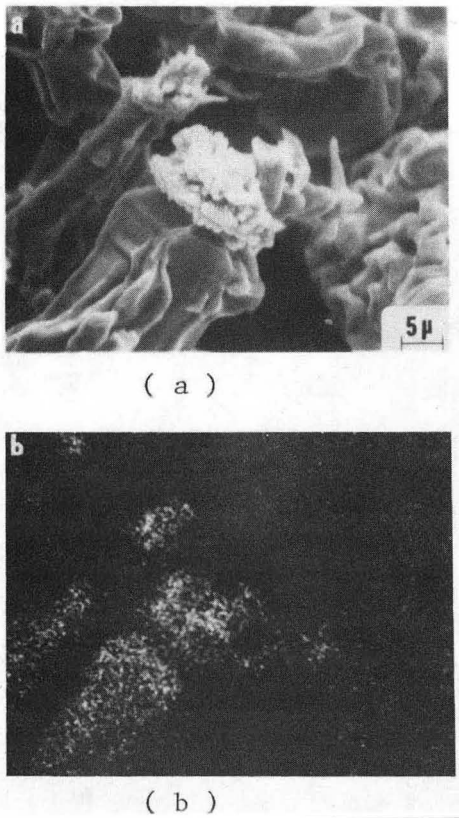

XBB 820-9621

Figure 31

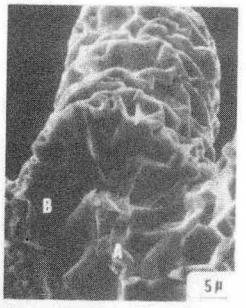

A—Sulfur rich core

B—Oxide

Figure 32

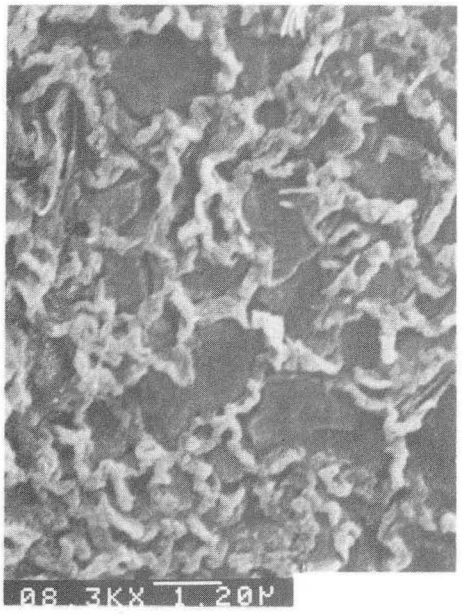

Figure 34

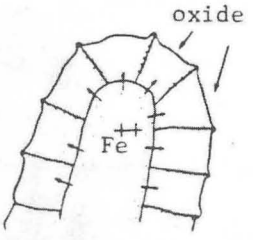

S-rich core

(a)

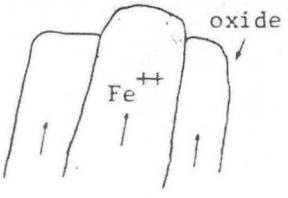

S-rich core

(b)

Figure 33

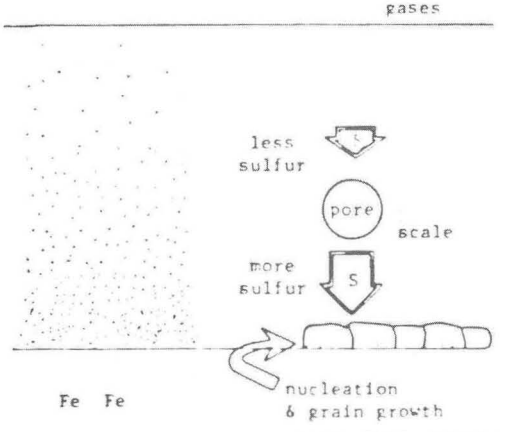

XBB 820-9626

Figure 36

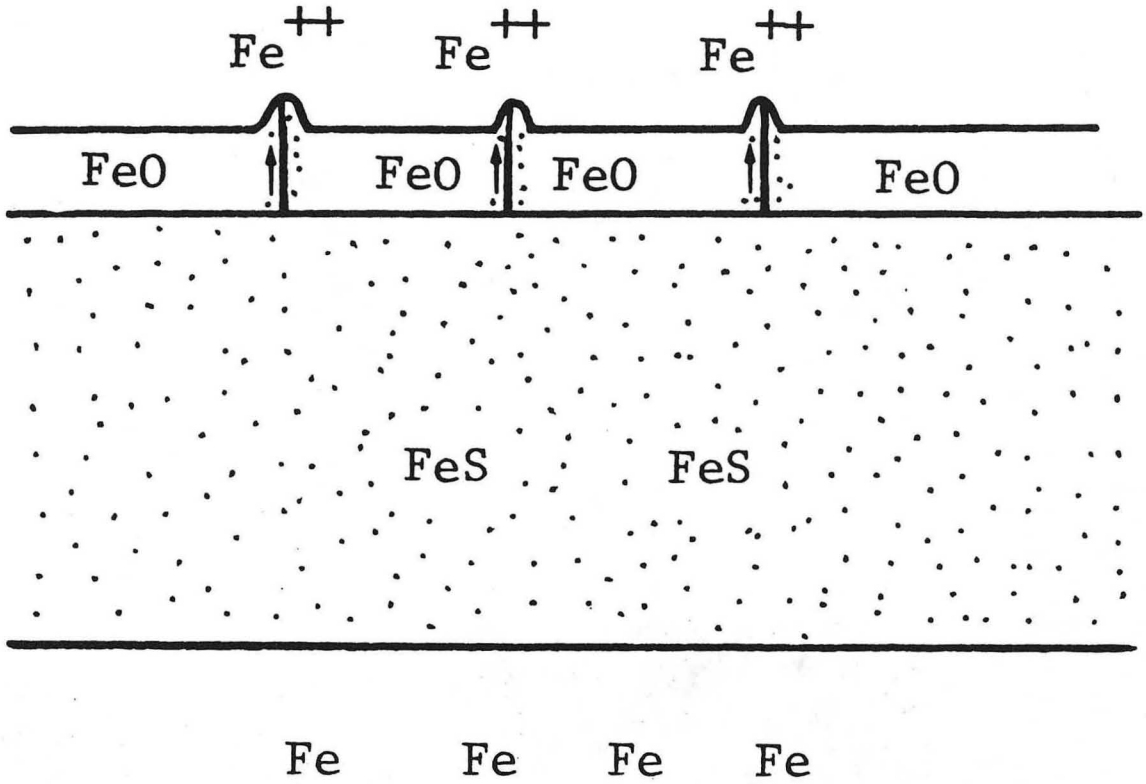

XBL 8210-2919

Figure 35

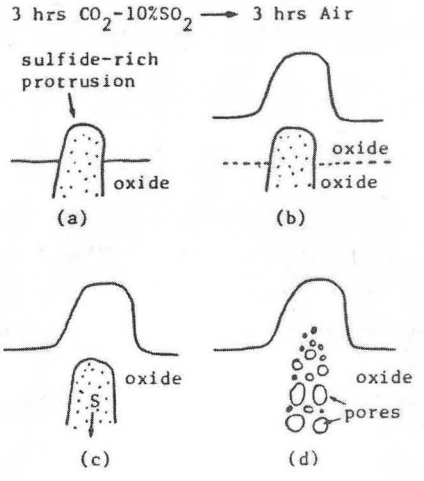

Figure 37

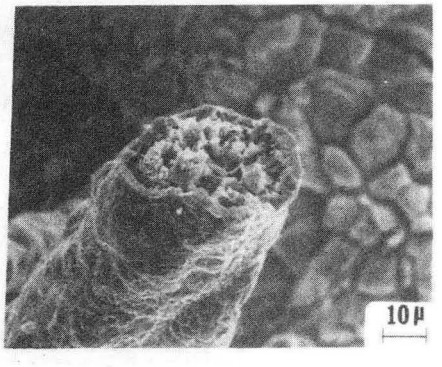

Figure 38

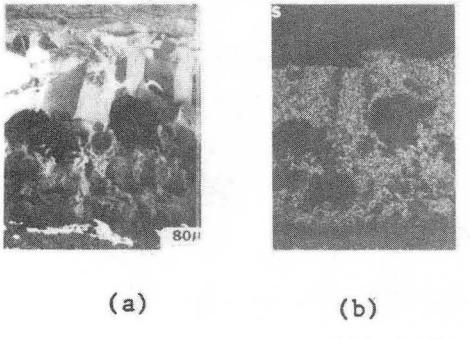

XBB 820-9627

Figure 39

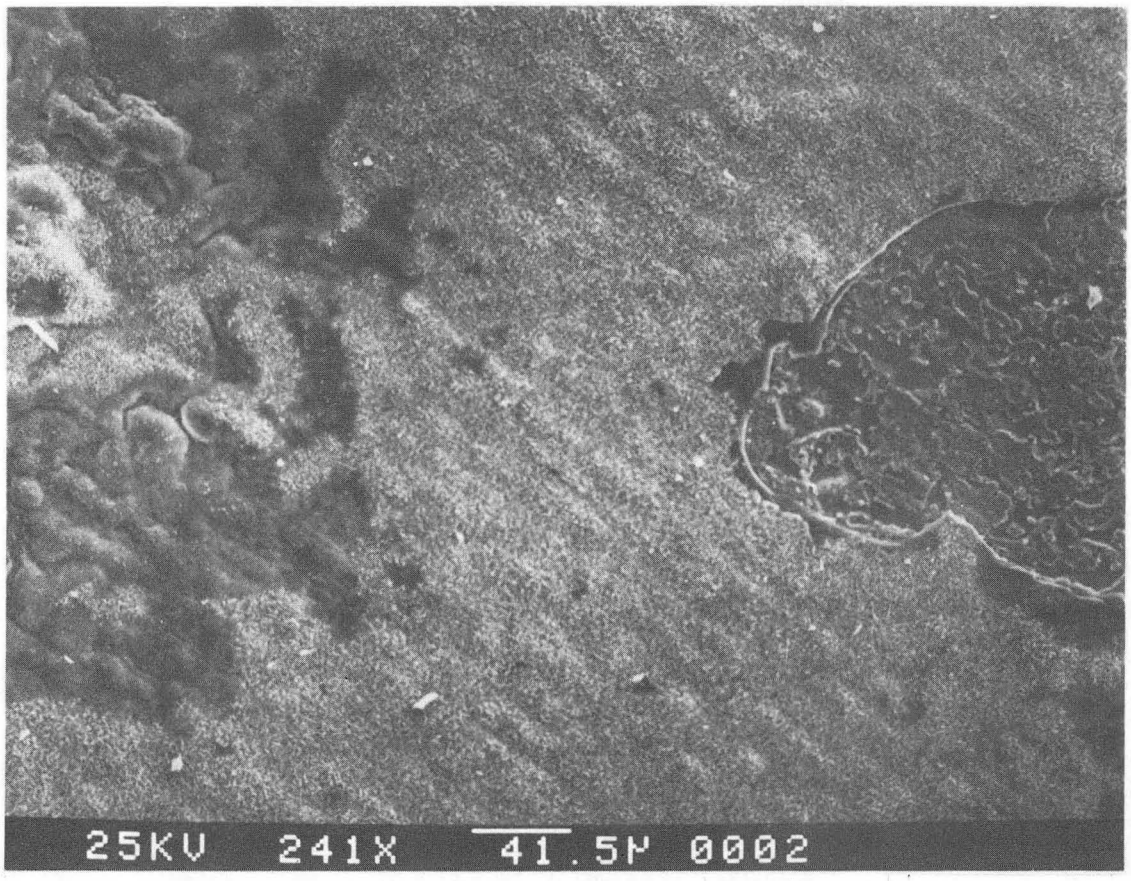

XBB 831-235

Figure 40

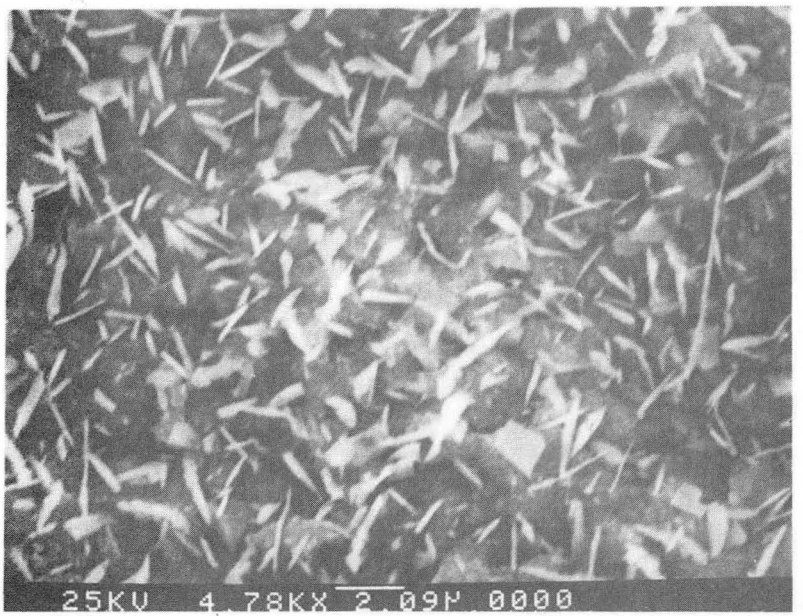

(a)

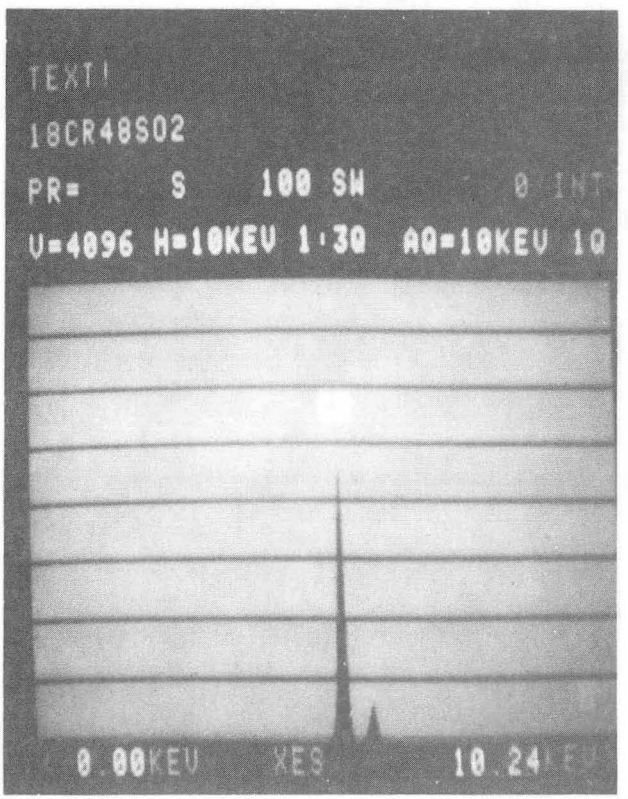

XBB 831-231

(b)

Figure 41

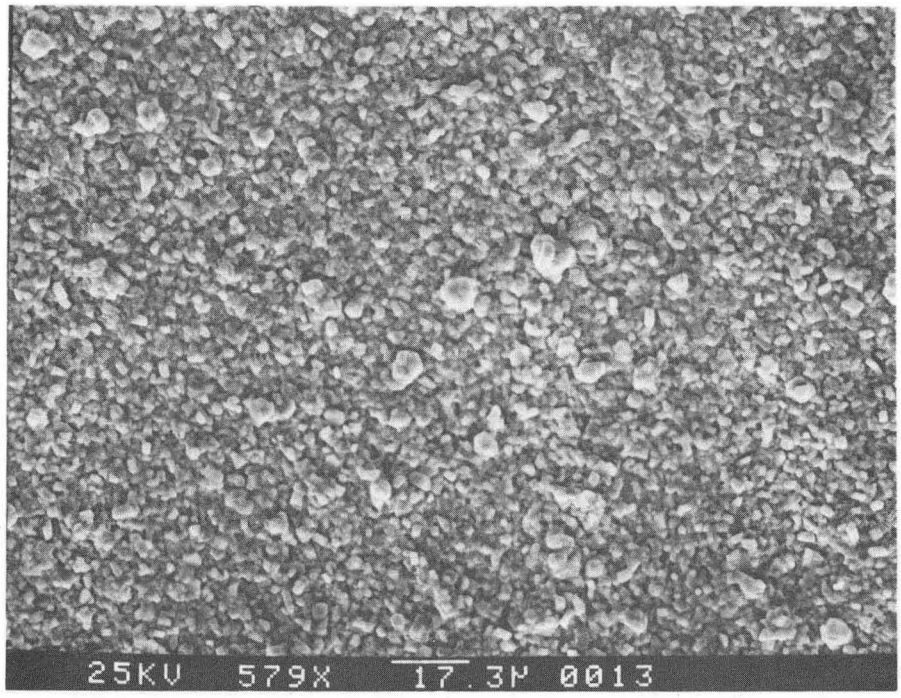

(a)

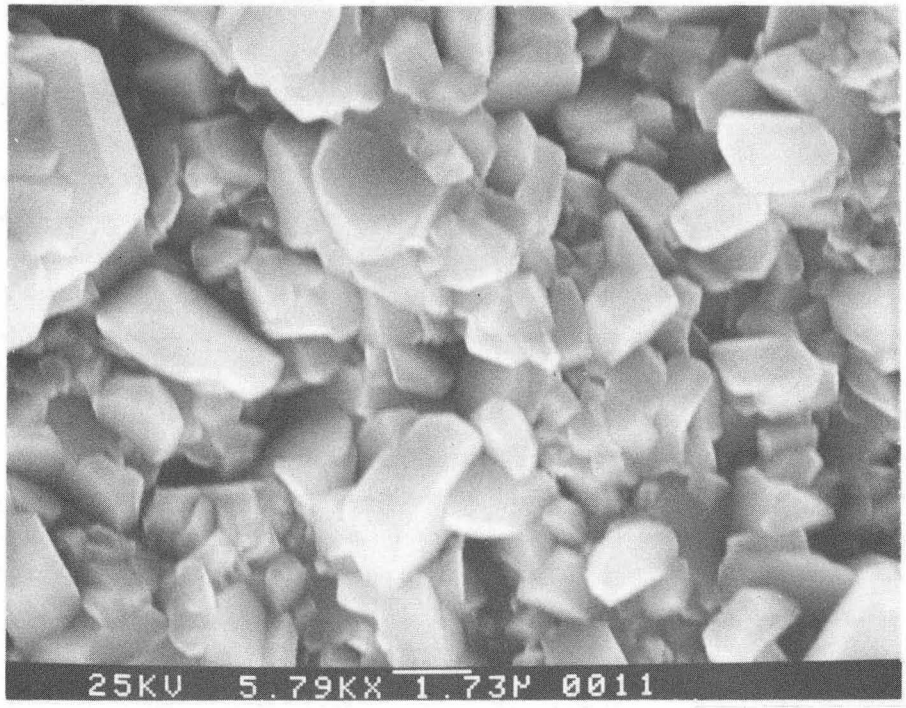

(b)

XBB 828-7465

Figure 42

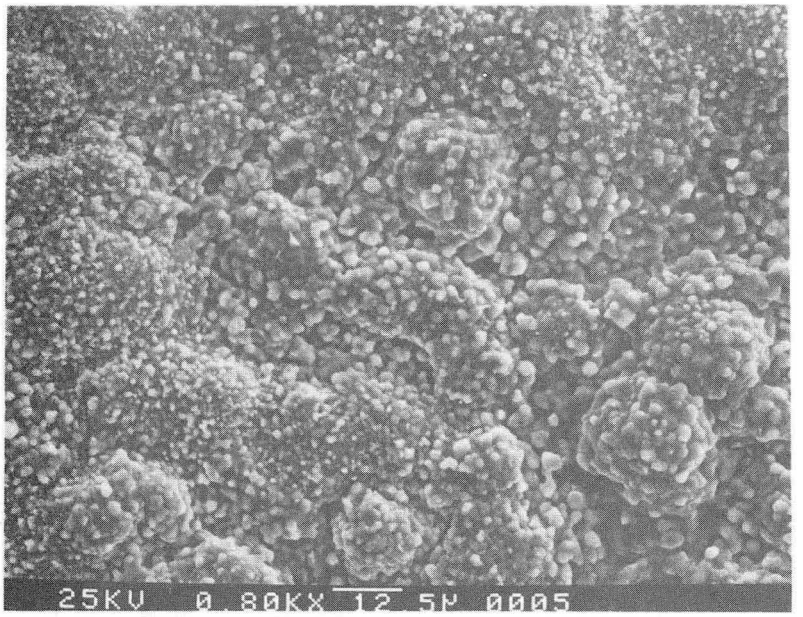

(a)

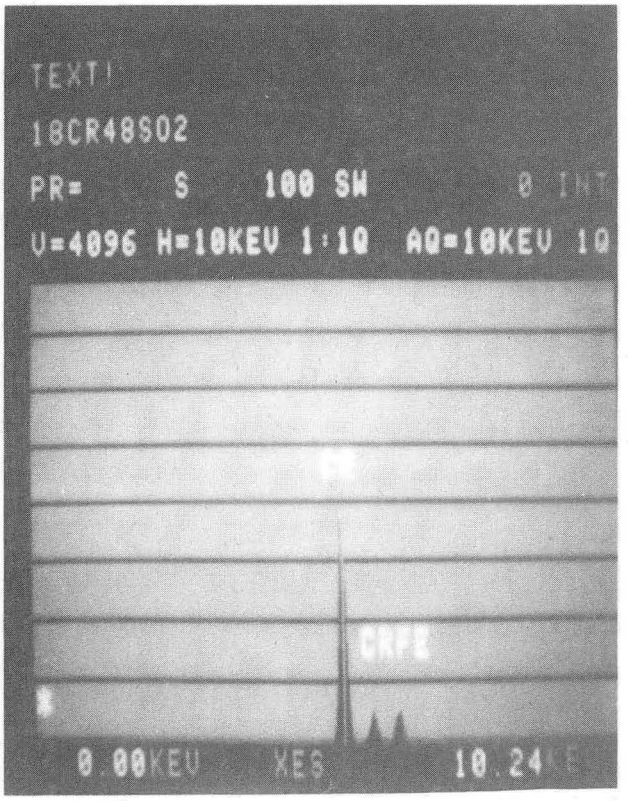

(b) XBB 831-232

Figure 43

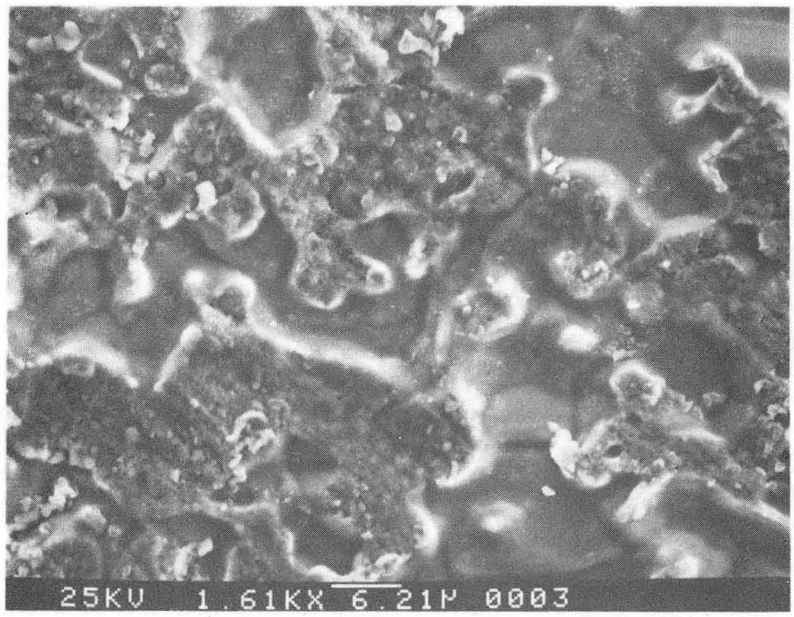

(a)

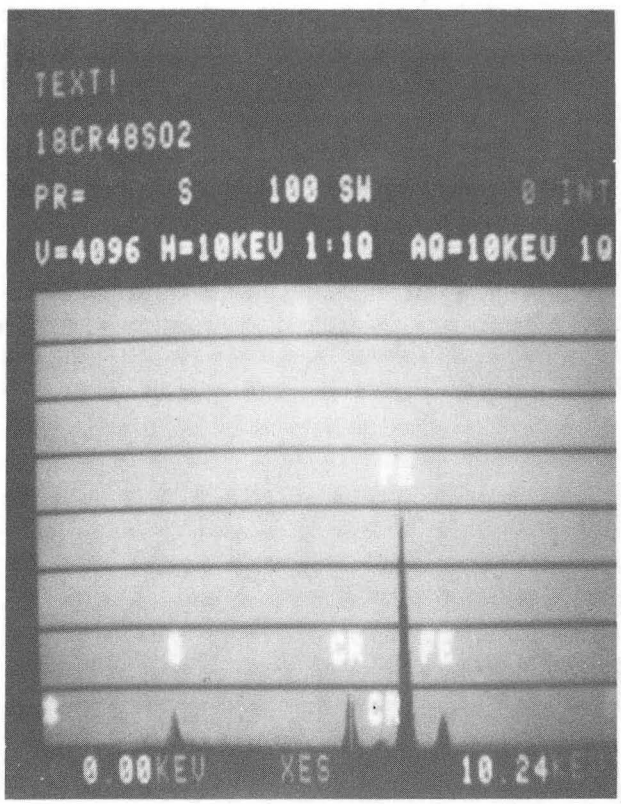

(b)

XBB 831-233

Figure 44

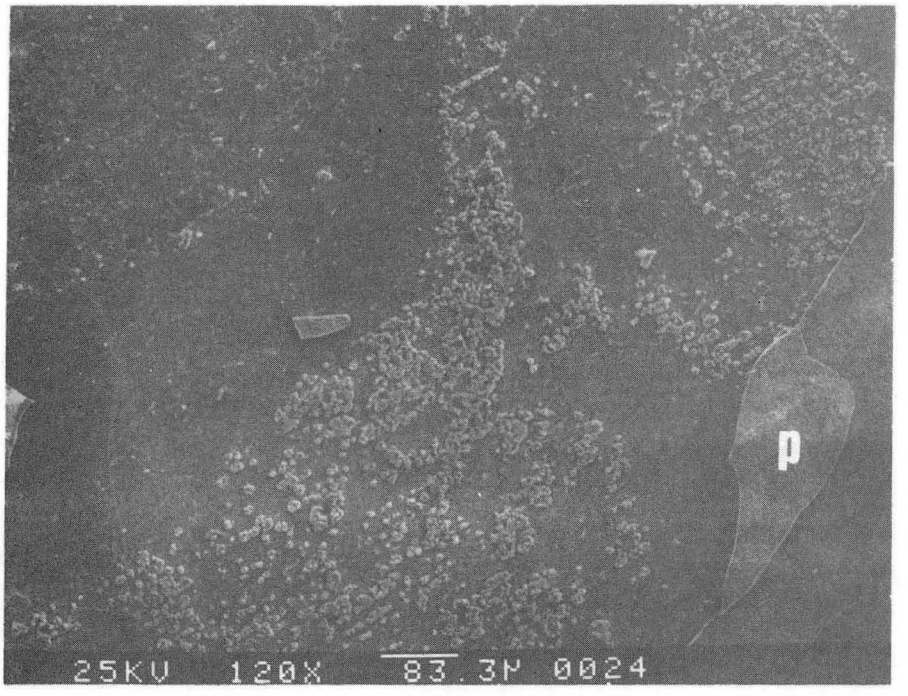

(a)

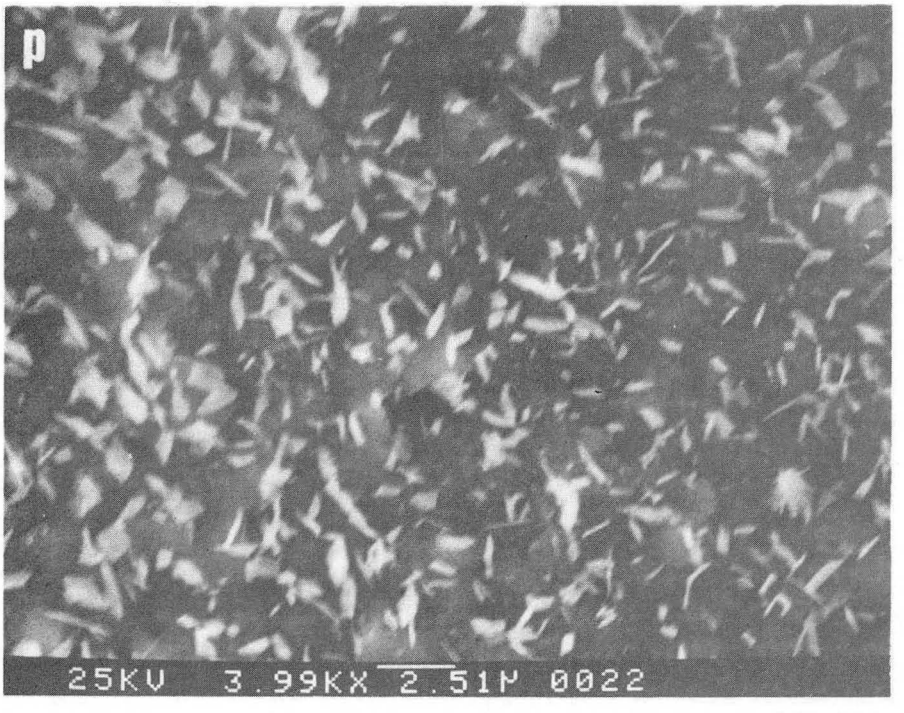

(b)

XBB 831-510

Figure 45

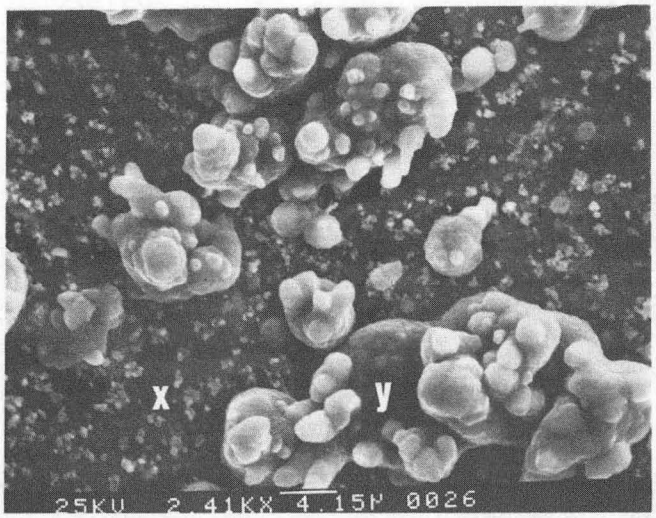

(a)

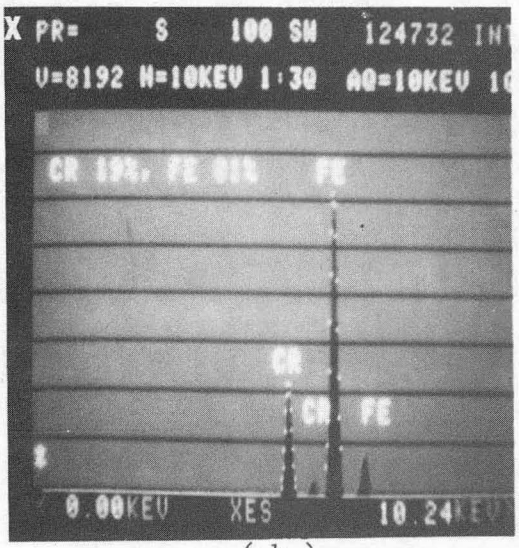

(b)

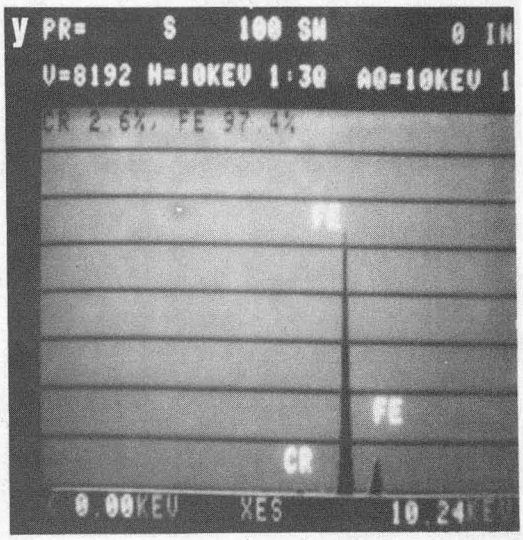

(c)

XBB 831-509

Figure 46

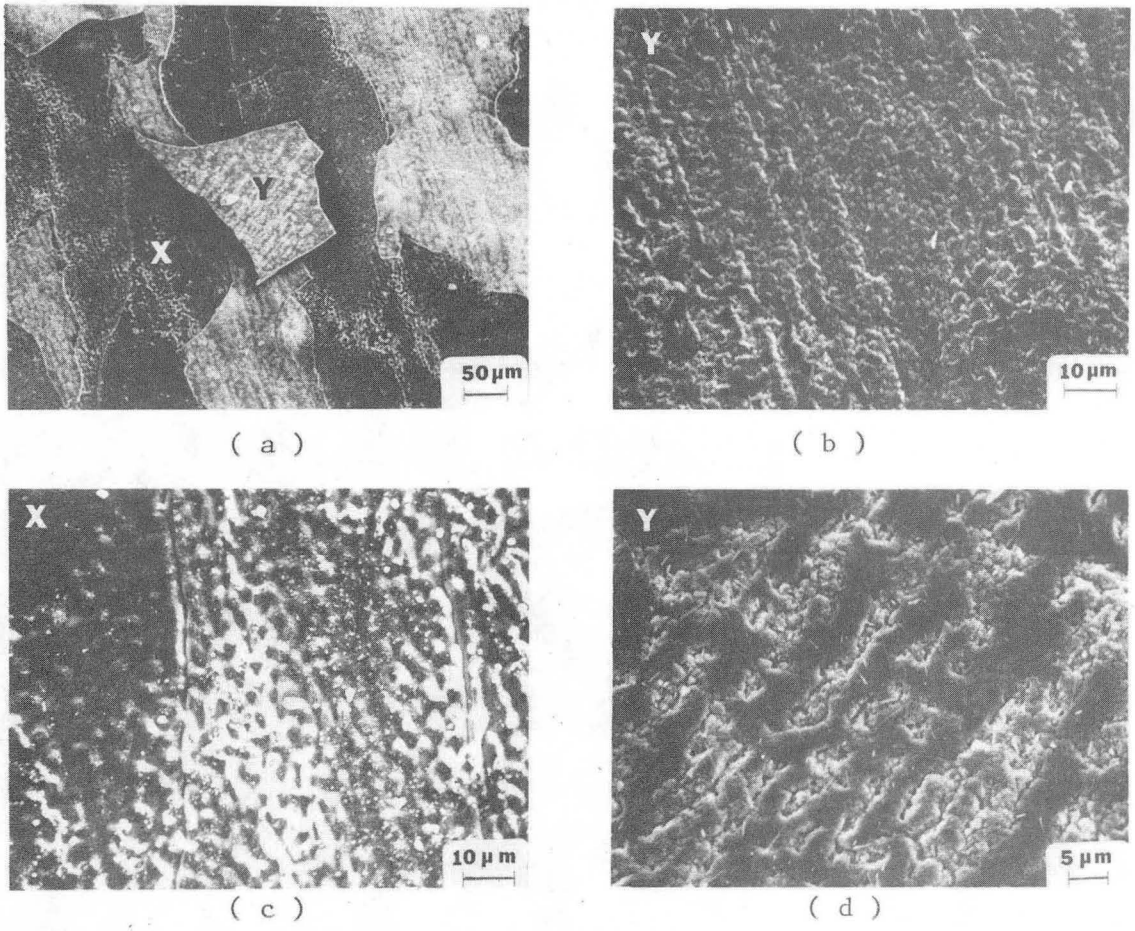

XBB 824-3938

Figure 47

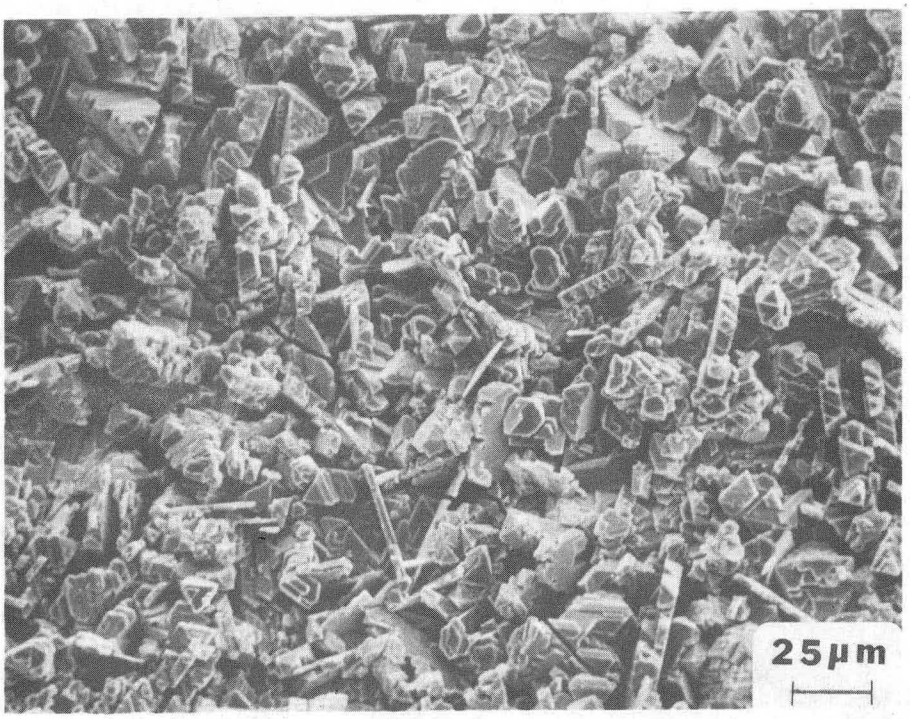

(a)

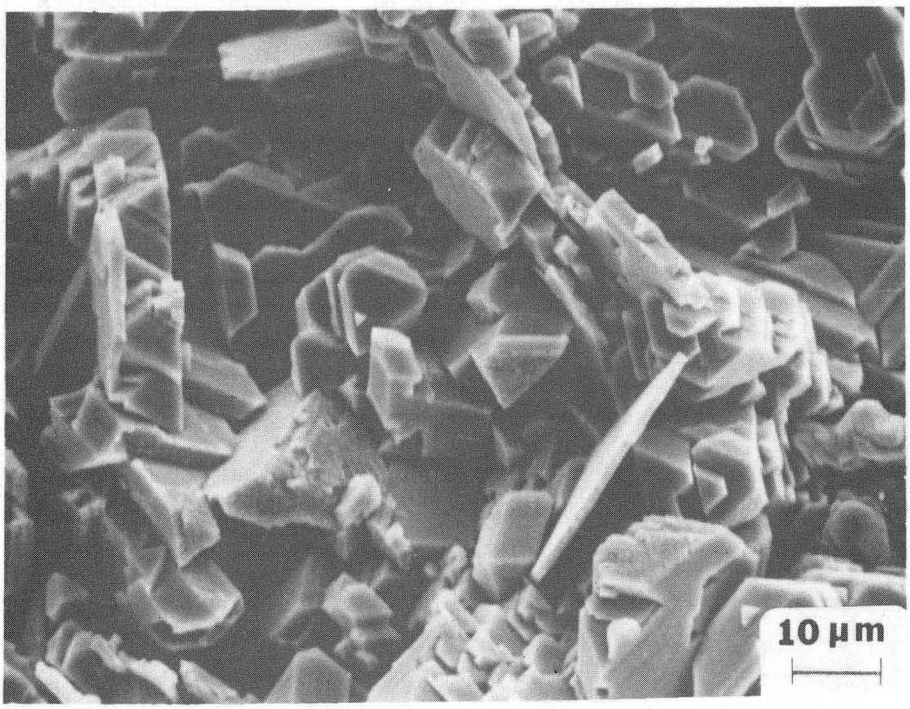

XBB 824-3943

(b)

Figure 48

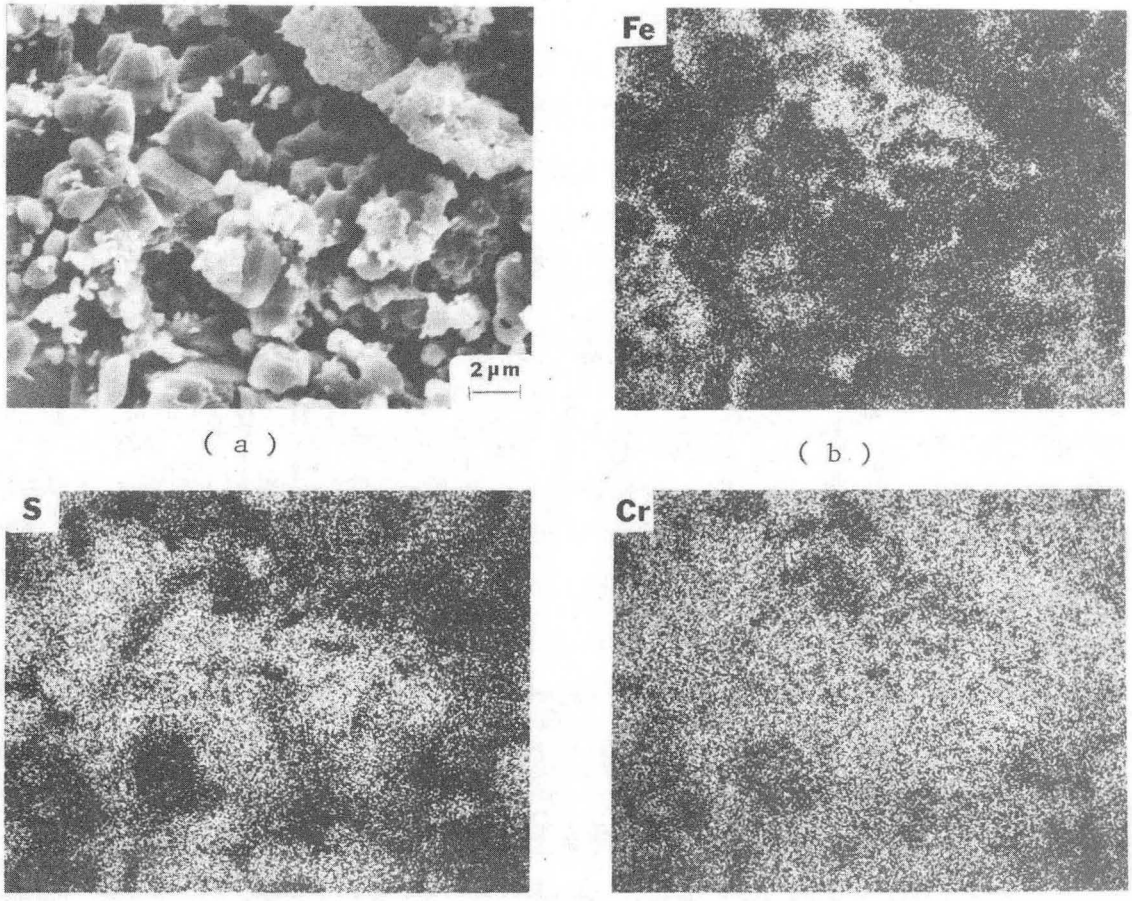

(a) (b) (c) (d)

XBB 824-3934

Figure 49

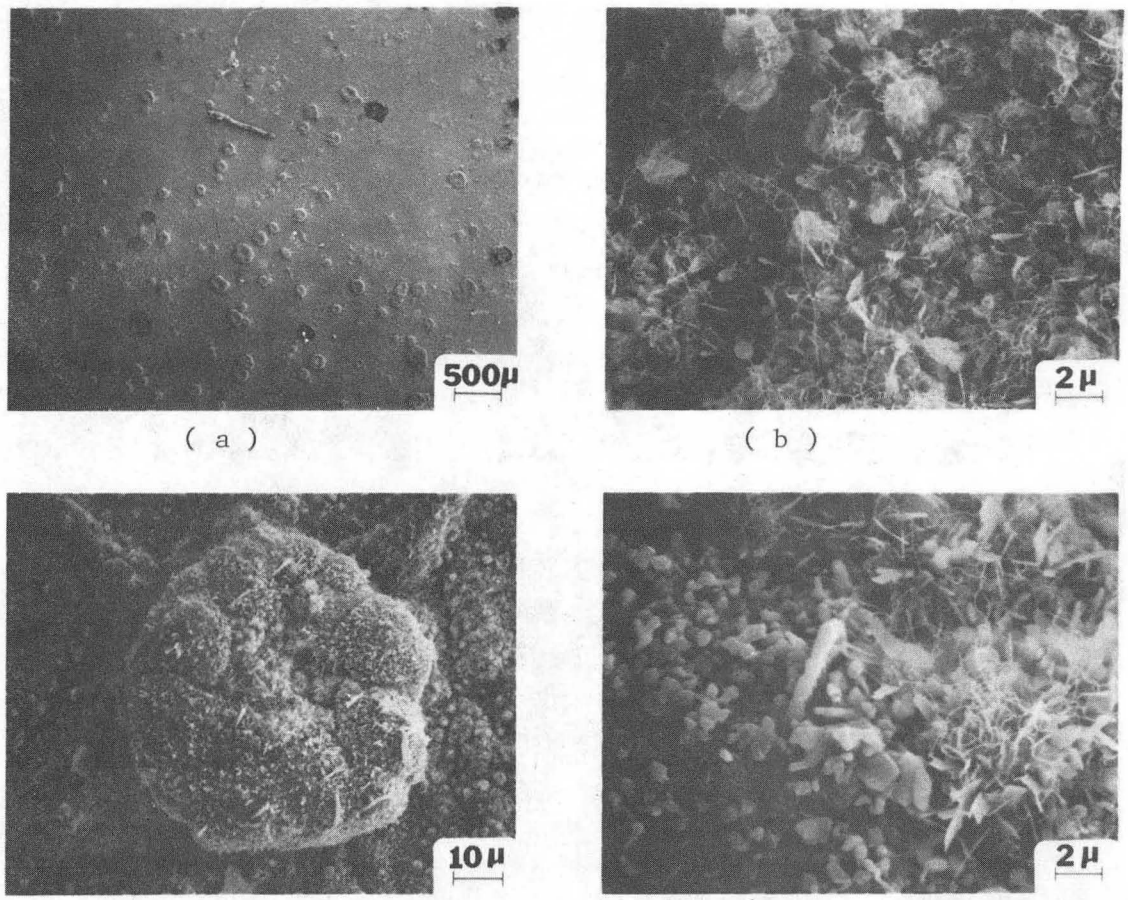

(a) (b)

(c) (d)

Figure 50

XBB 823-2280

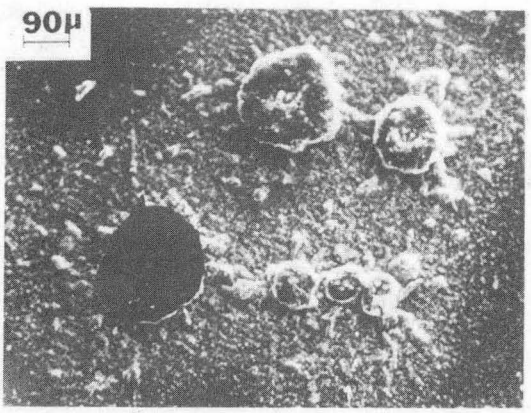

(a)

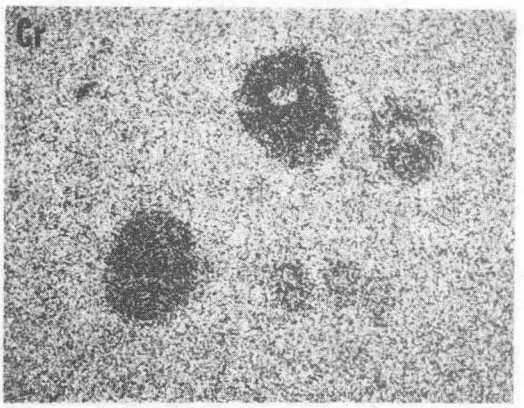

(b)

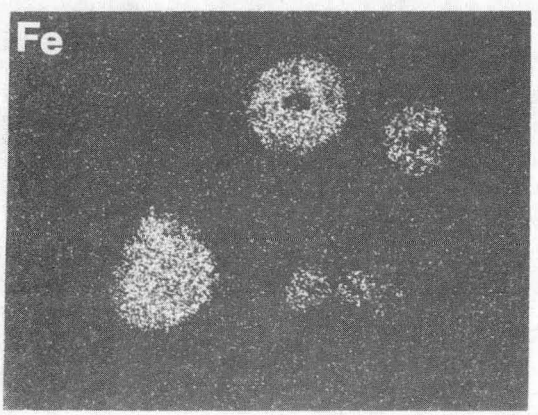

(c)

XBB 821-810

Figure 51

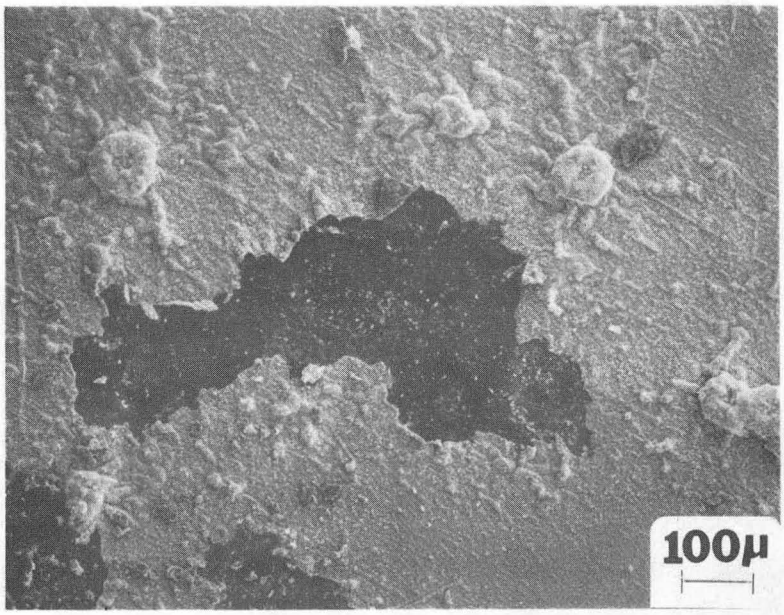

(a)

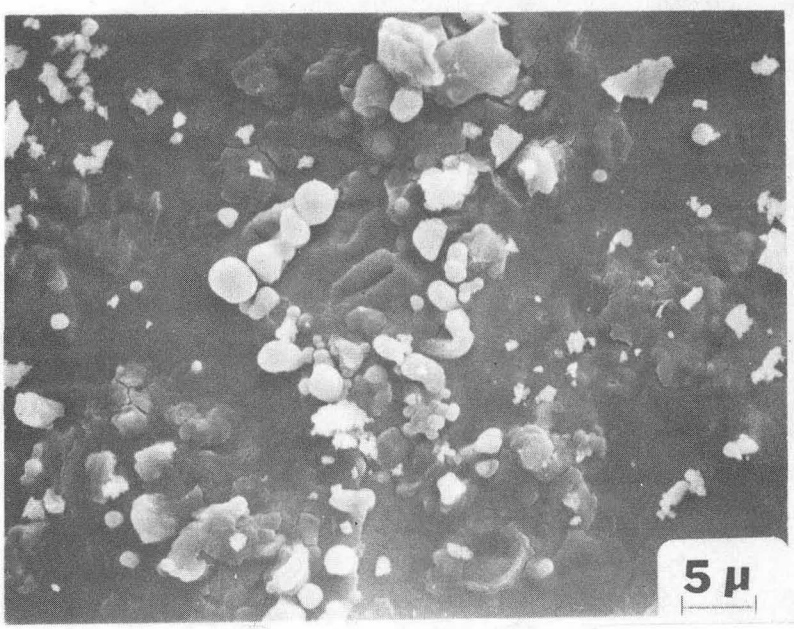

(b)

XBB 821-813

Figure 52

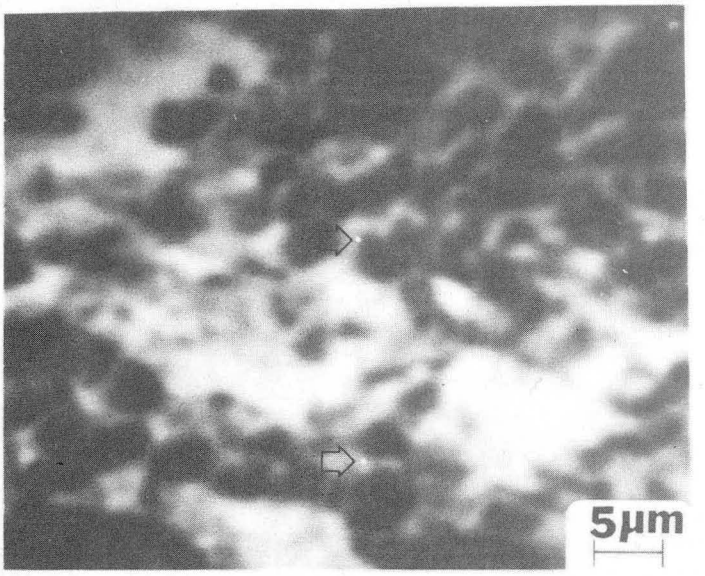

(a)

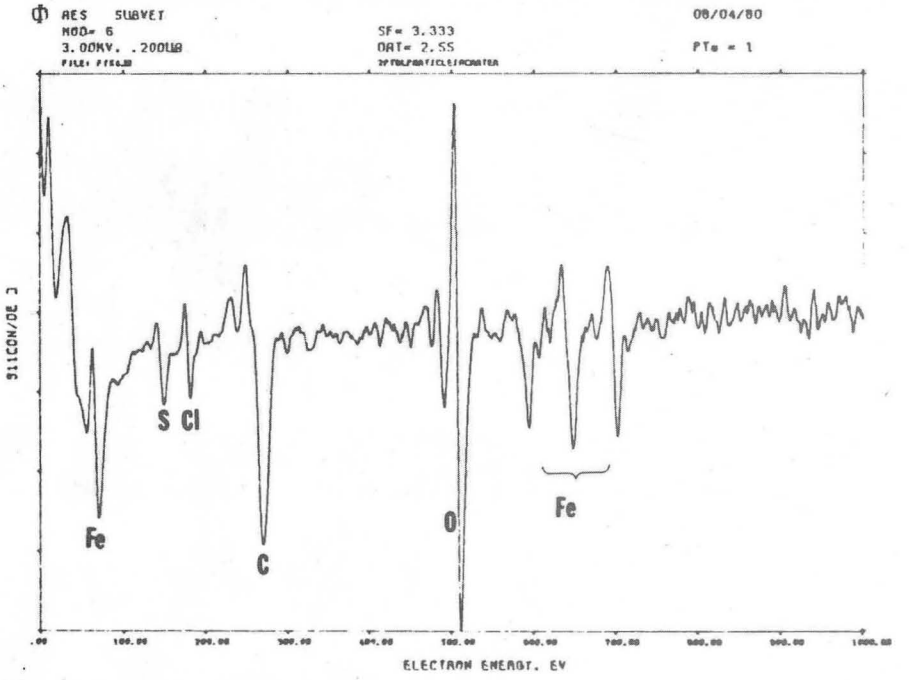

(b)

XBB 823-2277

Figure 53

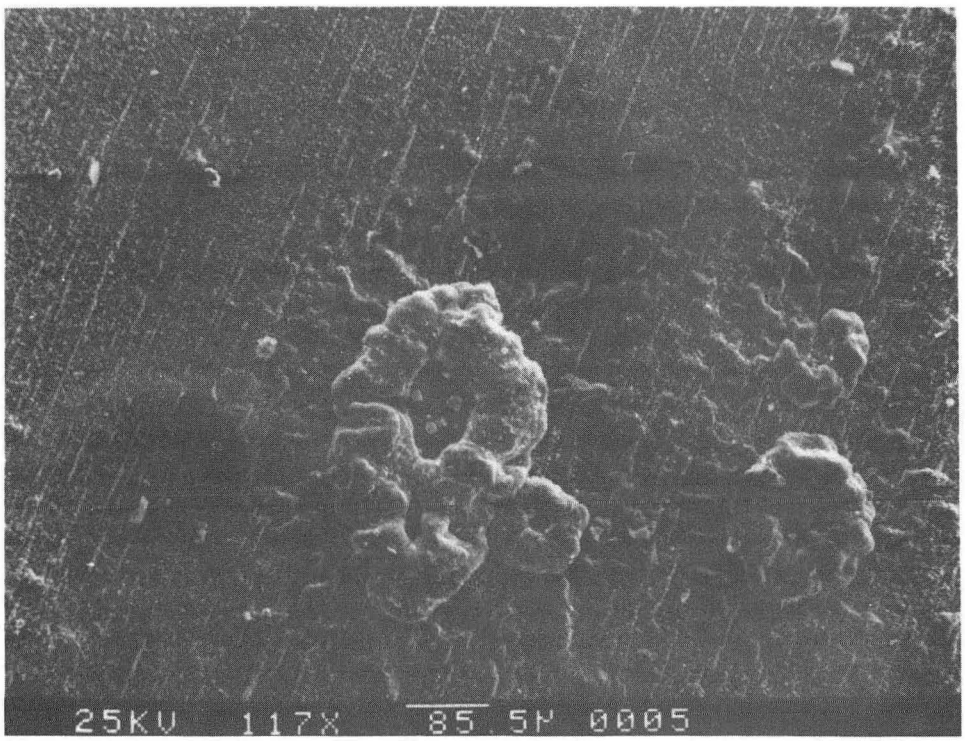

(a)

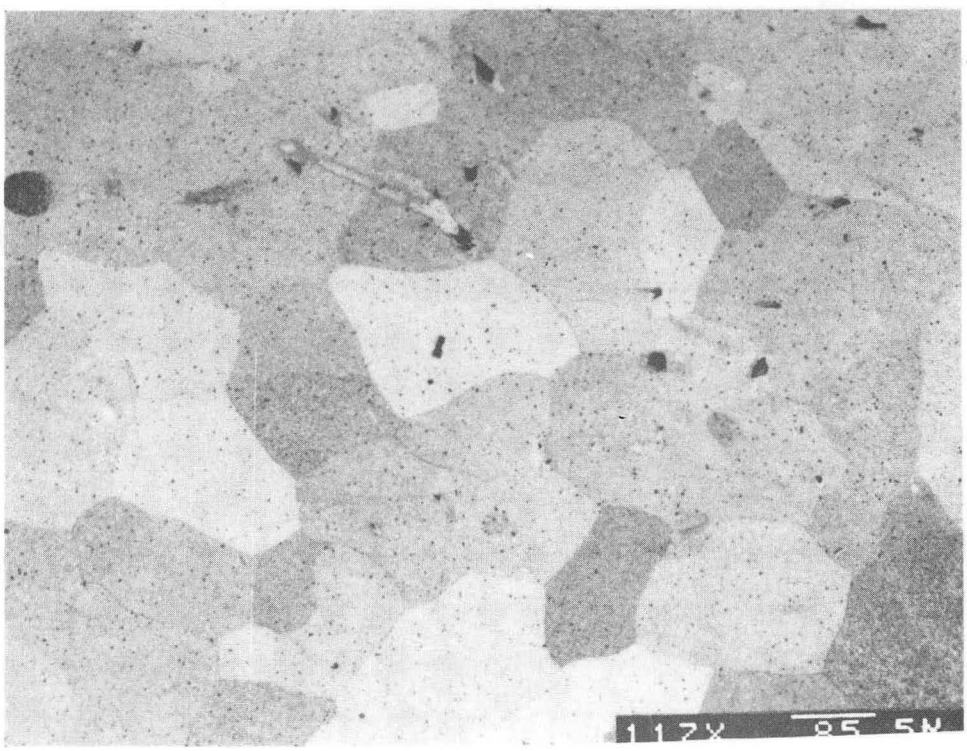

(b)

XBB 831-1

Figure 54

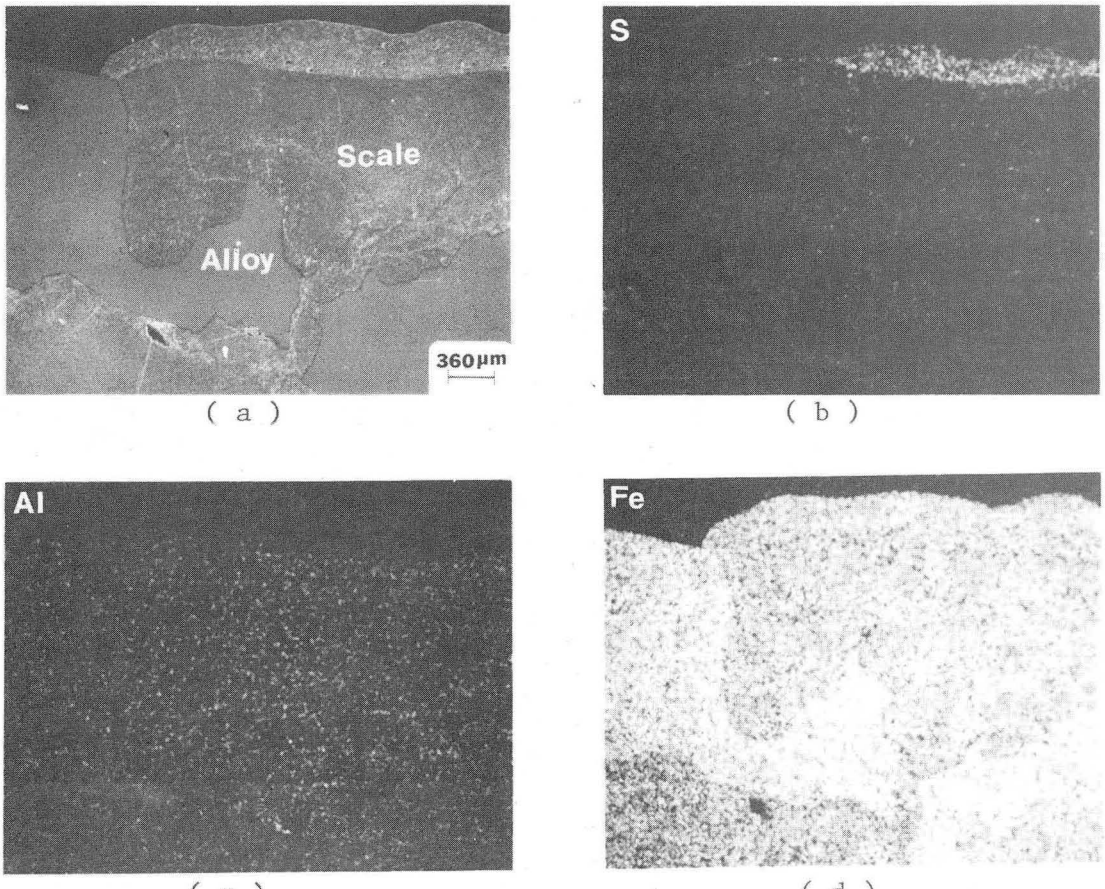

(a) (b) (c) (d)

XBB 823-2672

Figure 55

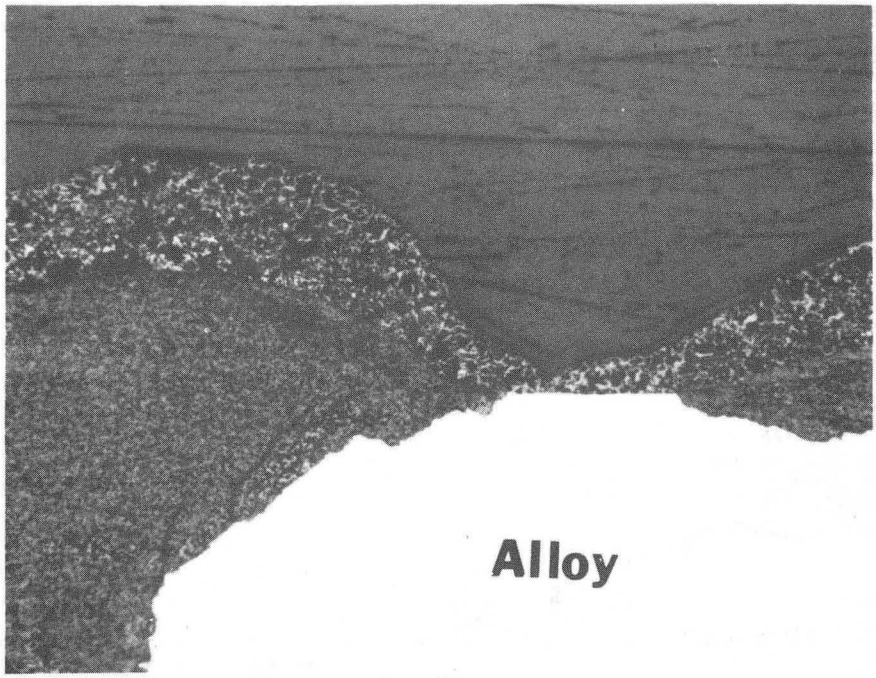

(a)

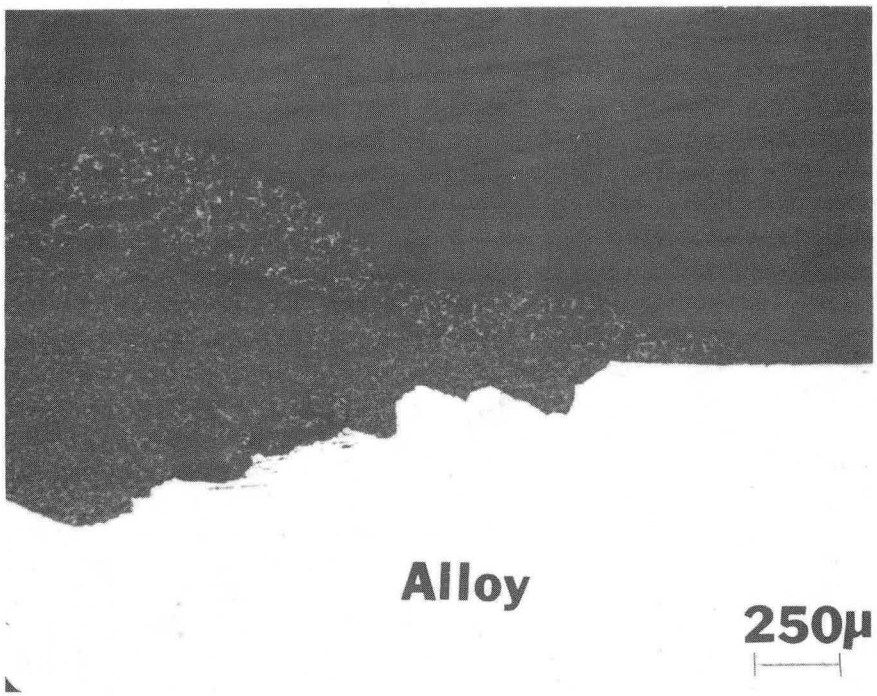

(b)

XBB 821-817

Figure 56

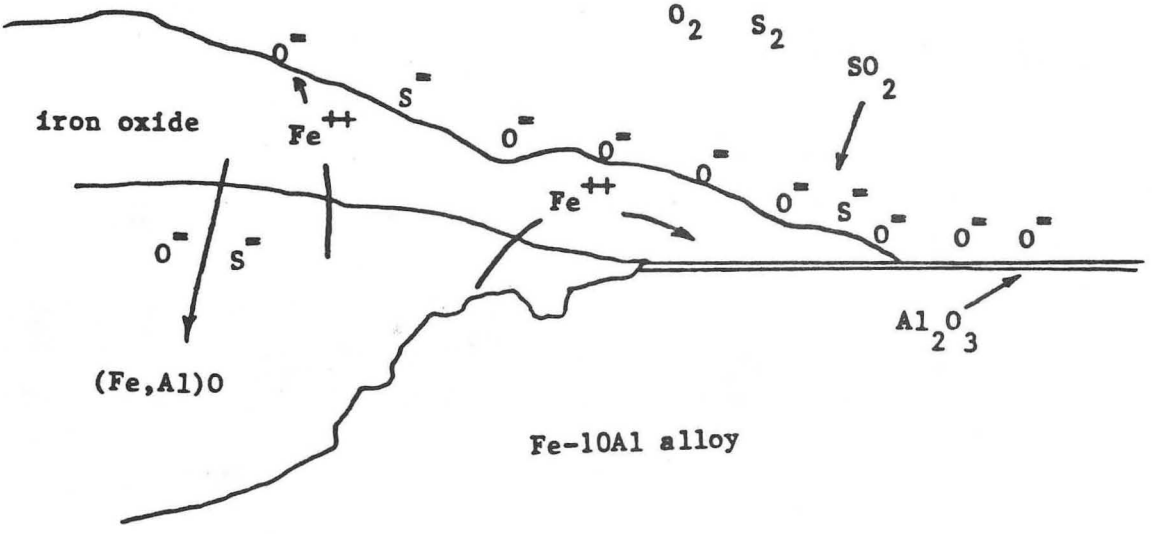
O_2 S_2
SO_2
$O^=$
$S^=$
$O^=$
$O^=$
$O^=$
$O^=$
$S^=$
$O^=$
$O^=$
$O^=$
Fe^{++}
Fe^{++}
iron oxide
$O^=$
$S^=$
(Fe,Al)O
Al_2O_3
Fe-10Al alloy

Figure 57

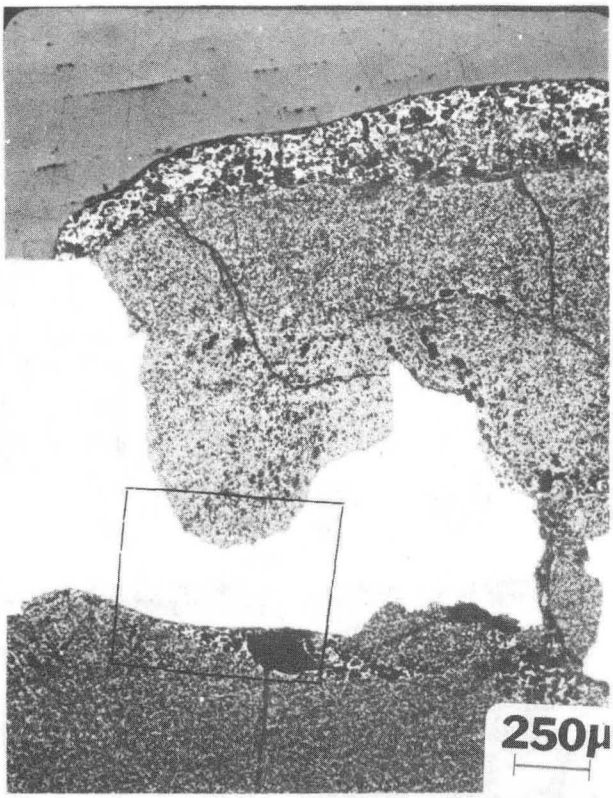

(a)

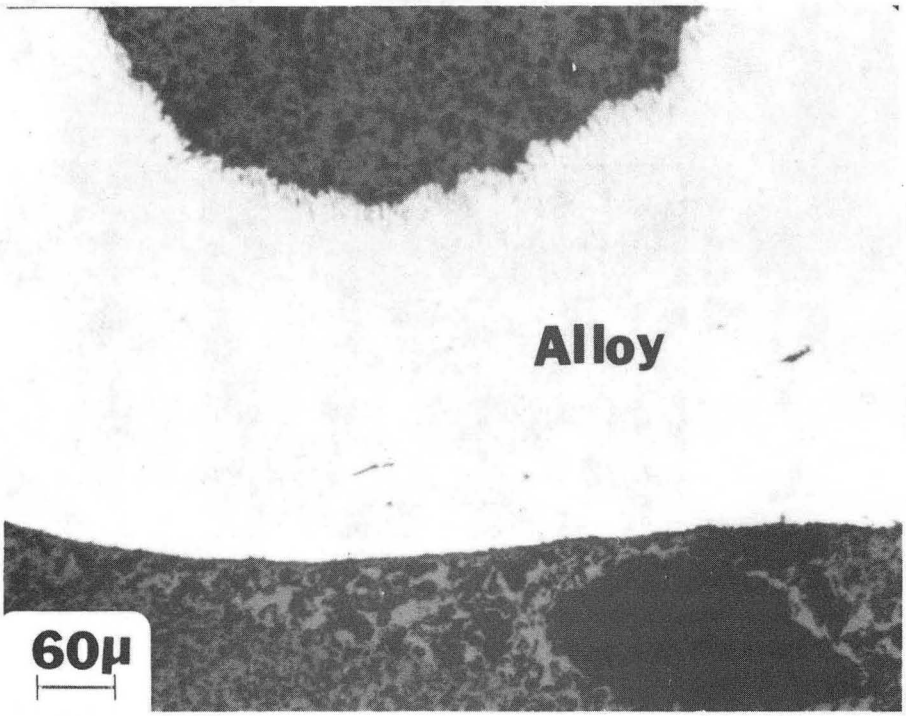

(b) XBB 821-827B

Figure 58

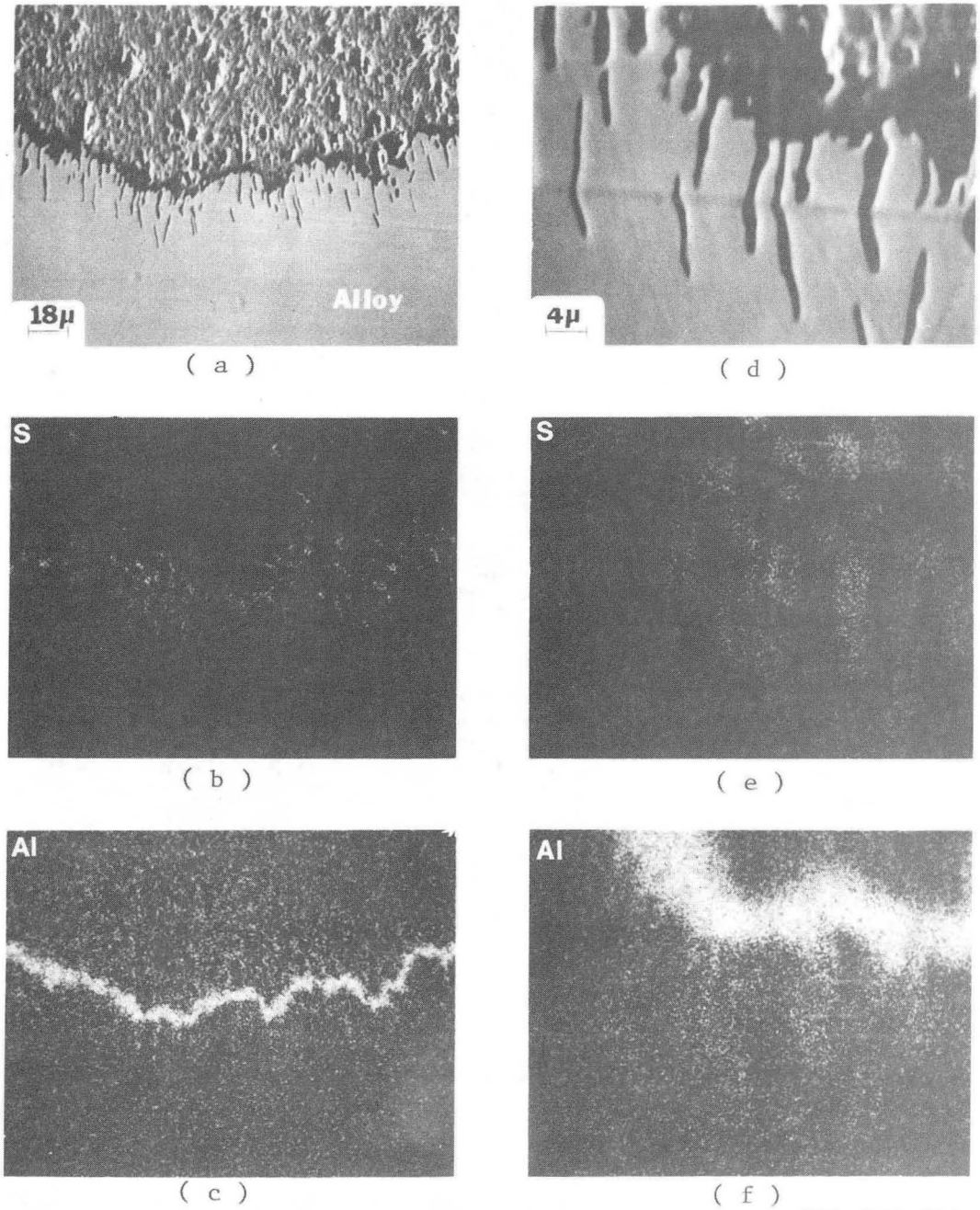

(a) (d)

(b) (e)

(c) (f)

XBB 821-832

Figure 59

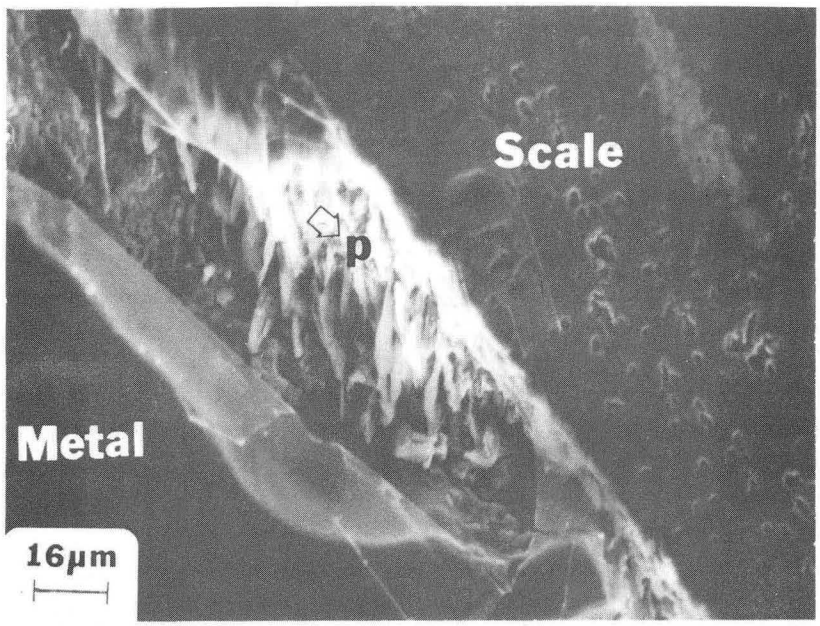

(a)

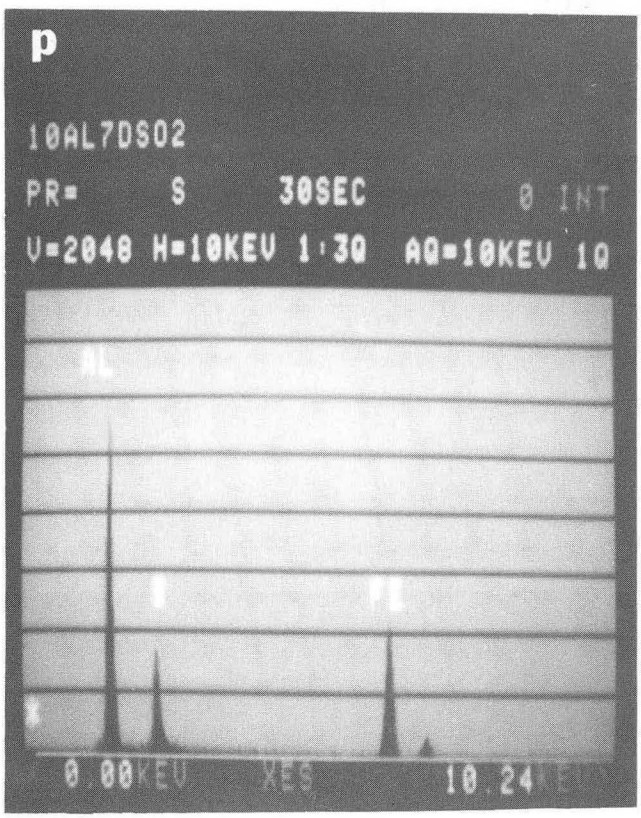

(b)

XBB 824-3947

Figure 60

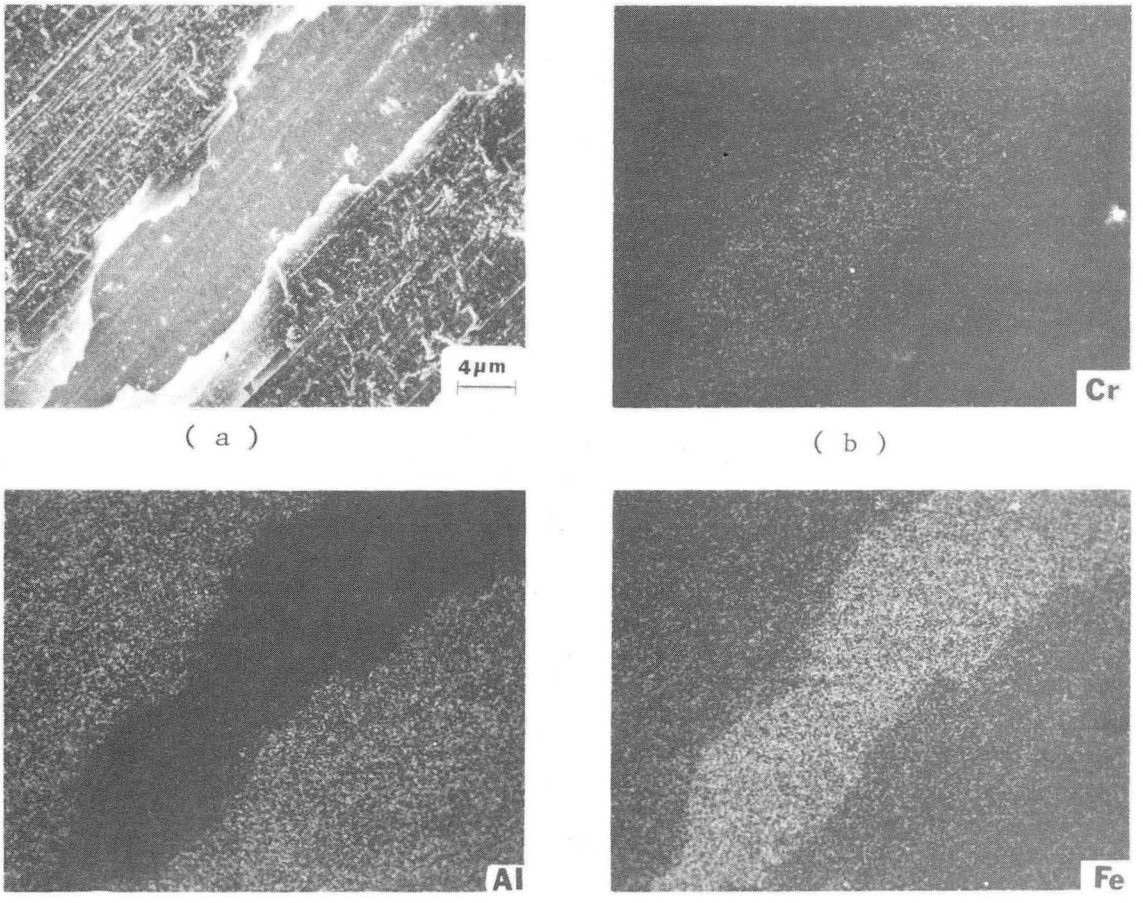

(a) (b) (c) (d)

XBB 824-3936

Figure 61

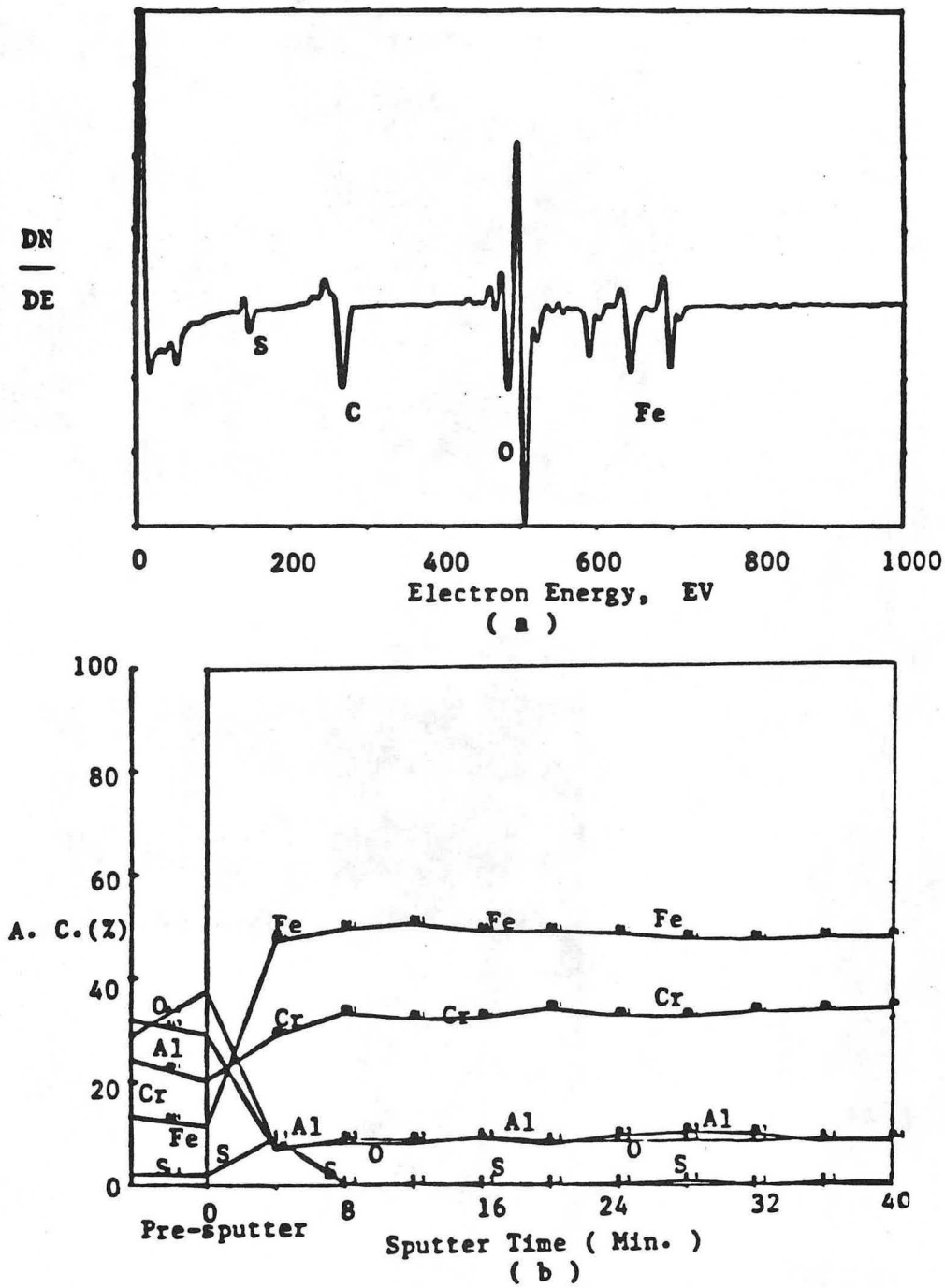
DN
DE
S
C
O
Fe
0
200
400
600
800
1000
Electron Energy, EV
(a)
100
80
60
A. C.(%)
40
20
0
O
Al
Cr
Fe
S
Fe
Cr
Al
S
O
S
0
8
16
24
32
40
Pre-sputter
Sputter Time (Min.)
(b)

Figure 62

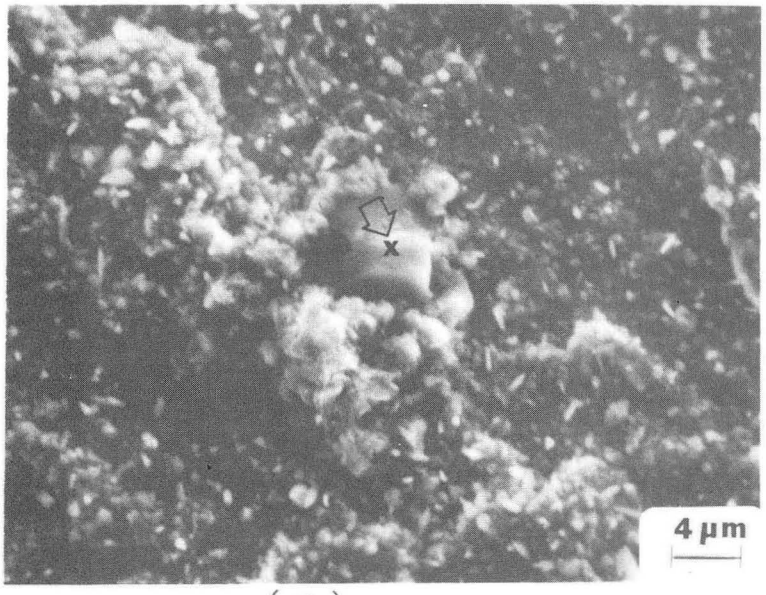

(a)

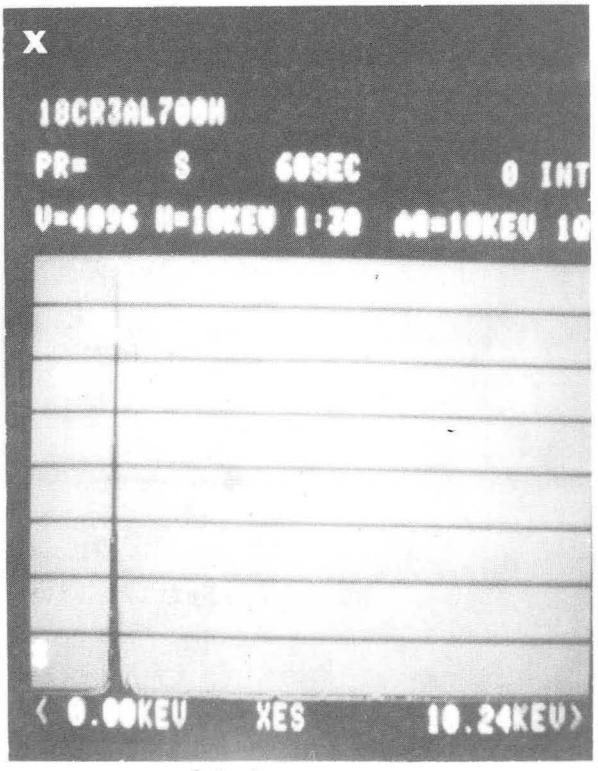

(b)

XBB 824-3948

Figure 63

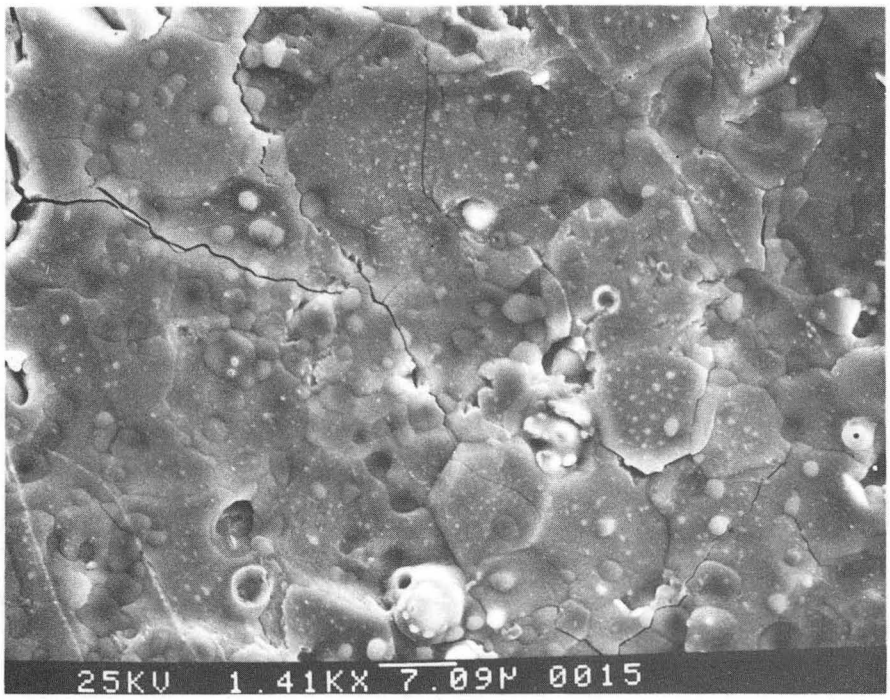

(a)

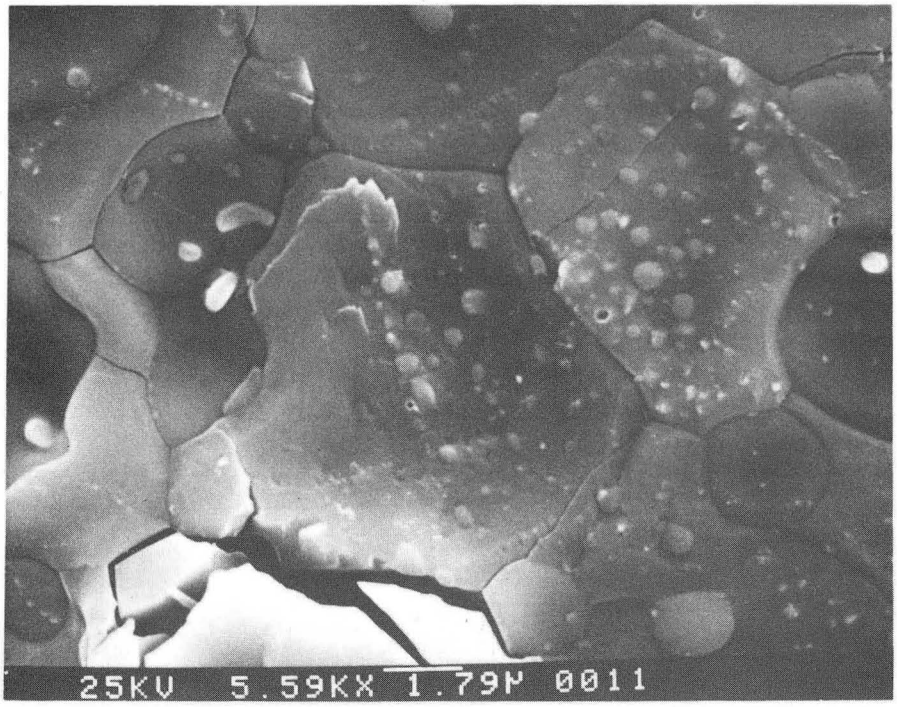

(b) XBB 826-5486

Figure 64

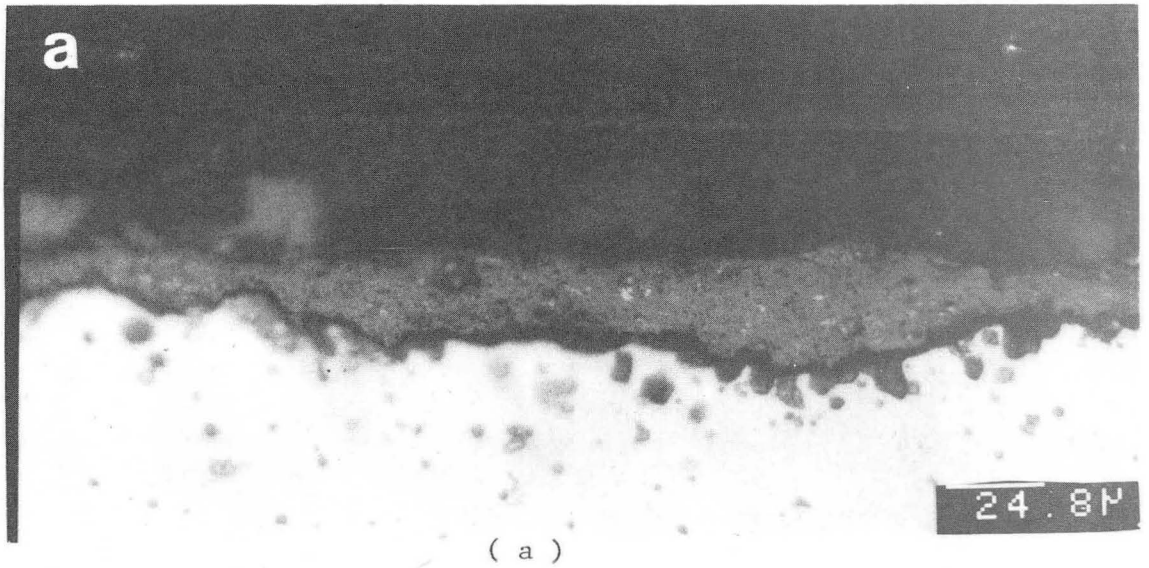

(a)

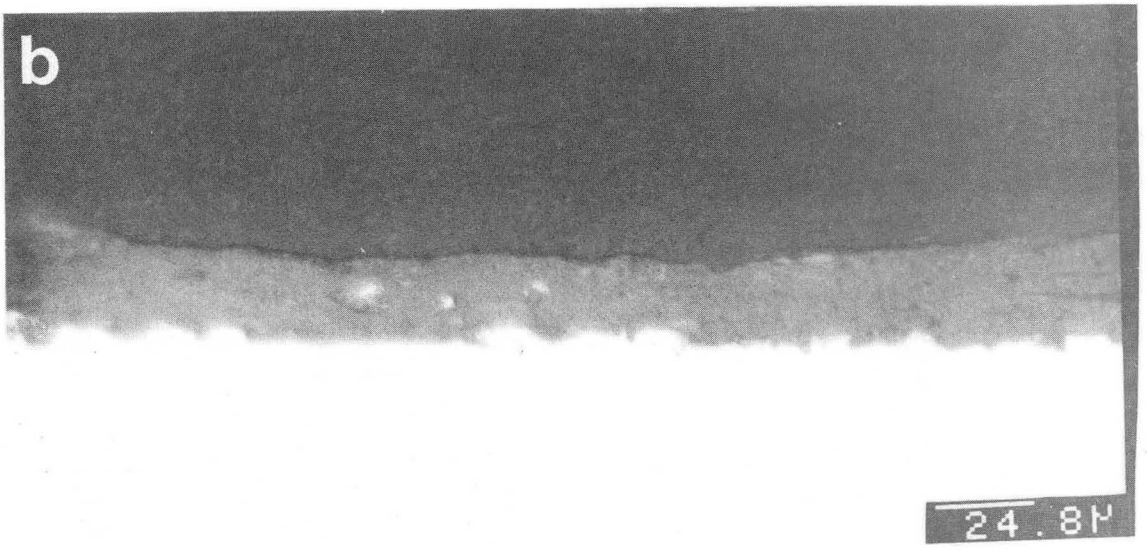

(b)

XBB 831-736

Figure 65

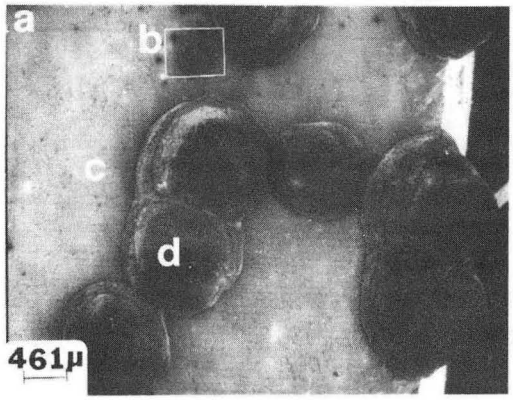

(a)

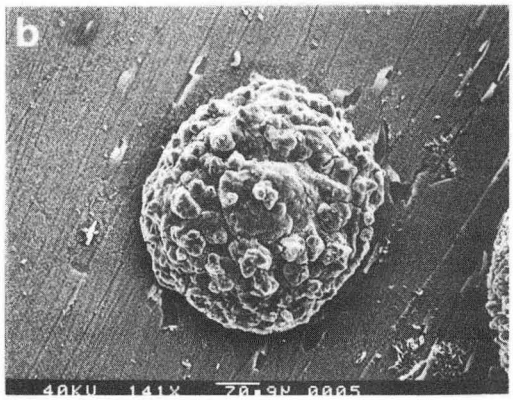

(b)

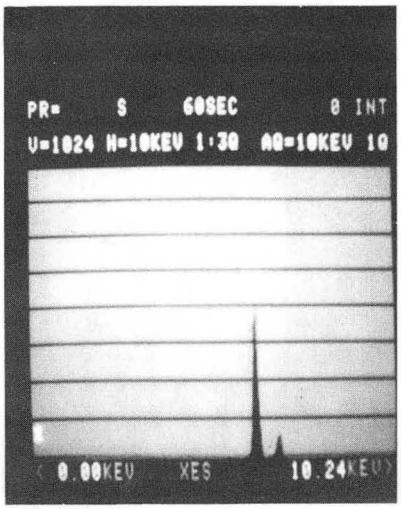

(c)

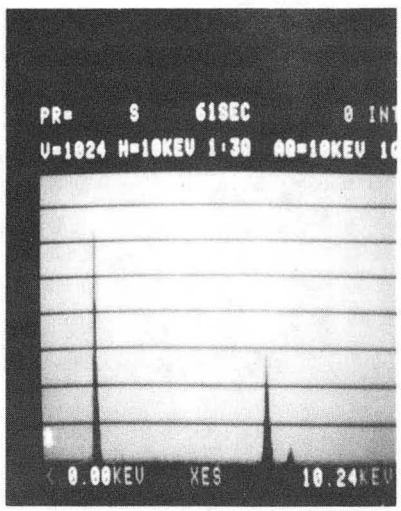

(d)

XBB 821-808

Figure 66

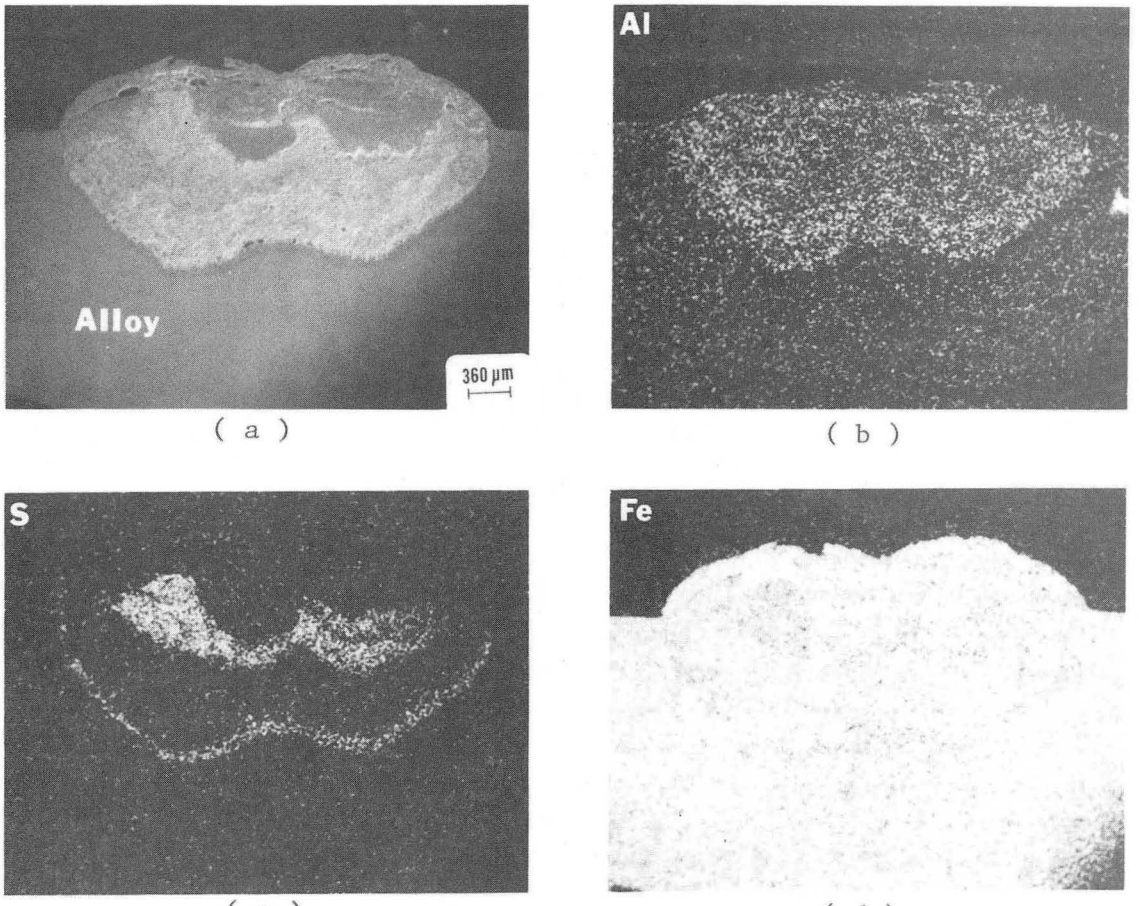

(a) (b) (c) (d)

XBB 826-5491

Figure 67

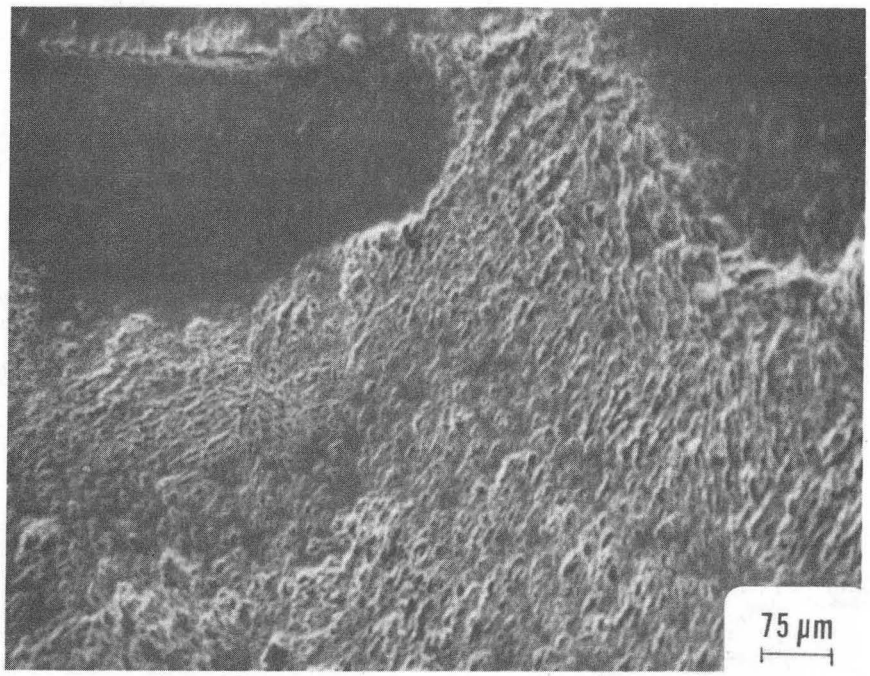

(a)

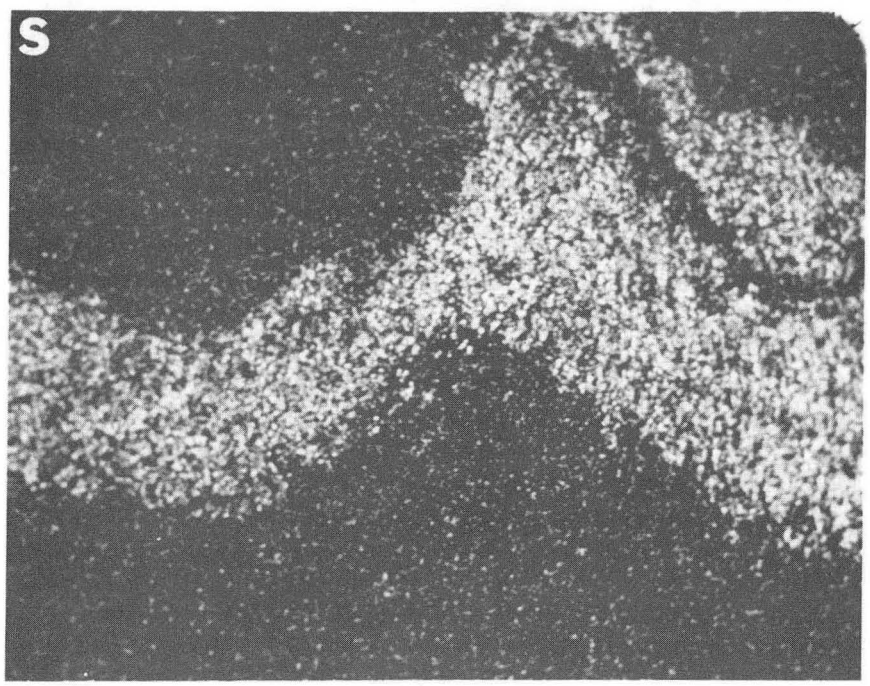

(b)

XBB 826-5488

Figure 68

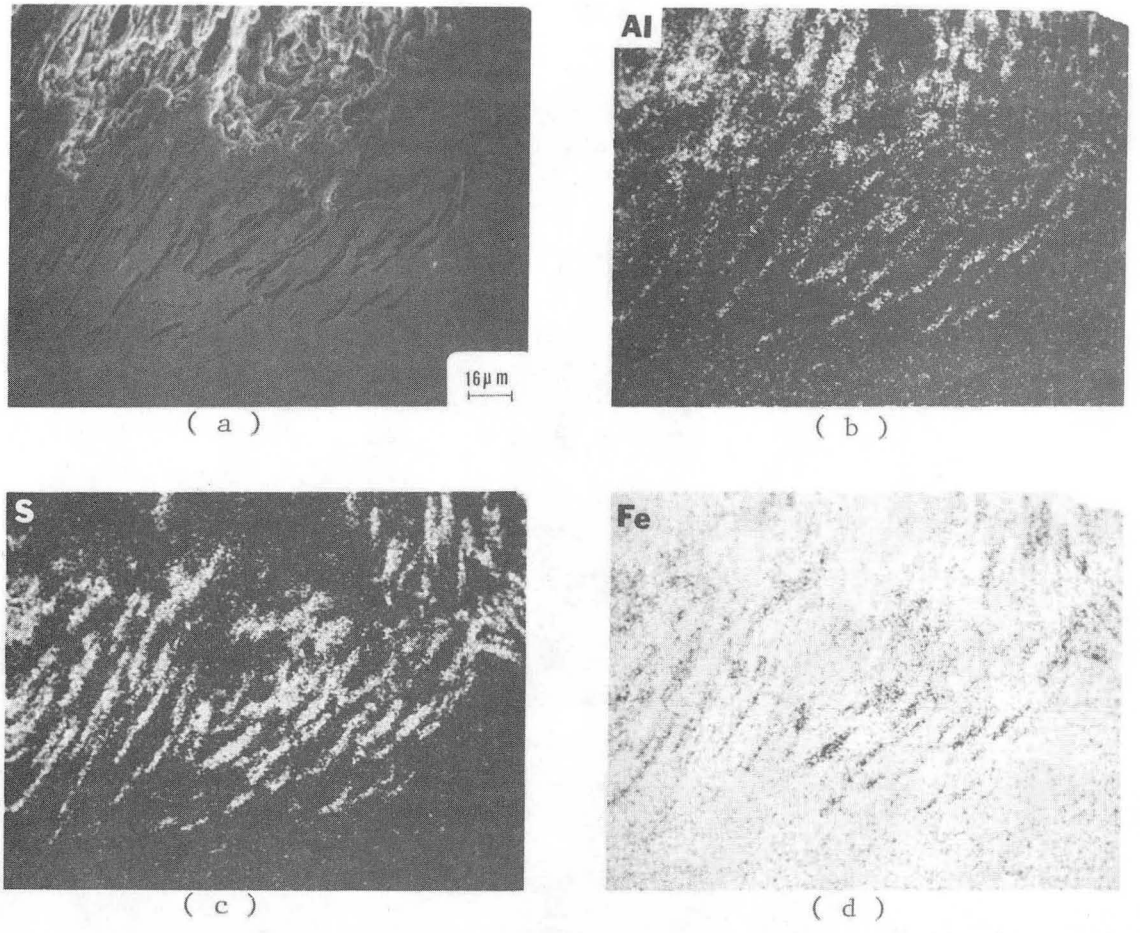

(a) (b) (c) (d)

XBB 826-5489

Figure 69

Case 1.

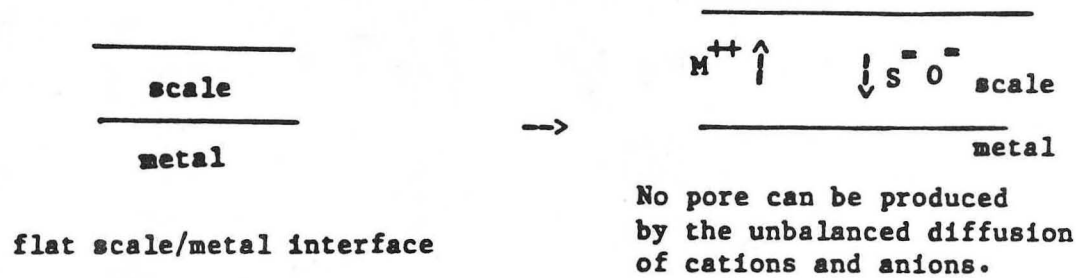

flat scale/metal interface

No pore can be produced by the unbalanced diffusion of cations and anions.

Case 2.

irregular scale/metal interface

Pores can be produced at the scale/metal interface by Kirkendall effect.

Case 3.

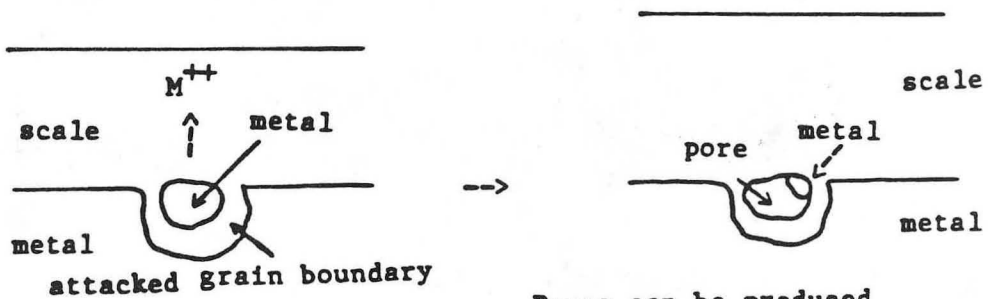

grain boundary attack near the scale/metal interface

Pores can be produced in the scale as

$V_{M^{++}}$ out > $V_{O^{=}}$ or/and $S^{=}$ in.

Figure 70

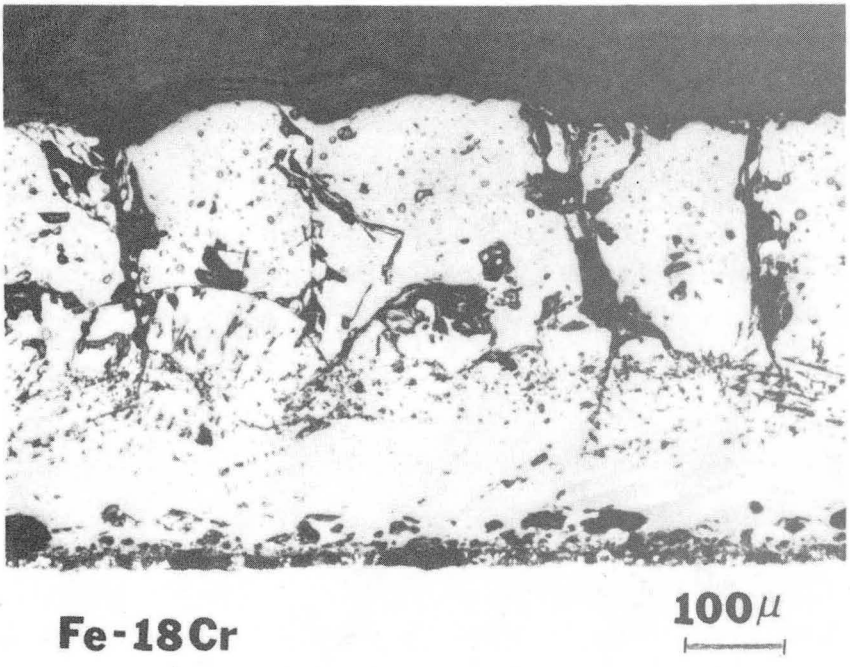

(a)

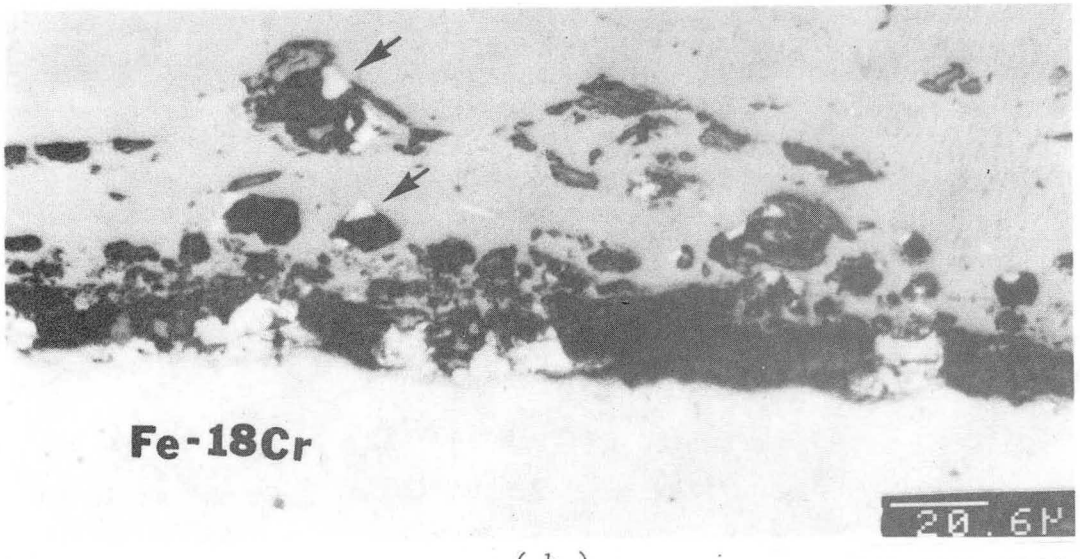

(b)

XBB 820-10720

Figure 71

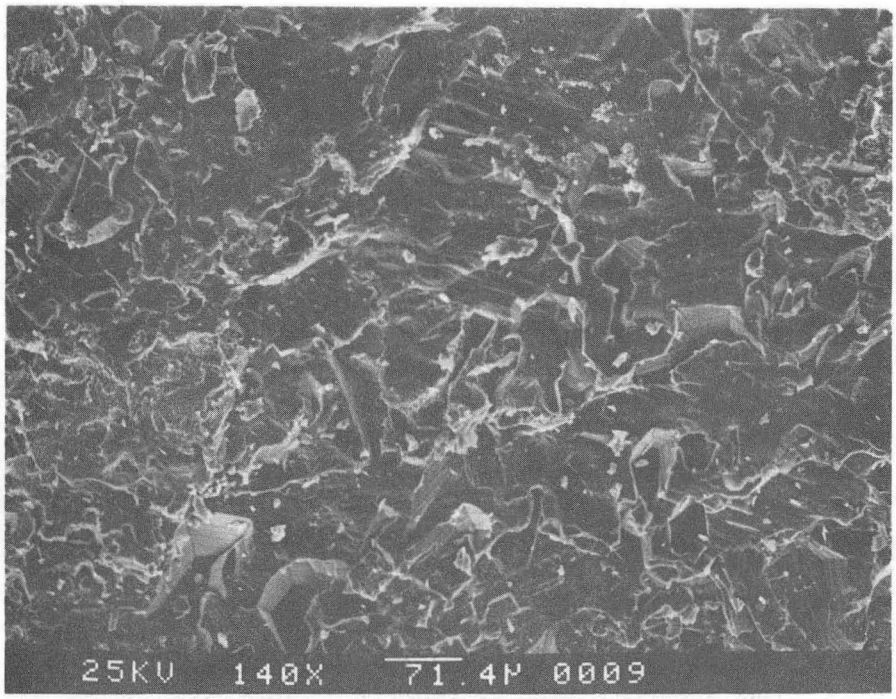

(a)

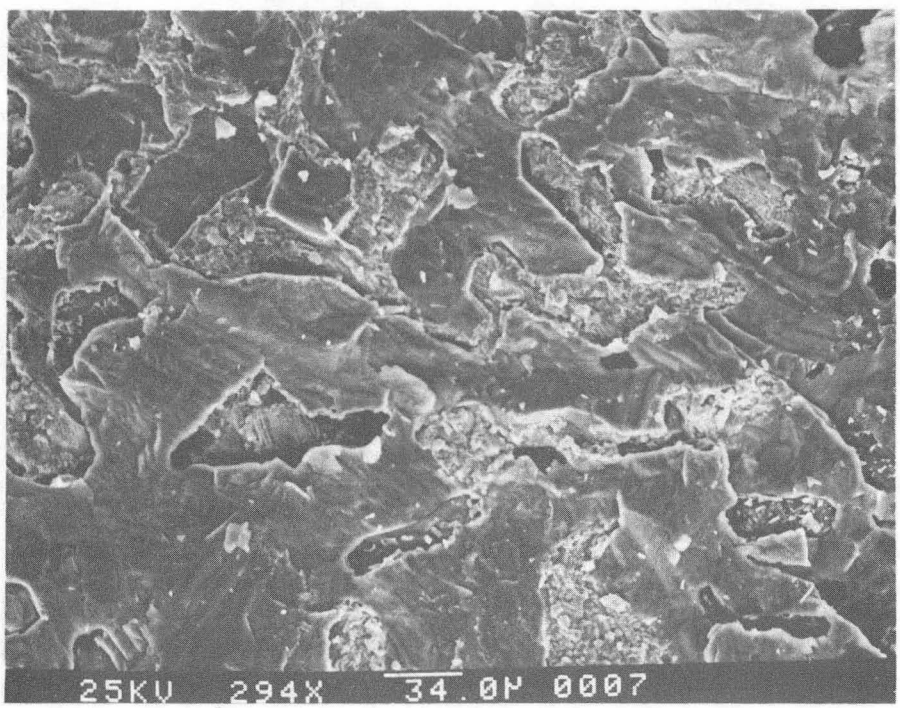

(b) XBB 828-7464

Figure 72

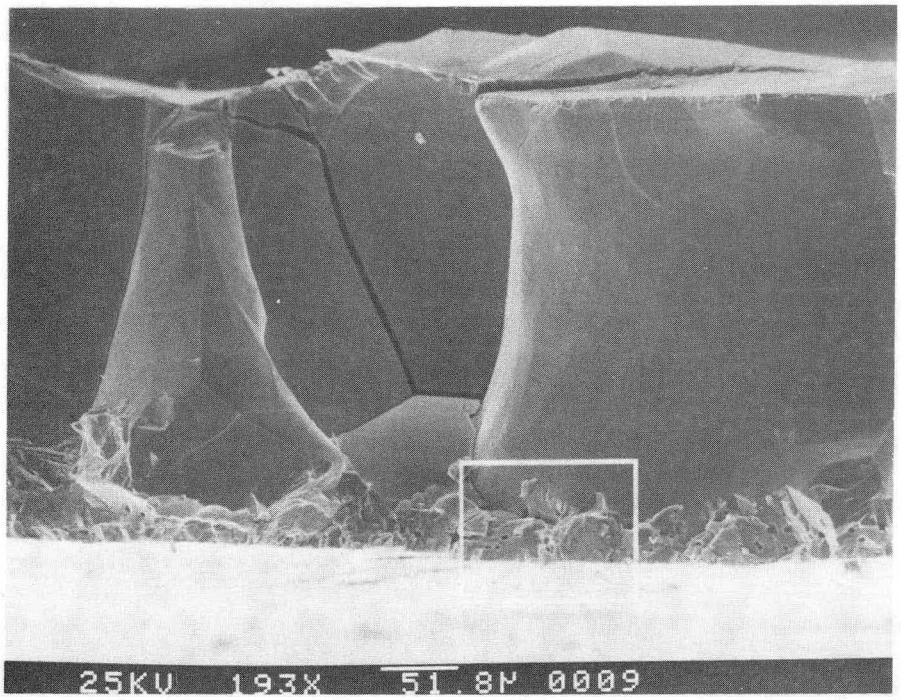

(a)

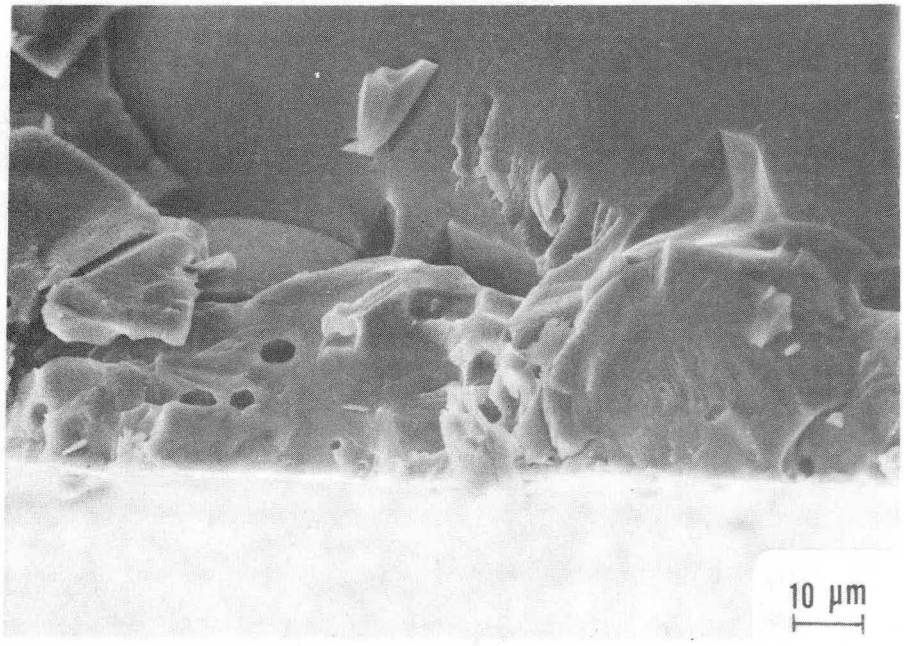

(b)

XBB 826-5485

Figure 73

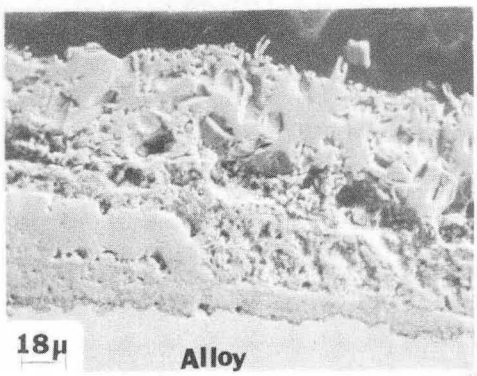

(a)

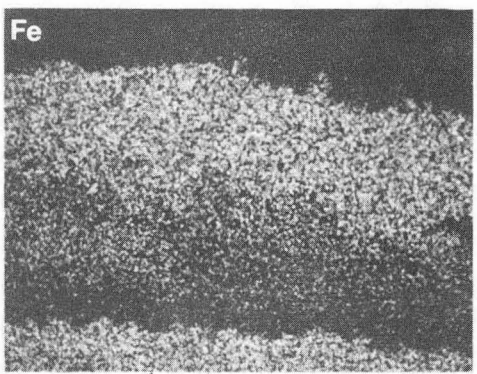

(b)

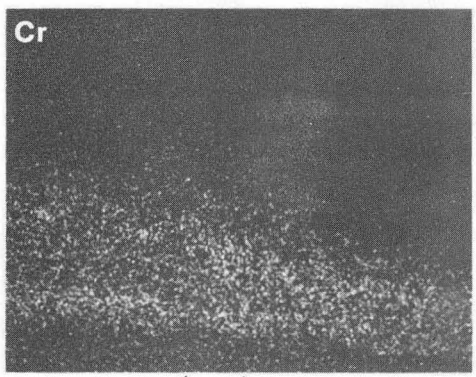

(c)

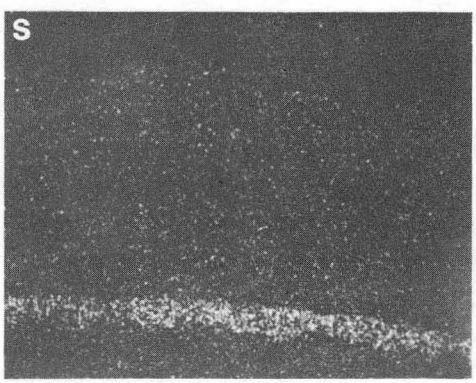

(d)

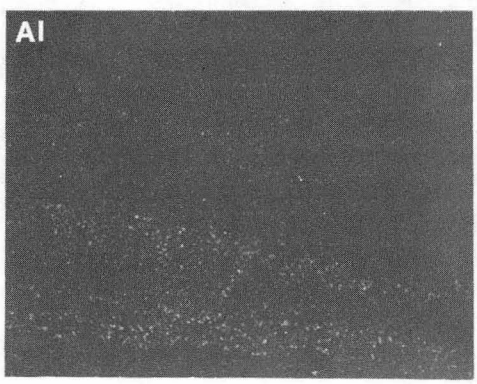

(e)

XBB 821-835

Figure 74

This report was done with support from the Department of Energy. Any conclusions or opinions expressed in this report represent solely those of the author(s) and not necessarily those of The Regents of the University of California, the Lawrence Berkeley Laboratory or the Department of Energy.

Reference to a company or product name does not imply approval or recommendation of the product by the University of California or the U.S. Department of Energy to the exclusion of others that may be suitable.

TECHNICAL INFORMATION DEPARTMENT
LAWRENCE BERKELEY LABORATORY
UNIVERSITY OF CALIFORNIA
BERKELEY, CALIFORNIA 94720